10

Computational Methods for Predicting Field Intensity and Temperature Change

James C. Lin and Paolo Bernardi

CONTENTS

10.1 Introduction

Electromagnetic energy at both high and low-frequencies can be transmitted into biological materials through the use of antennas or applicators. Antennas launch the electromagnetic energy into the medium. They serve to couple the generating source of electromagnetic energy into the medium, which surrounds it. The spatial distribution of electromagnetic energy from an antenna is directional and varies with distance from the antenna. At distances sufficiently far from an antenna, so that local field distribution changes predictably and varies mostly with distance, the region is called a far field or radiation zone. In the near field or near zone close to the antenna, the electromagnetic energy distribution varies as a function of both angle and distance. Moreover, the behavior of electromagnetic fields (EMFs) and their coupling and interaction with biological systems are very different, depending on whether they are in the near or far zone. In fact, these differences constitute the major variances between radio frequency (RF) and low-frequency energy deposition into biological systems. As shown in subsequent sections, the induction of electric and magnetic fields, deposition of electromagnetic power, absorption of electromagnetic energy, and their penetration into tissue, all are functions of the source and its frequency or wavelength. In general, when considering the interaction of EMFs with biological systems, it is necessary to account for the frequency or wavelength and its relationship to the physical dimensions of the body.

In addition, the interaction of EMFs with biological systems is characterized by the electromagnetic properties of tissue media, specifically, dielectric permittivity. Biological materials have magnetic permeability values close to that of free space and are independent of frequency. In a medium such as biological tissue with a finite electrical conductivity σ, a conduction current, $\mathbf{J} = \sigma\mathbf{E}$, can be induced to flow, giving rise to energy loss by joule heating. Clearly, fields must be coupled into tissues, and energy must be deposited or absorbed in the biological systems, regardless of the mechanism that is accountable for an effect, for the system to respond in some manner. Thus, to achieve any biological response, the electric field, magnetic field, or EMF that is exerting its influence must be quantified and correlated with the observed phenomenon.

The purpose of this chapter is to present an account of electromagnetic interactions in biological media, with special emphasis on the energy coupling and distribution characteristics in models of biological structures. Such information is essential for analyzing the interrelationships among various observed biological effects, for separating known and substantiated effects from those that are speculative and unsubstantiated, for assessing

the therapeutic effectiveness of electromagnetic waves, and for extracting diagnostic information from field effects.

There exist a wide variety of methods for quantifying fields in biological bodies. The extent of computer usage varies, depending on the specific information sought and the complexity of tissue geometry. This chapter outlines a number of techniques that have been successfully employed to analyze the propagation and absorption characteristics of electromagnetic energy in tissue structures. There are two general approaches: one involves extensive use of analytical development and the other relies more heavily on numerical formulation. Analytical computations are most suited for calculation of the distribution of absorbed energy in simplified tissue geometries such as plane slabs, cylinders, and spheroids, whereas numerical methods offer the opportunity of analyzing the coupling of electromagnetic energy to animal and human bodies, which is difficult, if not impossible, to approach analytically. The advantages and limitations of various methods for field computations, along with representative results, are provided in this chapter. In some cases, for additional details, the reader is referred to previous editions of this handbook [1,2]. This chapter will begin with a brief introduction to the concepts of induced field and power deposition and the characteristics of field intensities and dosimetric quantities.

10.1.1 Induced Field Intensity and Dosimetric Quantities

The quantities of import to characterize coupling of electromagnetic energy into biological systems include the incident field, induced field, power deposition, and absorbed energy. The metrics of specific absorption rate (SAR) and specific absorption (SA) in biological systems or tissue models have been adopted as the dosimetric quantities, especially at RF frequencies. The metric SAR (in W/kg) is defined as the time derivative of the incremental energy absorbed by (or dissipated in) an incremental mass contained in a volume of a given density. SA (in J/kg) is the total amount of energy deposited or absorbed and is given by the integral of SAR over a finite interval of time. Information on SA and SAR is of interest because it may serve as an index for comparison and extrapolation of experimental results from tissue to tissue, from animal to animal, from animal to human, and from human to human exposures. It is also useful in analyzing the relationships among various observed biological effects in different experimental models and subjects. This is in clear contrast to incident field or any other external measures of exposure, which often do not provide the same field inside biological systems of different sizes, species, or constitutions.

Moreover, determination of the induced field would be preferred because it (1) relates the field to specific responses of the body, (2) facilitates understanding of biological phenomena, and (3) is independent of mechanisms of interaction. Once the induced field is known, quantities such as SAR (in W/kg) can be derived from it by a simple conversion formula. For example, from an induced electric field E (in V/m), the SAR can be derived as

$$\mathrm{SAR} = \frac{\sigma E^2}{\rho_{\mathrm{m}}} \tag{10.1}$$

where σ is the bulk electrical conductivity (S/m) and ρ_{m} is the mass density (kg/m^3) of tissue. However, at present, a small, isotropic, implantable electric field probe has yet to be developed with sufficient sensitivity for practical use. Consequently, a common practice in experimental dosimetry relies on the use of temperature elevation produced under a short-duration ($<$30 sec), high-intensity exposure condition. The short duration is not enough for

significant convective or conductive heat contribution to tissue temperature rises. In this case, the time rate of initial rises in temperature (slope of transient temperature response curve) can be related to SAR through a secondary procedure, that is,

$$\text{SAR} = \frac{c\Delta T}{\Delta t} \tag{10.2}$$

where ΔT is the temperature increment (°C), c is the specific heat capacity of tissue (J/kg °C), and Δt is the duration (sec) over which ΔT is measured. Thus, the rise in tissue temperature during the initial or a transient period of RF energy absorption is linearly proportional to the value of SAR. It is important to distinguish the use of SAR and its derivation from temperature measurement. The quantity of SAR is merely a metric for energy deposition or absorption, and it should not be construed to imply any mechanism of interaction, thermal or otherwise. However, it is a quantity that pertains to a macroscopic phenomenon by virtue of the use of bulk electrical conductivity in its derivation (Equation 10.1).

It is of particular significance to emphasize the use of bulk electrical conductivity, the specific heat capacity, and the mass density (kg/m^3) of tissue in the derivation of SAR from electric field strength or temperature elevation. Their use in the definition means that a volume of tissue mass must be selected over which SAR is determined. It is self-evident that the numerical value of SAR would be the same, regardless of what volume is chosen, if the induced field or power deposition is uniform in a tissue medium. A difficulty arises when the absorption is not uniform or when tissues with differing properties and conductivities are within the same volume. Thus, in general, a smaller averaging mass or volume would allow SAR—as a metric—to provide a closer representation of its variation inside the body or tissue medium.

10.1.2 Characterizing EMFs

The space surrounding a source antenna can be divided into near and far zones as a function of distance from the antenna [3]. The demarcating boundary occurs at a conservative distance of $R = 2D^2/\lambda$, where D is the largest dimension of the antenna. Furthermore, the near zone can be divided into two subregions: the radiative region and the reactive region. In *the radiative region*, the region closer than $2D^2/\lambda$, the radiated power varies with distance from the antenna. The vicinity of the antenna where the reactive components predominate is known as *the reactive region*. The precise extent of these regions varies for different antennas. For most antennas, the transition point between reactive and radiative regions occurs from 0.2 to $0.4D^2/\lambda$. For a short dipole antenna, the reactive component predominates to a distance of approximately $\lambda/2\pi$, where the radiative and reactive components are equal to each other. However, the outer limit is on the order of a few wavelengths or less in most cases.

A typical wavelength in free space at extremely low-frequencies (ELF between 3 Hz and 3 kHz) is ~5000 km. The $\lambda/2\pi$ distance is about 800 km for the induction and radiation fields to have equal amplitudes. Therefore, for most purposes, ELF transmission line fields are not radiative but are inductive and quasi-static in nature. This fact governs the coupling and induced field characteristics of ELF and other low-frequency electric and magnetic fields in biological tissue. In particular, (1) the electric field is enhanced at the surface of the biological body and is nearly perpendicular to the surface of the body, (2) electric and magnetic fields are decoupled inside a biological body, (3) the electric field applied through air is weakened by a large dielectric permittivity (by about 10^{-6}) upon penetration into biological tissues, (4) the magnetically induced electric field encircles the

magnetic field and produces an eddy current whose magnitude increases with distance from the center of the body, and (5) an eddy current appears in each region inside the body with a different conductivity and behaves as a unit with its own body center and radius or an equivalent radius. These observations apply to all frequencies where the wavelength is high or the largest dimension of the body is small compared with the wavelength [2]

In contrast, the $2D^2/\lambda$ distance is approximately 6 cm for a 10-cm RF antenna operating at 900 MHz in free space. Clearly, both near-zone reactive and far-zone radiative interactions are encountered in the vicinity of wireless RF telecommunication systems. In the near zone, the coupling of RF energy into the human head is substantial. As much as 40% to 50% of the radiated RF power is transferred back and forth between the radiating antenna and the head. SAR will vary with specific antenna configuration and its placement next to the head. The bulk of power deposition is on the side of the head nearest to the radiating structure of the cellular mobile telephone and follows an exponential trend away from the antenna side. The anatomy of the head and tissue inhomogeneity can influence the maximum value and distribution of SAR in the head of a mobile telephone user. However, the integrated SAR in the head is similar for a homogenous or inhomogenous model. Some of the major features of near-zone field are that (1) RF electric and magnetic fields are decoupled and are not uniform, (2) wave impedance varies from point to point, (3) beam width from the antenna is divergent and is small compared with the head or human body, (4) electric field ffect is weaker since dielectric permittivity of tissue is relatively high, and (5) inductive coupling of antenna-current-generated magnetic field dominates power deposition.

In the far field, coupling is characterized by plane wave RF field interaction and is independent of source configurations. Electric and magnetic fields are uniquely defined through the intrinsic impedance of the medium. Thus, determination of the electric field behavior is sufficient to characterize the interaction. The coupling of RF power from air into planar tissue ranges from 20% to 60% at wireless communication frequencies. However, enhanced coupling can occur at a greater depth in bodies with curved surfaces. In fact, RF energy is resonantly absorbed by the head at 400 to 1500 MHz, and SAR peaks or hot spots may occur near the center of the head. The interaction of RF energy with biological systems depends on electric field polarization for elongated bodies whose height-to-width ratio is large. It is significant to observe that the integrated SAR or total absorption in the biological body is similar for a homogenous and inhomogenous model.

10.2 Planar Tissue Models

When the radius of curvature of the body surface is large compared to the wavelength and beam width of the impinging radiation, planar tissue models may be used to estimate the absorbed energy and its distribution inside the body. As a first-order approximation, the plane wave configuration is often used for its simplicity to assess EMF interaction with planar biological tissues. This section presents a summary of specific results that have been obtained, using analytical approaches, for thick or semi-infinite layers and for multilayered planar models of biological tissue structures.

10.2.1 Thick or Semi-Infinite Layers

The reflection and transmission of a plane wave at a planar tissue interface depend on the frequency, polarization, and angle of incidence of the wave and on the dielectric constant and conductivity of the tissue. For a linearly polarized plane wave impinging normally on

a boundary separating two semi-infinite media, the reflection and transmission coefficients are given by

$$\Gamma = \frac{\eta_2 - \eta_1}{\eta_2 + \eta_1} \tag{10.3}$$

and

$$T = \frac{2\eta_2}{\eta_2 + \eta_1} \tag{10.4}$$

respectively, where η_1 and η_2 are the intrinsic impedances ($= \sqrt{(\mu/\varepsilon)}$) of media 1 and 2. If intrinsic impedances of the two media are approximately equal or if the dielectric permittivities are comparable, most of the energy is transmitted into the second medium, and the reflected field is relatively small. Conversely, if intrinsic impedances differ greatly, or if the dielectric permittivities are very different, the transmitted field is small, and the quantity of reflected energy is large.

Table 10.1 summarizes the magnitude of the reflection coefficient at the boundary separating various tissues. The fraction of normally incident power reflected by the

TABLE 10.1

Reflection Coefficient (Magnitude in %) between Biological Tissues at 37°C

	Frequency (MHz)	Air	Fat (Bone)	Lung	Muscle (Skin)	Blood	Saline
Air	433	0	46	76	82	81	83
	915	0	43	73	78	79	80
	2,450	0	41	71	76	77	79
	5,800	0	39	70	75	76	78
	10,000	0	37	70	74	76	78
Fat (bone)	433		0	46	56	56	60
	915		0	43	52	54	57
	2,450		0	42	50	53	57
	5,800		0	42	50	53	56
	10,000		0	45	52	54	58
Lung	433			0	14	13	19
	915			0	12	14	18
	2,450			0	10	15	19
	5,800			0	10	14	19
	10,000			0	10	13	18
Muscle (skin)	433				0	4	6
	915				0	4	7
	2,450				0	5	10
	5,800				0	4	9
	10,000				0	3	9
Blood	433					0	6
	915					0	4
	2,450					0	5
	5,800					0	5
	10,000					0	6
Saline	433						0
	915						0
	2,450						0
	5,800						0
	10,000						0

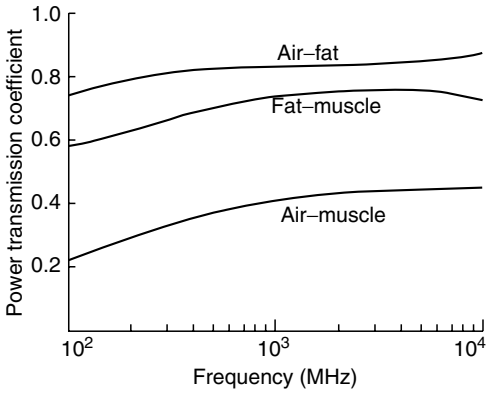

FIGURE 10.1
Power transmission coefficients at three tissue interfaces as functions of frequency.

discontinuity is given by Γ^2. Clearly, about one half of the incident power is reflected at these boundaries. Further, the reflection coefficient for tissue–tissue interfaces generally is smaller than for air–tissue interfaces. The percent reflected power for tissue–tissue interfaces ranges from a low of 5 for muscle–blood to a high of 50 for bone–biological fluid interfaces. This suggests that the closer are the dielectric properties on both sides of the interface, the smaller is the power reflection.

The fraction of power transmitted is related to the power transmission coefficient, T^2. It is readily apparent from Table 10.1 that the power transmitted at air–tissue interfaces is quite substantial at RF and microwave frequencies. Moreover, Figure 10.1 shows that the power transmission coefficient is highly frequency dependent, especially at lower frequencies.

As the transmitted wave propagates in the tissue medium, energy is extracted from the wave and absorbed by the medium. This absorption will result in a progressive reduction of the power density of the wave as it advances in the tissue. This reduction is quantified by the depth of penetration, which is the distance in which the power density decreases by a factor of e^{-2}. Table 10.2 presents the calculated depth of penetration in selected tissues using typical dielectric constants and conductivities. A graphical representation of penetration depth vs. frequency for blood, muscle, and fat is given in Figure 10.2. It is seen that the penetration depth is frequency dependent and takes on different values for different tissues. In particular, the penetration depth for fat and bone is nearly five times greater than for higher-water-content tissues.

TABLE 10.2

Depth of Penetration of an EMF in Biological Tissues as a Function of Frequency

	Tissue				
Frequency (MHz)	**Saline**	**Blood**	**Muscle (Skin)**	**Lung**	**Fat (Bone)**
Depth of Penetration (cm)					
433	2.8	3.7	3.0	4.7	16.3
915	2.5	3.0	2.5	4.5	12.8
2,450	1.3	1.9	1.7	2.3	7.9
5,800	0.7	0.7	0.8	0.7	4.7
10,000	0.2	0.3	0.3	0.3	2.5

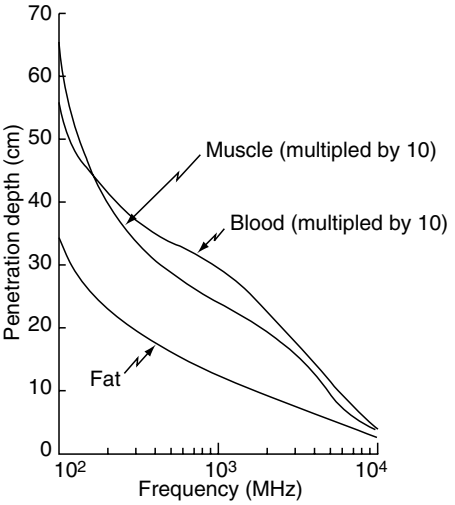

FIGURE 10.2
Depth of penetration for blood, muscle, and fat as functions of frequency.

A wave of general polarization usually is decomposed into its orthogonal linearly polarized components whose electric or magnetic field parallels the interface. These components can be treated separately and combined afterward. Figure 10.3 and Figure 10.4 illustrate the magnitude and phase of the reflection coefficients of representative tissue interfaces at a temperature of 37°C for irradiation at 2450 MHz. The figures clearly show the difference between *E* and *H* polarization. *E* polarization, also called perpendicular polarization, and *H* polarization, also referred to as parallel polarization, are defined in Chapter 1. For *E* polarization, there is only a slight variation in magnitude and phase of the reflection coefficient with incidence angle. For *H* polarization, however, there is a

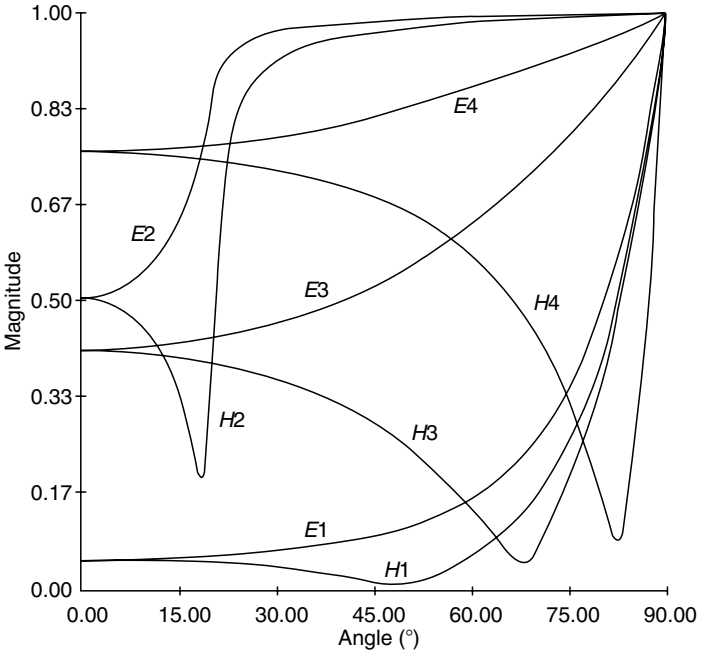

FIGURE 10.3
Magnitudes of reflection coefficients for *E*- and *H*-polarized plane waves at 2450 MHz.

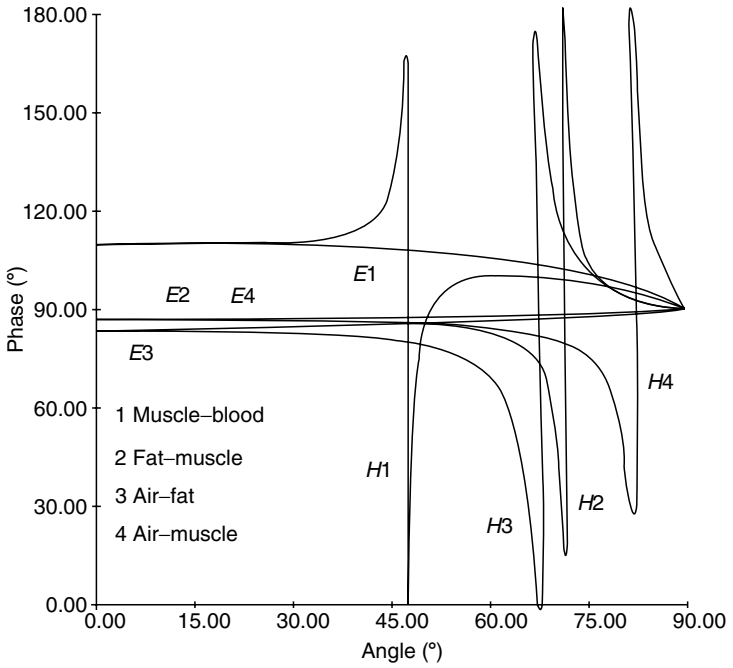

FIGURE 10.4
Phase of reflection coefficients for *E*- and *H*-polarized 2450 MHz plane waves.

pronounced dependence on incidence angle. The reflection coefficient reaches a minimum magnitude and has a phase angle of 90° at Brewster's angle. Thus, the *H* polarized wave is totally transmitted into the muscle medium at Brewster's angle.

10.2.2 Multiple Layers

When there are several layers of different tissues, the reflection and transmission characteristics become more complicated. Multiple reflections can occur between the skin and subcutaneous tissue boundaries, with a resulting modification of the reflection and transmission coefficients [4–7]. In general, the transmitted wave will combine with the reflected wave to form standing waves in each layer. This phenomenon becomes especially pronounced if the thickness of each layer is less than the penetration depth for that tissue. Plane waves impinging on the human body, considered as consisting of parallel layers of subcutaneous fat and more deeply lying muscle, have been studied in detail by Schwan and Li [5,6].

For the tissue model depicted in Figure 10.5, the electric field strength in the fat layer is given by

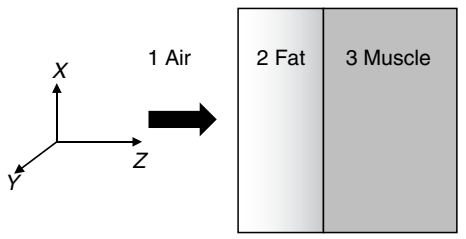

FIGURE 10.5
Plane wave impinging on a composite fat–muscle layer.

$$E_f = F_1 E_0 \left[e^{-(\alpha_2 + j\beta_2)z} + \Gamma_{32} e^{(\alpha_2 + j\beta_2)z} \right] \tag{10.5}$$

and the electric field in the underlying muscular tissue is given by

$$E_m = F_t E_0 e^{-(\alpha_3 + j\beta_3)z} \tag{10.6}$$

where α_2, β_2 and α_3, β_3 are the attenuation and propagation coefficients in fat and muscle, respectively. The layer function F_1 and the transmission function F_t are given by

$$F_1 = \frac{T_{12}}{e^{(\alpha_2 + j\beta_2)l} + \Gamma_{21}\Gamma_{32} e^{-(\alpha_2 + j\beta_2)l}} \tag{10.7}$$

$$F_t = \frac{T_{12}T_{23}}{e^{(\alpha_2 + j\beta_2)l} + \Gamma_{21}\Gamma_{32} e^{-(\alpha_2 + j\beta_2)l}} \tag{10.8}$$

where T_{12} and T_{23} are the transmission coefficients at the air–fat and fat–muscle boundaries, respectively. Γ_{21} and Γ_{32} denote the reflection coefficients at these boundaries, respectively; l is the thickness of the fat layer. The power deposition in a given layer can be obtained from Equation 10.1.

Figure 10.6 shows the results of SAR distribution obtained using the dielectric data given in part 1. The values are normalized to the SAR in muscle at the fat–muscle boundary. Note that the absorbed energy is much lower in fat than in muscle. The standing-wave maximum becomes bigger in fat, and the penetration into muscle becomes less as the frequency increases.

The electromagnetic energy absorbed in models composed of planar layers of skin, fat, and muscle can be analyzed in a similar manner [5–8], except that the distribution of

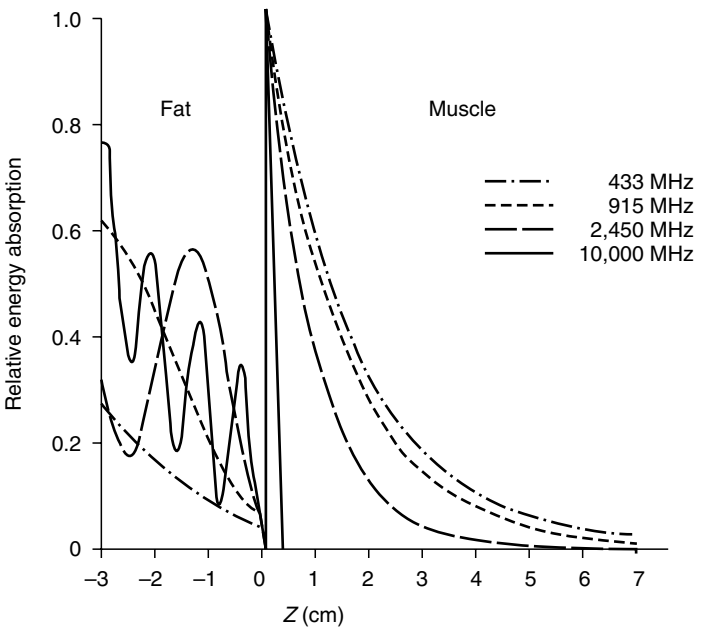

FIGURE 10.6
SAR (absorbed power density) in plane fat–muscle layers.

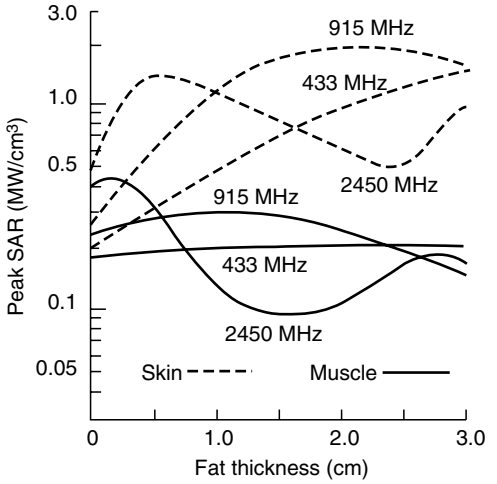

FIGURE 10.7
Peak SAR (absorbed power density) in models composed of fat–skin–muscle layers.

absorbed energy becomes more complex. Figure 10.7 shows that in addition to frequency dependence, the peak SAR exhibits considerable fluctuation with thickness of the subcutaneous fatty layer. The incident power density is, in this case, $10\,W/m^2$, and the skin layer is 0.2 cm thick. Note that the peak SAR is always higher in the skin layer for planar models at microwave frequencies. The depth of penetration for 10 GHz radiation in skin is less than 0.5 mm—the transmitted energy is almost completely absorbed in the skin, and the SAR is rather unaffected by changing fatty layer thickness. The fact that SAR is highest in the skin is significant, since skin is populated with thermosensitive free nerve endings, which may be excited along with cutaneous pain receptors when the absorbed energy exceeds the normal range that can be handled by thermoregulation.

Figure 10.8 shows the distribution of induced electric field strength in a layer of muscle beneath layers of fat, muscle, and bone for two frequencies [5–8]. It is seen that in addition

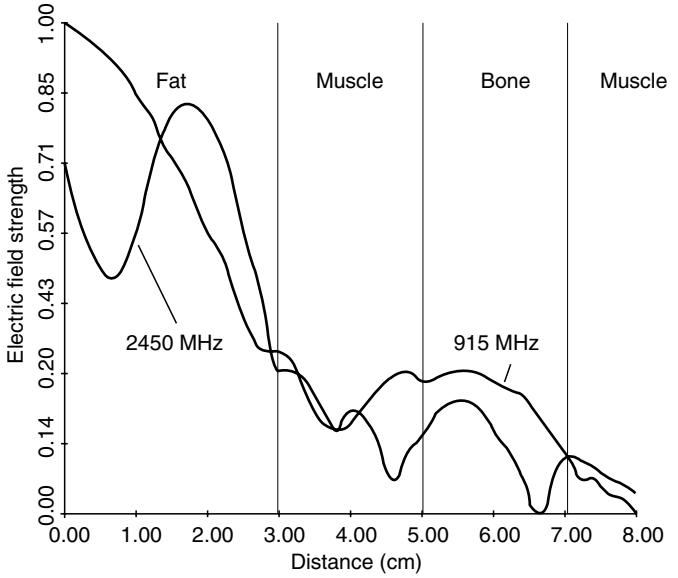

FIGURE 10.8
Distribution of electric field strength in planar layer of fat–muscle–bone–muscle tissue model.

to frequency dependence, the electric fields exhibit considerable fluctuation within each tissue layer. While the standing-wave oscillations are larger at 2450 than at 915 MHz, microwave energy at both frequencies penetrates to deeper tissues. This result, together with Figure 10.6 and Figure 10.7, implies that at frequencies between 300 and 3000 MHz, sufficient energy may be transmitted and reflected to allow examination of organs within the body. Furthermore, at these frequencies, electromagnetic energy can penetrate into more deeply situated tissues, making it especially desirable for therapeutic applications. They also call for special attention for safety considerations since electromagnetic energy in this frequency range can produce higher SAR at greater depth compared to superficial tissues.

10.3 Bodies of Revolution

Although depth of penetration and reflection and transmission characteristics in planar tissue provide considerable physical insight into the coupling and distribution of electromagnetic energy, biological structures generally are more complex in form and exhibit substantial curvature that can modify electromagnetic energy transmission and reflection. For bodies with complex shapes, the propagation characteristics depend critically on polarization and on orientation of the incident wave with respect to the body, as well as on the ratio of body size to wavelength. These complications place severe limitations on calculations of reflected and transmitted energy for bodies of arbitrary shape and complex permittivity. This section presents a summary of results for homogenous and multilayered models based on bodies of revolution that approximate certain mammalian tissue structures.

10.3.1 Spherical Models

Some representative calculations of the SAR are shown in Figure 10.9 for four different-sized models at 918 and 2450 MHz [7,8]. The 6-cm diameter sphere approximates a cat or rhesus monkey brain, and the 10-cm diameter sphere approximates the head of a child, while the 14- and 18-cm diameter spheres are more typical of human adult heads. The figures illustrate the SAR distributions along the three perpendicular axes whose origin coincides with the center of the sphere. An incident plane wave power density of $10\,\mathrm{W/m^2}$ is assumed. The plane wave is propagating in the positive z direction and is polarized along the x axis. It is seen that for 918 MHz, maximum absorption occurs near the center or inside of all the brain spheres. When the frequency is increased to 2450 MHz, the location of peak SAR for the cat-size brain sphere remains near the center, whereas that for a human-size brain sphere is moved to an anterior location.

In general, standing-wave patterns with many oscillations are observed. Note that while peak and average SARs in the cat brain are larger by a factor of 2 than in the human brain at 918 MHz, at 2450 MHz the peak absorption is four times and the average absorption is three times greater in the cat brain than in the human brain. Other studies [9–12] indicate that the peak absorption may be as much as five times greater than the average, and the enhanced absorptions near the center of these brain models may be two to three orders of magnitude greater than that expected from the planar tissue models. The increased absorptions are due to a combination of high dielectric constant and curvature of the model, which produces a strong focusing of energy toward the interior of the sphere that more than compensates for the transmission losses through the tissue.

The peak absorption per unit volume, average absorption per unit volume, and average absorption per unit surface area as functions of frequency and radius of the spherical brain model are illustrated in Figure 10.10. It can be seen that the absorbed energy varies widely with sphere size and frequency. In general, the absorption increases rapidly with increasing radius and is then followed by some resonant behavior. The peaks of these resonant oscillations are related to the maxima, or hot spots, in the distribution of absorbed energy inside the head model, as shown in Figure 10.9. Therefore, for $(2\pi a/\lambda_0) < 0.4$, where a is the sphere radius and λ_0 is the wavelength in vacuum, hot spots do not occur inside the sphere. However, for some combinations of irradiation frequency and radius, hot spots will occur, for example, in spheres with radii between 2 and 8 cm at 918 MHz and between 0.9 and 5 cm at 2450 MHz. For spheres whose radii exceed the size ranges mentioned above, the maximum absorption appears at the anterior portion (exposed surface) of the sphere, and the penetration depth at the surface becomes a dominating factor for exposures at frequencies in this range. The planar model discussed previously may be applied to obtain a theoretical estimation of the absorbed energy in this case.

The frequency dependence of energy absorption is illustrated in the upper graphs in Figure 10.10 for the head of a small animal, such as a cat or rhesus monkey, and a sphere the

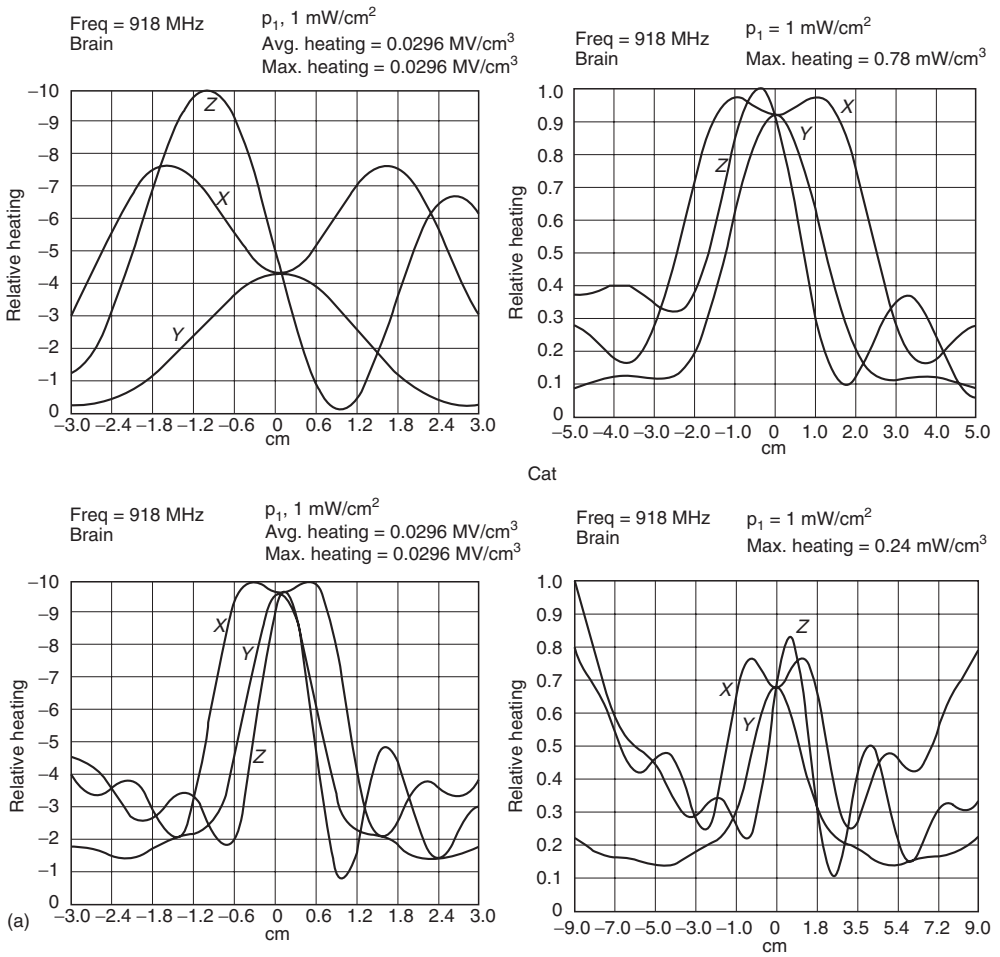

FIGURE 10.9
(a) Predicted SAR distribution (heating pattern) along the three rectangular axes of spherical models of brain exposed to 918-MHz uniform plane waves.

continued

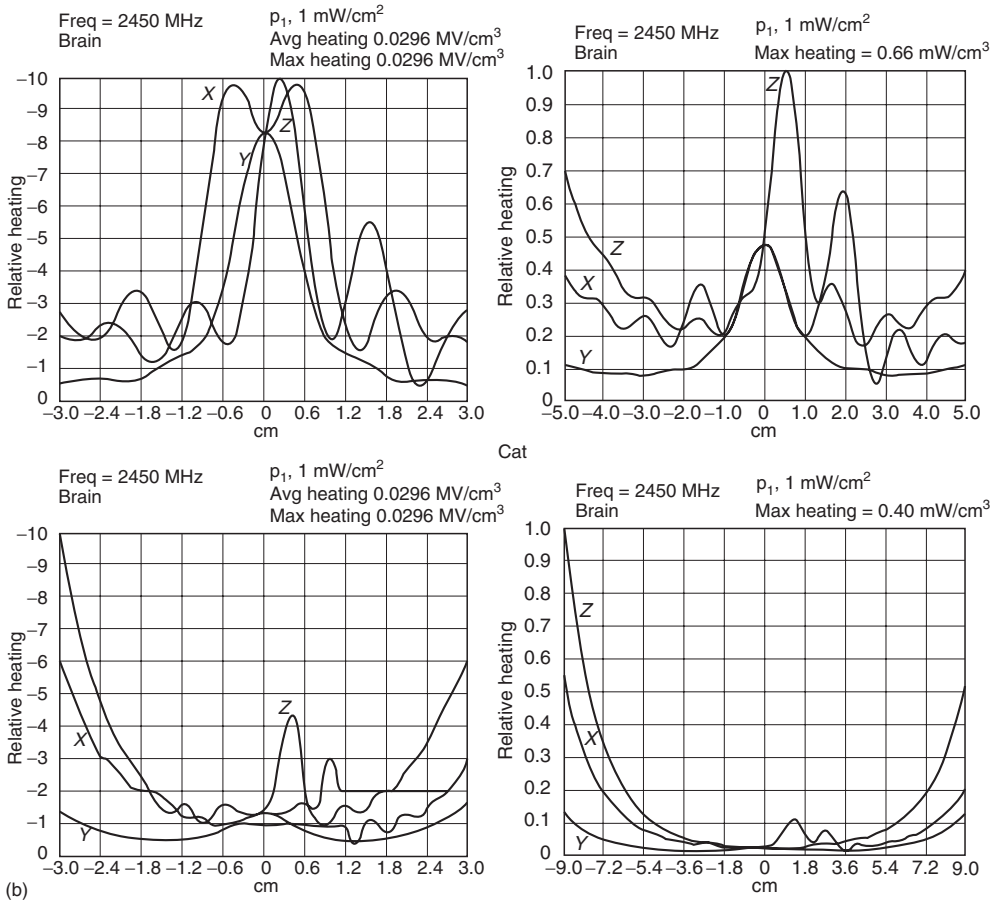

FIGURE 10.9 (continued)
(b) Predicted SAR distribution (heating pattern) along the three rectangular axes of spherical models of brain exposed to 2450-MHz uniform plane waves.

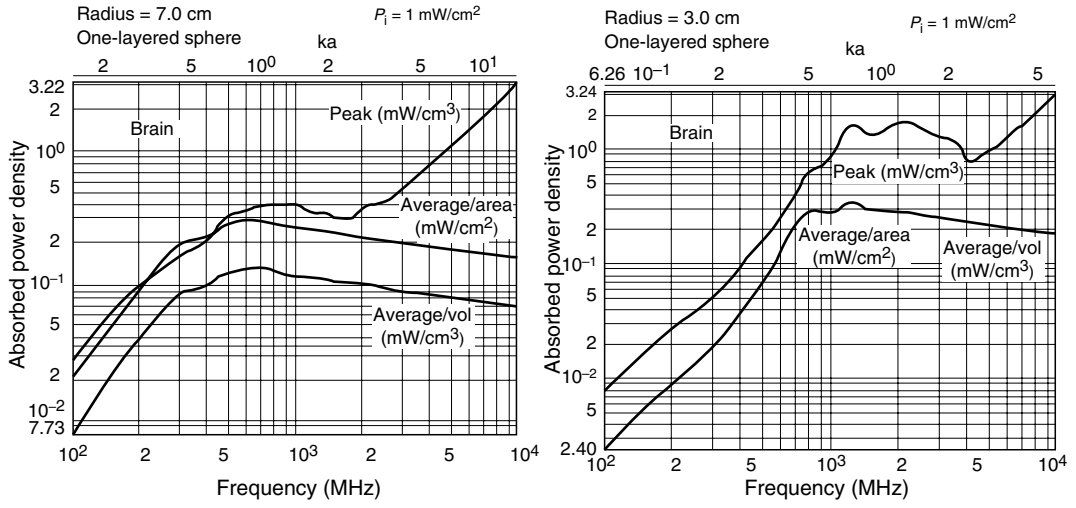

FIGURE 10.10
Electromagnetic energy absorption characteristics for spherical models of brain.

size of a human head. Besides the occurrence of resonant peaks, with increasing frequency, energy is absorbed in a decreasing volume as a result of shortened penetration depth.

The effects of skin, fat, bone, dura, and cerebrospinal fluid on the absorption of RF radiation by the brain have been investigated in several laboratories [9,13–15], using more complex spherical structures where the spherical core of brain is surrounded by five concentric shells of tissues. It is interesting to note that if brain sizes remain unchanged, but the overall sphere diameter is increased to account for the outer tissue layers, absorption in brain tissues may be increased by 25% for human- and cat-size heads at 918 MHz or decreased by 70% or more in the case of 2450 MHz. Moreover, surface absorption is greatly increased in the case of layered models, while fat and bone always absorb the least amount of energy.

If the outer diameter of the sphere remains the same, while the tissue layers are allowed to be either layered or homogenous, the peak and average SARs show very little change except when the radius of the spherical head is between 0.1 and 1.0 times the wavelength in air. The peak and average SARs for layered models may be several times greater than for homogenous models. Enhancement is apparently the result of resonant coupling of energy into the sphere by the outer tissue layers.

A study also has been made of the interaction of circularly polarized plane electromagnetic waves with six-layered spherical models of the mammalian head [15]. The approach is a classic one; Mie equations were modified to account for the two polarizations that are orthogonal in space. For example, calculations at 918 and 2450 MHz for a 7-cm diameter sphere representing a cat or monkey head and a 20-cm diameter sphere typical of a human adult head indicated that the maximum absorption for 918 MHz occurs near the center of a cat-size head, whereas the maximum absorption for a human-size head is at the surface, as in the case of linearly polarized plane waves. However, at 2450 MHz the location of maximum absorption for both the smaller and the larger spheres shifts to the leading surface. The distribution of absorbed energy for circularly polarized waves is more uniform compared with the linearly polarized case. In fact, the absorbed energy distribution in the planes transverse to the direction of propagation is rotationally symmetric, that is, it is independent of angular variation. Note also that the maximum energy absorbed in the spherical head models varies only slightly between these two frequencies. However, a greater quantity of energy is deposited in the inner sphere (representing the brain of a human head) for 918- than for 2450-MHz radiation.

Spherical models of muscle [16,17] have been used as a first-order approximation for the extrapolation to human beings of results obtained from laboratory animals and as an index of whole-body absorption of electromagnetic energy as a function of frequency. The spherical model is attractive since exact solutions for absorbed energy can be obtained for all frequencies and body sizes. While in this case the peak absorption is of very limited utility, the average absorption per unit surface area is related to the time and power required to overload the thermoregulatory capacity of an exposed subject. The absorptions for homogenous muscle spheres, whose volumes correspond to small animals, such as a rat, and standard man, computed as functions of frequency, showed that the average absorption for the rat model is at least ten times higher than for a muscle sphere representing a human body at frequencies greater than 500 MHz. The absorption increases rapidly with frequency until the free space wavelength of the impinging radiation approaches the diameter of the sphere. A number of resonant oscillations appear that tend to increase the amount and nonuniformity of absorbed energy. Above this range the absorption falls off slowly, indicating that details of body surface curvature are of little significance.

We have, thus far, dealt mainly with situations where the diameter of the sphere is comparable to or larger than the wavelength in air. It is interesting to note that when the sphere is small compared with the wavelength, the absorbed energy distribution varies

almost as the square of the radius or distance from the axis parallel to the direction of the magnetic field vector. If the sphere is extremely small compared with the wavelength, the absorbed energy distribution becomes nearly uniform in the transverse directions but decreases continuously with distance from the exposed surface. This behavior can be explained by a quasi-static field theory [16]. The electric component of the incident field couples to the object in the same fashion as an electrostatic field. This gives rise to a constant induced electric field inside the sphere that has the same direction but is reduced by $3/\varepsilon$ from the applied electric field for biological materials and is independent of sphere size. Similarly, the magnetically induced electric field inside the body is identical to the quasi-static solution whose magnitude is given by $E = \pi f \mu r H$, where f is the frequency, μ is the permeability, r is the radius, and H is the magnetic field component. Thus, the magnetic component of the incident field produces an internal electric field that varies directly with distance from the axis and in proportion to the frequency. This magnetically induced electric field encircles the magnetic axis and gives rise to an eddy current whose magnitude increases with distance from the y axis. It indicates that while the H-induced energy absorption in a mouse or larger animal is much greater than the E-induced component, electrically and magnetically induced absorption may be equally significant in smaller animals at lower frequencies (below 30 to 40 MHz). Moreover, for a small insect or pupae the electric field will be the predominant factor.

The variation of average and maximum energy absorption with frequency for a human-size sphere is illustrated in Figure 10.11. In the frequency range from 1 to 20 MHz, the maximum absorption rate is only 10^{-6} to 10^{-3} (W/kg)/(W/m^2) of incident power. Inspection of the maximum absorption rate induced by a plane wave, a quasi-static electric field, and a quasi-static magnetic field shows that absorption at frequencies below 20 MHz is primarily due to the magnetically induced eddy current and is characterized by a square-of-frequency dependence. The approximate frequency dependence of average or total energy absorption throughout the frequency range from 1 MHz to 10 GHz is indicated by the dashed line. For frequencies below 20 MHz the average absorption varies as the square of the frequency. In the frequency range of 20 to 200 MHz, the average absorption increases directly in proportion to frequency and attains a maximum of about 2×10^{-3} (W/kg)/(W/m^2) of incident power at 200 MHz. The average absorption rate remains fairly constant with increasing frequency. (Its slow variation is inversely proportional to frequency for higher frequencies.) There is thus little doubt that electromagnetic energy absorption varies both with frequency and with body size, and in a predictable manner.

10.3.2 Prolate Spheroidal Models

Since the bodies of humans and experimental animals are seldom spherical in shape, a better geometric model is needed to analytically and numerically describe the induced fields and absorbed energy inside experimental subjects. A prolate spheroid emulates more closely the shape of mammalian bodies, but most analyses have been restricted to homogenous models for humans and experimental animals [18–22]. As in the case of spherical models, for frequencies below resonance, long-wavelength formulations [19,20] and quasi-static approximations [22] have been used to obtain absorption information. Geometric optics approximations also have been developed for computation of absorption characteristics of prolate spheroidal models of humans at frequencies whose wavelengths are short compared with body size [21].

Three orientations of the impinging plane wave with respect to the body must be distinguished: E-polarization, in which the electric field is parallel to the major axis of

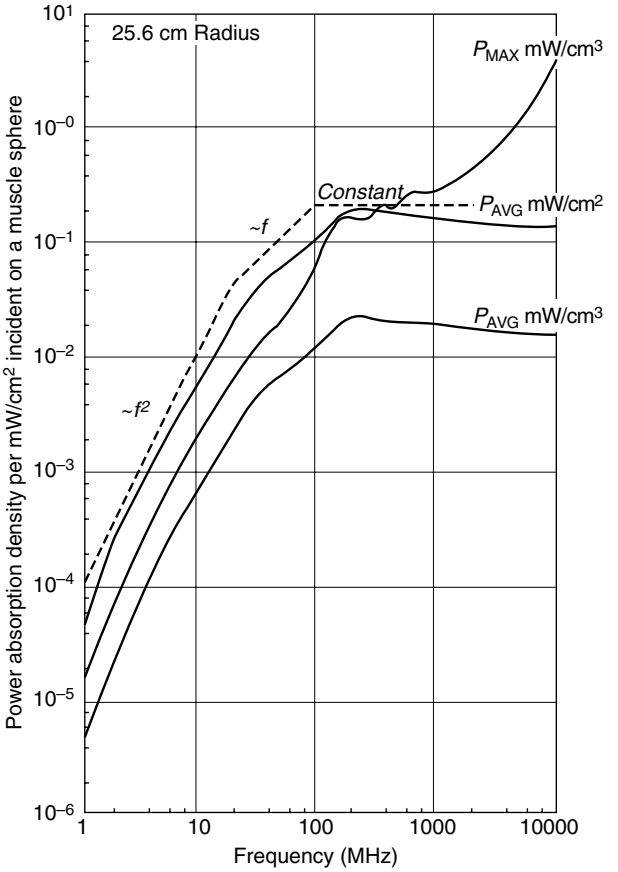

FIGURE 10.11
Frequency dependence of absorption in a spherical model of the human body.

the spheroid; *H*-polarization, in which the magnetic field vector is parallel to the major axis; and *K*-polarization, in which both electric and magnetic field vectors are perpendicular to the major axis of the spheroid. In general, *E*-polarization produces the highest energy absorption for frequencies up to and slightly beyond the resonance region.

For a plane wave with long wavelength, that is, $\lambda > a$, where a is the semimajor axis of the prolate spheroid, the induced fields within the spheroid are uniform and independent of size when the external field is uniform. For $\varepsilon_r > 1$, the field inside the spheroid is weaker than the applied field. Moreover, the whole-body energy absorption depends not only on the strength of impressed fields but also on the orientation of the field with respect to the major axis of the body. As in the case of spherical models, the absorption is produced by an electrically induced current in the direction of the applied *E*-field vector, combined with a circulating eddy current induced by the incident magnetic field [16]. One would therefore expect the electrically induced absorption to be uniform, whereas the absorption due to the circulating eddy current would be zero at the center of the body and increase as the square of the distance from the center.

Note that for a given incident field orientation, the average SAR for humans may be either higher or lower than for rats, depending on the frequency. For example, at 70 MHz, the average SAR is the highest for humans, having a value of 0.25 W/kg for an incident power density of 10 W/m^2; the average SAR for a rat is only 0.0125 W/kg. In contrast, the average SAR of 0.8 W/kg at 700 MHz is the highest for rats; the corresponding value for humans is less than 1/25. It is thus extremely important to take into account the body size

and operating frequency to draw any relationship between the biological effects that arise in the laboratory and the corresponding effects that might occur in humans at a given incident power density [1,2].

The frequency for maximal absorption (resonance frequency) depends on the subject and its orientation with respect to the incident field. In general, the shorter the subject, the higher the resonance frequency and vice versa. Further, the frequency dependence of whole-body or average absorption may be partitioned into three regions. This may be illustrated using the orientation that is most efficient in energy coupling, *E*-polarization. For frequencies well below resonance such that the ratio of the longest body dimension (L) to free space wavelength (λ) is less than 0.2, the average SAR is characterized by an f^2 dependence. The average absorption goes through a resonance in the region where $0.2 < L/\lambda < 1.0$. In this case, the average SAR rapidly increases to a maximum near $L/\lambda = 0.4$ and then falls off as $1/f$. At frequencies for which $L/\lambda > 1.0$, the whole-body absorption decreases slightly but approaches asymptotically the geometrical optics limit of about one half of the incident power (1 − power reflection coefficient).

It should be noted that the resonant absorption length of 0.4λ is in good agreement with results from antenna analysis. In addition, whole-body absorptions for *H*- and *K*-polarizations are totally different. The resonances are not nearly as well-defined as for *E*-polarization. In fact, the whole-body absorption curve for *H*-polarization gradually reaches a plateau and stays at that plateau for higher frequencies.

At 10 MHz, the size of the spheroidal model approximating an average human body—height equals 1.75 m with a major-to-minor axis ratio of 6.34 and a 70-kg mass—is small compared with the wavelength. The distribution of absorbed energy in the spheroidal model is qualitatively similar to that for spherical models. But quantitatively, the difference could be as much as one order of magnitude. As expected, the absorbed energy is highest for *E*-polarization. There is a strong coupling of the applied electric field into the interior of the prolate spheroid, and a relatively weak eddy current contribution due to a smaller cross section for intercepting the magnetic flux. The current distribution along the direction of incident field indicates that the electrically and magnetically induced field components are nearly equal. The electric polarization field and the circulating eddy current add at the front side and subtract on the back side of the spheroid to render an absorption pattern that peaks at the front surface and is reduced to almost zero deeper inside the spheroid.

For *H*-polarization, the electrically induced current flows along the x axial direction of incident **E** field, and the eddy current field encircles the z axial direction of incident **H** field. The relatively low power on the z axis comes solely from the incident electric field. The combination of *E*- and *H*-induced components generates a displaced parabolic energy absorption pattern along both the x and the y axes. Clearly, the magnetically induced eddy current predominates in this case, and the absorption is highest along the transverse circumference at the middle of the prolate spheroid. For *K*-polarization, both the electric and the magnetic components of the incident field are along the minor axes of the spheroid: the electrically induced current flows along one axis, and the incident magnetic field induces an eddy current electric field that encircles another axis. The absorption is lowest at the center. Whereas in both *E*- and *H*-polarization cases, the peak absorption occurs at the front surface of the spheroid irradiated by the incident field, this is not the case for *K*-polarization. Maximum absorption appears at the surface of the narrow cross section, and the absorbed energy varies parabolically. This is the result of the large quantity of magnetic flux intercepted by the broad cross section (and the resulting concentration of eddy current). It should be noted that the results match very well with experimental measurements [23]. Moreover, the peak absorptions may be two orders of magnitude higher than those for dielectric spheres of equal mass.

10.4 Anatomically Based Models

We have summarized above some of the computational approaches to quantify the absorbed energy in simple models of biological objects. It should be recognized that while spheres and spheroids are good models of some animal bodies and certain body parts, they may not always be adequate for humans and experimental animals under a variety of exposure situations. More realistic models, such as models of human bodies formed from small-sized, computational-cell volumes have been developed to account for the irregular shapes [24–28]. These models, based on numerical techniques have been a great asset in efforts to accurately predict energy absorption and its distribution in biological objects exposed to EMFs and RF radiation. In what follows we shall summarize a number of computer techniques that have been applied with some success in solving electromagnetic energy absorption and SAR distribution problems. We shall also describe some results obtained using these methods.

10.4.1 Brief Survey of Numerical Methods

The numerical methods used to predict induced fields in biological bodies of realistic shape and composition include the quasi-static impedance method, the method of moments (MoM), the finite element method (FEM), and the finite difference time domain (FDTD) method. Note that the quasi-static impedance method is restricted to lower frequencies (<30 to 40 MHz for the human body), but the MoM, the FEM, and the FDTD method may be used for any frequency of interest. In addition, both the finite element and the FDTD methods involve solving Maxwell's equations in the differential form for the computation of induced fields.

10.4.1.1 Quasi-Static Impedance Method

For low-frequency situations, where the dimensions of the biological body are small compared to the wavelength, the impedance method has been found to be highly efficient as a numerical procedure for calculating internal current densities and induced electric fields [29–33]. In this method, the biological body or the exposed part thereof is represented by a three-dimensional (3-D) network of impedances whose individual values are obtained from the complex conductivities $\sigma + j\omega\varepsilon$ for the various locations of the body. The impedances for various directions for the 3-D network can be written as

$$Z_m^{i,j,k} = \frac{\delta_m}{\delta_n \delta_p (\sigma_m^{i,j,k} + j\omega\varepsilon_m^{i,j,k})} \tag{10.9}$$

where i, j, k indicate the cell index; m is the direction in x, y, or z for which the impedance is calculated; and σ_m and $j\omega\varepsilon_m$ are the conductivities and the dielectric permittivities for the cell (i,j,k). δ_m is the thickness of the cell in the mth direction, and δ_n and δ_p are the widths of the cell in directions at right angles to the mth direction.

In the impedance method formulation, it can be seen that the cells need not be identical so that fairly thin features of the body can be modeled as well as the interfaces between the various tissues and organs. Also, the conductivity for a given cell can be directionally dependent. This feature will be useful in allowing for the highly anisotropic conductivities of the tissues that have been reported for low-frequencies including the power-line frequencies [34,35].

Employing anatomically based models of the human body, the impedance method has been used for the following applications:

1. Calculation of SAR distributions for operator exposure to spatially variable fields of induction heaters [31]
2. SAR distributions for linearly or circularly polarized RF magnetic fields representative of magnetic resonance imagers [32]
3. SAR distributions due to capacitive-type electrodes used for hyperthermia [33]
4. SAR distributions for interstitial RF needle applicators for hyperthermia [36]

Some calculations using the impedance method are listed below:

1. Internal electric fields and current densities induced in the human body by exposure to magnetic fields of high-voltage power transmission lines [37]
2. Electric fields and current densities induced in the human head by magnetic fields of a hair dryer [38]
3. Current densities induced in the arm and the body by magnetic fields of an electric hand drill [39]
4. Currents induced in the anatomically based model of the human body by the electric and magnetic fields of electric blankets [40].

In the section that follows, the use of the impedance method is described for calculating currents in models of the human body exposed to electric and magnetic fields of both the conventional (pre-1990) electric blanket and the new low-magnetic-field electric blanket.

10.4.1.2 Volume Integral Equation MoM

The MoM [41] is used in conjunction with either the volume integral equation method or the surface integral equation method for finding solutions to the unknown fields inside the body. The approaches differ, however, in specifics, in that the surface integral equation MoM (SMoM) finds the unknown currents on the body surface and calculates the interior fields from the surface currents, the reciprocity theorem, and a ''measurement matrix.'' In contrast, the volume integral equation MoM (VMoM) requires determination of unknown fields throughout the volume of the body using the volume equivalence principle and the MoM.

The numerical technique that has been adopted for most of the early field intensity computations is the VMoM, employing the volume equivalence principle [26,27,42,43]. The MoM is used to transform the integral equation into a matrix equation by subdividing the body into N simply shaped cells. This is accomplished with the aid of an appropriate set of expansion functions, chosen to satisfy the boundary conditions, and a set of weighting (testing) functions to reduce the matrix fill-in time. The total electric field in each of the N cells is given by matrix inversion. A more detailed description of the volume integral equation method is included in the next section.

However, it should be noted that a fundamental limitation of this method is the use of full or nearly full matrices and, therefore, the requirement of extensive computer storage and long running time. Even with the availability of larger and faster computers, this difficulty is not completely resolved. The need for excessively large numbers of mathematical cells to render a more accurate representation of the body will give rise to an equally large and full matrix. The inversion of large, full matrices often leads to numerical instabilities in the solution. Nevertheless, the method does allow the use of inhomogenous models

with up to 1000 cells. In fact, this method has been employed, successfully, to calculate whole-body averaged absorption and to obtain regional distribution of absorbed RF energy using inhomogenous block models composed of rectangular cells [29–28,44]. This method also has been used to study the interaction of the near-zone field of an antenna with biological bodies [45,46].

10.4.1.3 SMoM

Another approach for predicting the distribution of absorbed electromagnetic energy is the SMoM [47–50]. This method makes use of two coupled integral equations, that is, the electric field and magnetic field integral equations for the tangential components of the field on the surface separating the biological body from air. The unknown surface currents are found by Fourier decomposition and the moment method. The fields inside the biological body are calculated using the previously computed surface currents, the reciprocity theorem, and the concept of measurement matrix [48,51–53].

The method begins with the matrix representation of the coupled integral equations. If the body is assumed to be rotationally symmetric, the incident wave and the induced current could then be expanded in a Fourier series expansion in the angle of rotation. This reduces the problem to that of solving a system of orthogonal modes. The method further expands the surface components in terms of triangular expansion or basis functions and allows the testing functions to be the complex conjugate of the basis functions taking advantage of the orthogonality property. Thus, the major advantage of introducing the Fourier series is to enable each mode to be treated completely independently of all other modes. This results in a much smaller-size, manageable matrix equation to be evaluated for the unknown expansion coefficients that determine the surface currents. It should be noted that for biological bodies, triangular expansion and testing functions are preferred over flat pulse expansion functions [47,48]. In fact, an expansion function with a continuous first derivation may constitute an even better choice for the expansion basis function. In any event, once the surface currents are obtained, the fields everywhere, or SAR at each point inside the body, can be calculated using the reciprocity theorem [52,53]. The total absorption can be found by integrating the surface Poynting vector.

The validity of SMoM has been substantiated by using a dielectric sphere [47]. Calculations for a human torso modeled by a homogenous muscle body of revolution with a height of 1.78 m at 30, 80, and 300 MHz showed enhanced absorption in the neck region for all three frequencies and both vertical and horizontal polarizations [48]. Note that the vertical direction is aligned with the long dimension of the torso and serves as the axis of symmetry. The strongest absorption in the torso model was found to occur with vertical polarization and near the first resonance frequency of the torso (80 MHz). In general, the surface integral equation method is applicable to any arbitrarily shaped homogenous body of revolution. The method can be used not only with incident plane waves but also with a wide variety of other field exposure conditions, including direct contact situations and near-zone sources.

Since both the surface and volume integral equation methods for field intensity prediction rely on the MoM for implementation, it is instructive to compare the relative advantages of these two techniques. For simplicity, consider a homogenous cube with N samples on each side: the computer storage requirements are N^2 and N^3 for the surface and volume integral methods, respectively [48]. For sufficient sampling to ensure accurate description of field variations, N is usually a large number. Thus, the surface integral equation method requires significantly fewer unknowns for homogenous models. Moreover, in cases where permittivity and conductivity values are large, such as in biological bodies, the wavelength becomes contracted inside the body, and a much larger number of cells than that indicated above may actually be needed. If the model is inhomogenous,

then the volume integral equation would prove to be more suitable. It is possible, however, to generalize the surface integral equation technique to account for inhomogeneities by employing the invariant imbedding procedure [54].

10.4.1.4 FEM

The FEM has been a preferred numerical algorithm in many fields of application. However, its use and popularity in predicting field intensities in biological systems have been modest until recent progress in mesh generation, boundary conditioning, and large matrix solvers. The FEM method is a near-neighbor, volume method for solving Maxwell's differential equations and is associated with a sparse system of equations [55,56]. Aside from the low memory requirement (on the order of N), an inherent attraction of FEM is its adaptability in modeling inhomogeneities and complex geometries. The feature of conforming and the variable-sized cell elements of the computational volume are extremely important in bioelectromagnetics.

The basic approach of the FEM method for predicting EMF distributions inside biological bodies starts by subdividing the physical space and biological body of interest into meshes of small volumes or cells of tetrahedral elements. This step is very important since the manner in which the volume is subdivided will dictate the computational resources required and the speed of the computation and accuracy of the results. Each cell element and node location will have to be systematically numbered and described. Once the volume has been subdivided, labeled, and the appropriate property values ascribed, the unknown field within each element is then approximated using linear extrapolation. A major step in FEM is the formulation of the system of linear equations using either the Ritz or the Galerkin algorithm with proper boundary conditions. There are two approaches to solve the system of linear algebraic equations: the direct method of Gaussian elimination or the iterative method that starts with an initial guess. In practice, either method can produce an approximate solution to the unknown field intensity with a prescribed accuracy.

It should be noted that a large region exterior to the biological body is often encountered in bioelectromagnetic situations, where the biological body, or portion of it, is part of a region into which electromagnetic energy is radiated and scattered. The region of space exterior to the biological body and applicator must be truncated with an artificial boundary to limit the volume elements and the number of unknowns. Consequently, an appropriate boundary condition needs to be established at this artificial boundary for a unique finite element determination of the induced fields inside the body. The most common boundary conditions selected for this purpose are the absorbing boundary conditions that minimize the nonphysical reflections from the artificial boundaries by making boundaries transparent to the scattered field.

Fairly large-scale calculations, on the order of 200,000 elements, have been conducted effectively in the workstation-computing environment. Specifically, detailed power deposition patterns have been simulated in full and partial models of the human body undergoing electromagnetic hyperthermia treatment for cancer [57]. In this case, the cell elements were generated from computerized tomographic data obtained on human patients.

10.4.1.5 FDTD Method

The FDTD approach is an attempt to solve Maxwell's curl equations by directly modeling propagation of waves into a volume of space containing the biological body. By repeatedly implementing a finite difference representation of the curl equations at each cell of

the corresponding space lattice, the incident wave is tracked as it first propagates to the body and then interacts with it through surface current excitation, transmission, and diffraction. This wave tracking process is completed when the steady-state behavior is observed at each lattice cell. Considerable simplification is achieved by analyzing the interaction of the wavefront with a part of the body surface at a time, rather than attempting a simultaneous solution of the entire problem.

The FDTD method has become one of the most successful methods for SAR calculations. The method was first proposed by Yee [58] and later developed by Taflove [59–61], Holland [62], and Kunz and Lee [63]. Several books [64–66] are devoted to the FDTD method and some of its applications. For bioelectromagnetic applications the FDTD method has been found to be extremely versatile and has been used for whole-body or partial-body exposures due to spatially uniform or nonuniform fields (far or near fields), sinusoidally varying EMFs, and transient fields such as ultra-wide-band (UWB) and electromagnetic pulses (EMPs) [67–71]. Accordingly, some details of FDTD are included in this section.

10.4.1.5.1 The Traditional FDTD Method

In this method, the time-dependent Maxwell's curl equations

$$\nabla \times \mathbf{E} = -\mu \frac{\partial \mathbf{H}}{\partial t} \tag{10.10}$$

and

$$\nabla \times \mathbf{H} = \sigma \mathbf{E} + \varepsilon \frac{\partial \mathbf{E}}{\partial t} \tag{10.11}$$

are implemented for a lattice of subvolumes or Yee ''cells'' that may be cubical or parallelepiped with different dimensions, δ_x, δ_y, and δ_z in the x-, y-, or z-directions, respectively. The components of **E** and **H** are positioned about each of the cells as shown in Figure 10.12 and calculated alternately with half-time steps where the time

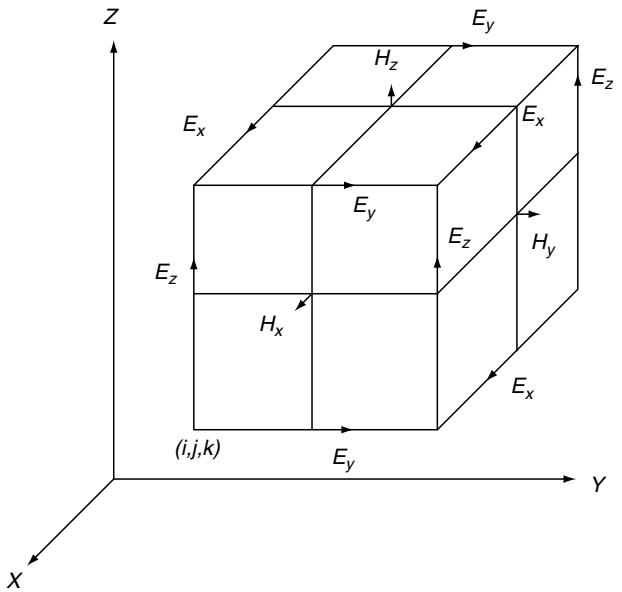

FIGURE 10.12
Unit cell of Yee lattice indicating positions for various field components.

step $\delta t = \delta/2c$. Here δ is the smallest of the dimensions used for any of the cells, and c is the maximum phase velocity of the fields in the modeled space. Since some of the modeled volume is air, c corresponds to the velocity of EM waves in air.

In the FDTD method, it is necessary to represent not only the scatterer or absorber, such as the human body or a part thereof, but also the EM sources, including their shapes, excitations, etc., if these sources are in the near-field region [70,71]. The far-field sources, on the other hand, are described by means of incident plane wave fields prescribed for a ''source'' plane [68,69], typically six to ten cells away from the exposed body. The source–body interaction volume is subdivided into Yee cells of the type shown in Figure 10.12. The interaction space consisting of several hundred thousand to a few million cells is truncated by means of absorbing boundaries. The prescribed incident fields are tracked in time for all cells of the interaction space. The solution is considered completed when either the fields have died off or, for sinusoidal excitation, when a sinusoidal steady-state behavior for **E** and **H** is observed for the interaction space.

The body of interest is mapped into the lattice space by first choosing the lattice increment and then assigning values of permittivity and conductivity to each cell. The boundary conditions at media interfaces are naturally generated by the curl equations. Thus, once a computer program is developed, the basic routines need not be changed for different model geometries. In fact, inhomogeneities and fine structural details could be modeled with a maximum resolution of one unit cell.

Time stepping for the FDTD method is accomplished by an explicit finite difference procedure [58,64]. For a cubic-cell lattice space, this procedure involves positioning the electric and magnetic field components about a unit cell of the lattice and then evaluating the components at alternate half-time steps. In this manner, centered difference expression can be used for both the space and the time increments without solving simultaneous equations to compute the fields at the latest time step.

The explicit formulation of the FDTD method is particularly suited for execution with minimum computer storage and run time using current array-processing computers. The required computer storage and run time increase only linearly with N, the number of cells. In fact, it has been shown that the FDTD method is capable of solving for more than 1 million unknown field components within a few minutes on an array-processing computer. Field intensities have been predicted to within 2.5% accuracy relative to known analytical and experimental bench marks. Recently, this FDTD technique has been improved to allow solutions for field penetration and absorption in large, complex, inhomogenous, and irregularly shaped biological bodies in three dimensions, with millimeter range spatial resolution. With the exception of a few early attempts with lossy biological objects [59,67], a majority of early efforts have been directed toward application of the FDTD method to electromagnetic interaction in time-varying inhomogenous media [60], and with metallic bodies of revolution [61]. However, during the last decade, the FDTD method has become the most extensively used numerical procedure for bioelectromagnetic computations.

10.4.1.5.2 Frequency-Dependent FDTD Formulation

For short pulses where wider bandwidths are generally involved, a frequency-dependent FDTD or $(FD)^2TD$ method is needed. Two general approaches have been used for the $(FD)^2TD$ method. One approach is to convert the complex permittivity from the frequency domain to the time domain and convolve this with the time domain electric fields to obtain time domain fields for the dispersive material. This discrete time domain method may be updated recursively for some rational forms of complex permittivity, which removes the need to store the time history of the fields and makes the method feasible. This method has

been applied to materials such as water, for which the permittivity may be described by a first-order Debye relaxation equation [72–74] or more complex materials with dielectric properties given by a second-order Lorentz equation with multiple poles [75].

A second approach is to add a differential equation relating the electric flux density **D** to the electric field **E** and solve this new equation simultaneously with the standard FDTD equations. This method has been applied to 1-D and 2-D examples with materials described by a first-order Debye equation or second-order single-pole Lorentz equation [76], and to a 3-D sphere and homogenous two-thirds muscle-equivalent man model with properties described by a second-order Debye equation [77,78]. In the following we describe this differential equation approach, which has now been used for induced current and SAR calculations for a heterogenous model of the human body [79].

The time-dependent Maxwell's curl equations used for the FDTD method have already been given as Equation 10.10 and Equation 10.11. The curl ***H*** can also be written as follows:

$$\nabla \times \mathbf{H} = \frac{\partial \mathbf{D}}{\partial t} \tag{10.12}$$

where the flux density vector **D** is related to the electric field through the complex permittivity $\varepsilon^*(\omega)$ of the local tissue by the following equation:

$$\mathbf{D} = \varepsilon^*(\omega)\mathbf{E} \tag{10.13}$$

Since Equation 10.10 and Equation 10.12 are to be solved iteratively in the time domain, Equation 10.13 must also be expressed in the time domain. This may be done by choosing a rational function for $\varepsilon^*(\omega)$, such as the Debye equation with two relaxation constants (see Chapter 1):

$$\varepsilon^*(\omega) = \varepsilon_0 \left[\varepsilon_\infty + \frac{\varepsilon_{s1} - \varepsilon_\infty}{1 + j\omega\tau_1} + \frac{\varepsilon_{s2} - \varepsilon_\infty}{1 + j\omega\tau_2} \right] \tag{10.14}$$

Rearranging Equation 10.14 and substituting in Equation 10.13 gives

$$\mathbf{D}(\omega) = \varepsilon^*(\omega)\mathbf{E}(\omega) = \varepsilon_0 \frac{\varepsilon_s + j\omega(\varepsilon_{s1}\tau_2 + \varepsilon_{s2}\tau_1) - \omega^2\tau_1\tau_2\varepsilon_\infty}{1 + j\omega(\tau_1 + \tau_2) - \omega^2\tau_1\tau_2}\mathbf{E}(\omega) \tag{10.15}$$

where the static (zero frequency) dielectric constant is given by

$$\varepsilon_s = \varepsilon_{s1} + \varepsilon_{s2} - \varepsilon_\infty \tag{10.16}$$

Assuming $e^{j\omega t}$ time dependence, Equation 10.15 can be written as a differential equation in the time domain:

$$\tau_1\tau_2 \frac{\partial^2 \mathbf{D}}{\partial t^2} + (\tau_1 + \tau_2)\frac{\partial \mathbf{D}}{\partial t} + \mathbf{D} = \varepsilon_0 \left[\varepsilon_s \mathbf{E} + (\varepsilon_{s1}\tau_2 + \varepsilon_{s2}\tau_1)\frac{\partial \mathbf{E}}{\partial t} + \varepsilon_\infty \tau_1\tau_2 \frac{\partial^2 \mathbf{E}}{\partial t^2} \right] \tag{10.17}$$

For the $(FD)^2TD$ method, Equation 10.10 and Equation 10.12 need to be solved subject to Equation 10.17. These equations can be written in the difference form [77,78] and solved to find **E**, **H**, and **D** at each cell location. The $\mathbf{E} \rightarrow \mathbf{H} \rightarrow \mathbf{D}$ loop is then repeated until the pulse has died off.

10.4.2 Human Bodies Exposed to EMFs

Computational algorithms based on numerical techniques described in the previous section have been applied to predict field intensities and SAR distributions in anatomically realistic models of human bodies. However, the use of a given numerical method and the number of computational cells involved in the models typically dictate the applicability of the techniques, how real the model is, the degree of accuracy attainable, and its domain of applicability. In the following sections, a few of the models will be described, and they will be followed by some representative results obtained using the models.

10.4.2.1 Realistic Models of the Human Body

Models proposed as better representations of the complex geometry and composition of the human body include constructions using small-volume cubic cells or cell meshes and anatomically based models generated from computerized tomographic and magnetic resonance image data.

10.4.2.1.1 Cubic-Cell Models

Models of the human body consisting of 200 to 1000 cubic cells that account more realistically for the gross anatomic and biometric characteristics of human bodies have been used by several investigators [24–28]. The models are 1.75 m tall and can be made either homogenous or inhomogenous by choosing an equivalent or a volume-weighted complex permittivity for each cell. The cubic-cell model has been employed successfully to calculate whole-body averaged absorption. It is important to note that for subdivision with less than three cells per wavelength, the magnitude and phase resolutions would be such that even with convergence the reliability of the MoM-computed SAR would be questionable. Therefore, if the interest is primarily in whole-body SAR, this model may provide quite adequate results for frequencies lower than 30 MHz. To achieve more accurate structural representation of the human body, anatomically based models have been offered in recent years.

10.4.2.1.2 Millimeter-Resolution Model Based on Magnetic Resonance Imaging Scans of the Human Body

A new millimeter-resolution model of the human body has been developed from the magnetic resonance imaging (MRI) scans of a male volunteer of 176.4-cm height and 64-kg weight [80,81]. The MRI scans were taken with a resolution of 3 mm along the height of the body and 1.875 mm for the orthogonal axes in the cross-sectional planes. Even though the height of the volunteer was quite appropriate for an average adult male, the weight was somewhat lower than an average of 71 kg, which is generally assumed for an average male. This problem can, to some extent, be ameliorated by assuming that the cell dimensions for the cross sections are larger than 1.875 mm by the ratio of $(71/64)^{1/2} = 1.053$. By taking the larger cell dimensions of $1.053 \times 1.875 = 1.974$ mm for the cross-sectional axes, the volume of the model can be increased by $(1.053)^2 = 1.109$, that is, by about 10.9%, which results in an increase of its weight by approximately the same percentage, that is, to a new weight of approximately 71 kg. The MRI sections were converted into images involving 29 tissue types whose electrical properties can then be prescribed at the exposure frequency. The tissue types are fat, muscle, bone, cartilage, skin, brain, nerve, cerebrospinal fluid (CSF), intestine, spleen, pancreas, heart, blood, eye, eye humor, eye sclera, eye lens, ear, liver, kidney, lung, bladder, stomach, ligament, compact bone, testicle, spermatic cord, prostate gland, and erectile tissue. As described above, this

model has been used to calculate the electromagnetic absorption in the human head, neck, and shoulders for cellular telephones operating at frequencies of 800 to 900 MHz. Because of the localized nature of EMFs, it was possible to use the model corresponding to the top 42 cm of the body for SAR calculations.

10.4.2.1.3 The ''Visible Human'' Model

The Visible Human (VH) Project, developed by the National Library of Medicine, is a 3-D digital image library representing an adult human male and female [82]. The dataset for both male and female includes photographic images obtained through cryosectioning of human cadavers and digital images obtained by computer tomography and MRI of the same cadavers. In particular, the photographic images represent a highly accurate and realistic counterpart of the anatomical cross sections contained in human anatomy atlases. The male dataset, the first to be constructed, consists of 1871 digital axial images obtained at 1.0-mm intervals, with a pixel resolution of 1 mm, while the female one contains 5189 digital axial images, obtained with a finer spatial step of 0.33 mm. While these digital datasets represent a unique tool to explore human anatomy, their direct use for computational electromagnetic dosimetry is limited by the fact that images cannot be directly used as an input for a numerical electromagnetic tool but must be converted to a so-called ''segmented'' version. A segmented model is a model where every pixel, usually called in such models ''voxel,'' does not contain information about the color (like in digital images) but rather a label that is uniquely associated to a given tissue. In such a way, it is possible to know which tissue fills each of the model voxels and hence assign the correct complex permittivity values to be used in numerical simulations.

Segmentation of the original image sets is a complex and time-consuming activity, which is difficult to carry out making exclusive use of automatic procedures, such as contour recognition algorithms, but inevitably requires intervention by experts in human anatomy. The segmentation procedure has been carried out for the male model by researchers at the Air Force Research Laboratory, Brooks Air Force Base, TX [83]. The final segmented model, made freely available to the scientific community, comprises $586 \times 340 \times 1878$ voxels with a resolution of $1 \times 1 \times 1$ mm, and is segmented in about 40 different tissue types [84]. The model has been widely used to study both whole-body and localized human exposure to EMFs radiated by different types of sources and is now being included in many commercially available electromagnetic simulation tools with capabilities for dosimetric evaluation.

10.4.2.2 Currents Induced in the Human Body by Low-Frequency EMFs

This section reports the results obtained for low-frequency EMF. Specifically, it includes the use of the impedance method to calculate currents induced in the human body by the EMFs of electric blankets. It also includes the use of the FDTD method for calculations of internal **E** and **H** fields and induced current densities for exposure to electric, magnetic, or combined electric and magnetic fields at power-line frequencies. The results given below were obtained using a 1.31-cm resolution, anatomically based model of the human body. Since the term $j\omega\varepsilon$ can be neglected as compared to σ for the various tissues at ELF including electric power frequencies (50/60 Hz), the impedances for the various cells of the model given by Equation 10.9 can be replaced by resistances. It is recognized that the conductivities of various tissues, for example, skeletal muscle, heart, and bone, are anisotropic for power-line frequencies [34,35,85]. This has been neglected in this case, however, and average values of conductivities given in Table 10.3 have been taken for the various tissues for the calculations.

TABLE 10.3

Tissue Conductivities Used for Calculations at the Power-Line Frequency of 60 Hz

Tissue Type	σ (S/m)
Air	0
Muscle	0.52 or 0.11
Fat, bone	0.04
Blood	0.6
Intestine	0.11
Cartilage	0.04
Liver	0.13
Kidney	0.16
Pancreas	0.11
Spleen	0.18
Lung[a]	0.04
Heart	0.11
Nerve, brain	0.12
Skin	0.11
Eye	0.11

[a]The dielectric properties of the lung consist of 33% lung tissue and 67% air.

10.4.2.2.1 Electric Blankets

To illustrate the use of the impedance method, currents induced in the human body by the EMFs of two types of electric blankets have been calculated [1,2]. The two models used for the blanket are (a) a low-magnetic-field blanket and (b) a conventional (pre-1990) electric blanket. The low-magnetic-field blanket uses two parallel leads carrying equal and opposite currents to reduce the net magnetic field around the conductors. The two leads are separated typically by 1.5 mm and are embedded in a positive temperature coefficient (PTC) conductive polymer and insulated by polyvinyl chloride (PVC). The PTC conductive polymer surrounding the two leads may be represented by a set of distributed resistors, which would result in linearly decreasing equal but opposite currents flowing through the two leads over the length of the wiring used for the blanket. By comparison, the conventional electric blanket uses a resistive alloy wire wrapped on a nylon cord and insulated with PVC. Because of the distributed resistance of the wire, this blanket would therefore have a linearly diminishing voltage and identical magnitude of current over the length of the wiring used for the blanket.

The validity of the calculated results has been established by comparing the results obtained using the impedance algorithm and those reported by others. The calculated fields are in excellent agreement with the data given by Florig et al. [86] and Hayashi et al. [87].

Currents are induced in the body by the following sources:

1. Time- and spatially varying magnetic fields of the blanket induced voltages in the various resistance loops of the body.
2. Currents launched into different subareas at the body surface by means of the capacitively coupled currents from the various conductors of the blanket.

The spatial variations of the magnetic fields were calculated from Biot-Savart's law for a short current-carrying conductor [2]. By integrating it over the entire length of the

current-carrying conductors, one can obtain the vector magnetic fields at the centers of the cells representing the model of the human body or any of the other points in space. From the vector magnetic fields thus calculated for each of the cell centers for the impedance model of the human body, the induced voltages for each of the faces of the cells can be written [32]. This information is then used to calculate the induced currents for the various impedances, that is, resistances. The average current densities J_x, J_y, and J_z for each of the cell centers can be obtained by taking the average of the currents through the resistances representing each of the four edges of the cell in the respective directions and dividing the same by the cross-sectional area δ^2 ($= 1.31 \times 1.31$ cm).

To calculate the electric field distribution in air, a 3-D impedance model consisting of capacitors representing the space between the various faces of the cells was used. For cubic cells of dimension $\delta = 1.31$ cm, the capacitances used are $\varepsilon_0 \delta^2/\delta = 0.116$ pF.

For currents induced in the human body due to electric fields, it should be recognized that the energized conductors of the blanket are capacitively coupled to the body. The capacitance between a given conductor and the highly conducting human body can be obtained by using an expression similar to that for a conductor at a distance S from the ground plane. Capacitance per unit length C of a wire of diameter d parallel to but separated at a distance S from the ground plane is given by

$$C = (2.73\varepsilon_{\text{eff}})/[\log_{10}(4S/d)], \quad \text{pF/m} \tag{10.18}$$

For a spacing $S = 5$ mm and a wire diameter $d = 0.8$ mm, and for $\varepsilon_{\text{eff}} = 2.5\varepsilon_0$, which is a value intermediate between the permittivity ε_0 for air and $4\varepsilon_0$ for the material of the blanket, we can calculate $C = 43.1$ pF/m. For a cell length $d = 1.31 \times 10^{-2}$ m, the coupling capacitance C_c between the wire and the cell can be calculated to be 0.565 pF. Since the interconductor spacing of 1.5 mm for a PTC blanket is fairly small as compared to the cell size, a proportionately smaller resistance is taken for the tissue-equivalent cells immediately underneath the conductors for the direction parallel to the interconductor spacing. Capacitances of 0.565 pF are taken from each of the conductors of the PTC blanket to the appropriate points on the impedance model of the human body. In the presence of an electrical grounding surface, the space underneath the model is represented by a 3-D network of capacitors, each of value 0.116 pF, representing the air space between the various faces of the cubic cells of dimension $d = 1.31$ cm for each of the sides.

For the PTC low-magnetic-field blanket, a constant voltage of 110 V AC is taken between the conductors of the twin-lead wiring for calculation of currents induced or injected into the human body as a result of electric fields. For calculating the magnetic fields, an input current of 1 A is taken. On account of the conductive polymer surrounding the parallel wires, this current diminishes linearly to zero at the end of the PTC wiring. This assumes a blanket input power of 110 W under normal operating conditions. If magnetic fields or induced current densities due to higher input powers are desired, the numbers calculated for 1 A input current may then be multiplied by the appropriate factor.

The conventional blanket, on the other hand, uses a resistive conductor for which the voltage diminishes linearly from 110 to 0 V over the length of the wiring. For this blanket the current throughout the length of the wiring is the same as at the input, that is, 1 A, which is assumed for the calculation of magnetic fields.

The magnetically induced, section-averaged magnitudes of the total current densities from head to feet for the two types of blankets are shown in Figure 10.13a and b, respectively. For these calculations, the wiring of the blanket was taken to be 0.5 cm from the surface of the body. Nearly identical current densities were also obtained for a grounding plate underneath the body at distances of 0.25, 0.5, and 1.0 m. It is interesting to

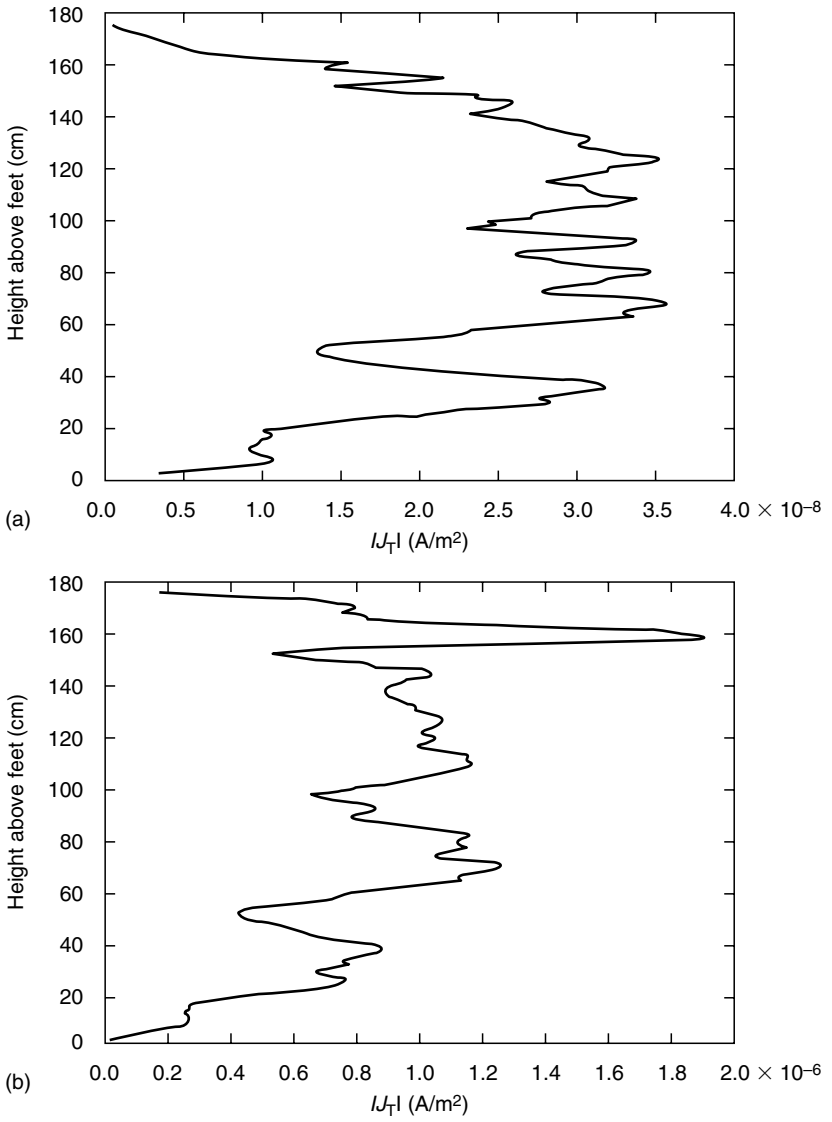

FIGURE 10.13
Section-averaged magnitudes of total current densities for the various sections of the body for magnetic fields of the blankets. Nearly identical current densities were obtained also for a grounding plate at distances of 0.25, 0.5, and 1.0 m underneath the body. Input current = 1 A.

note that the induced current densities are larger by a factor of about 500 for the conventional blanket vis-a-vis those for the low-magnetic-field blanket.

The calculated section-averaged magnitudes of the total current densities due to electric fields of both the blankets in the absence of a grounded plane are shown in Figure 10.14a and b, respectively. It should be noted that while the current densities induced by the electric fields of a low-magnetic-field blanket (Figure 10.14a) are considerably higher than those due to magnetic fields (Figure 10.25a), the converse is true for a conventional blanket. For this blanket, the current densities induced by the magnetic fields (Figure 10.13b) are higher than those due to electric fields (Figure 10.14b). In fact, while the current densities due to magnetic fields are fairly small for a low-magnetic-field blanket

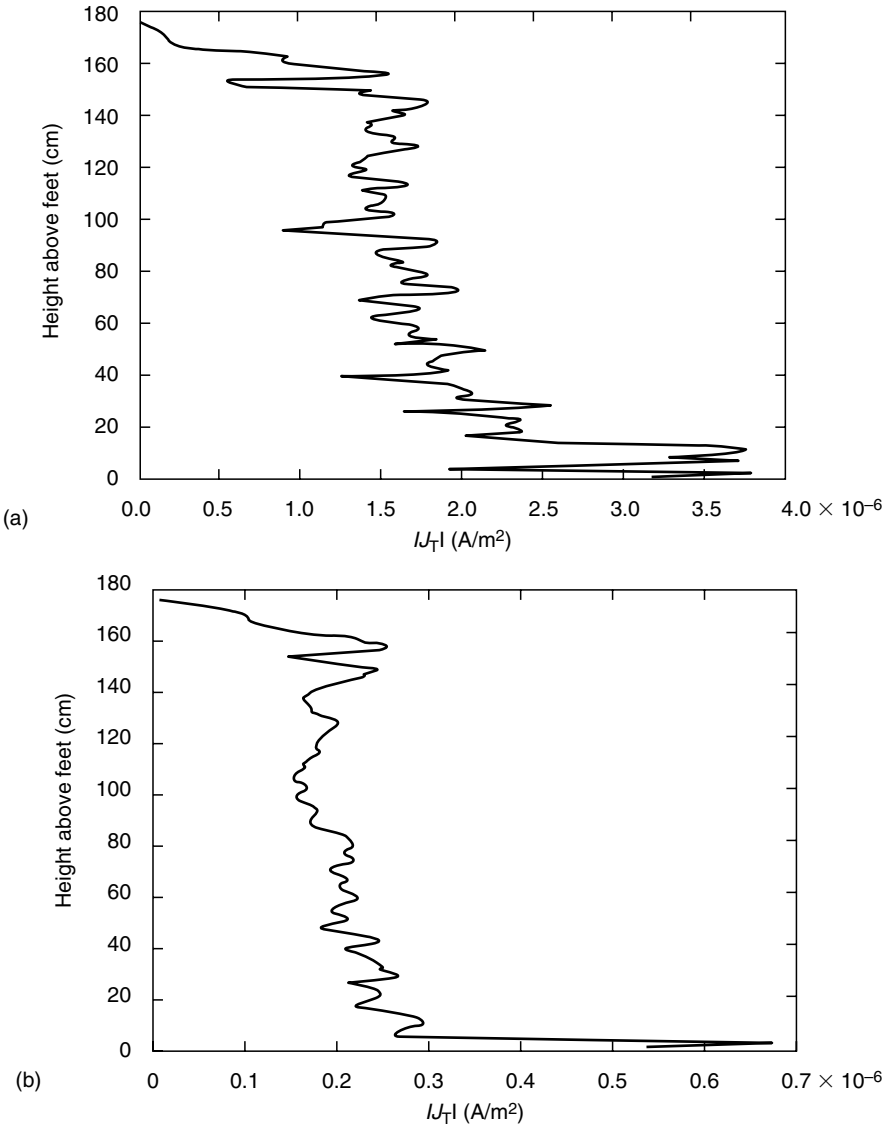

FIGURE 10.14
Section-averaged magnitudes of total current densities for the various sections of the body for electric fields of the blankets. No ground plane underneath the body.

as compared to those for a conventional blanket, the current densities due to electric fields of a low-magnetic-field blanket are even higher than those for a conventional blanket (see Figure 10.14a and b). The reasons for these observations can be seen from the values of magnetic and electric fields given in Table 10.4 for the two types of blankets, respectively. While fairly small magnetic fields are calculated for the low-magnetic-field blanket as compared to those for the conventional blanket, the converse is true for the electric fields created by these blankets. As seen in Table 10.5, somewhat higher electric fields are created by the low-magnetic-field blanket as compared to those for the conventional blanket. This is likely due to the higher potential difference between the twin-lead conductors that are used for the low-magnetic-field blankets.

TABLE 10.4

Comparison of the Calculated and Measured Magnetic Field (μT) and Electric Field (V/m) Close to a Flat Blanket [2]

	Grid Size (cm)	Calculated	Measured
Low-magnetic-field blanket[a]			
Magnetic field			
Average	1.31 × 1.31	0.056	—
	10.5 × 10.5	0.072	0.09
Peak	—	0.20	0.26
Electric field			
Average	1.31 × 1.31	103.7	—
	10.5 × 10.5	144.6	111.2
Peak	—	159.7	176.0
Conventional electric blanket[b]			
Magnetic field			
Average	1.31 × 1.31	2.16	—
	10.5 × 10.5	2.45	2.18
Peak	—	3.52	3.94
Electric field			
Average	1.31 × 1.31	57.3	—
	10.5 × 10.5	70.1	95.4
Peak	—	176.1	167.2

[a]For this blanket, the magnetic-field results are normalized for a blanket input current of 1.227 A, that is, a power input of 135 W.
[b]For this blanket, an input current of 1 A is assumed.

10.4.2.2.2 Power Transmission Lines

The FDTD method has been used for calculations of internal **E** and **H** fields and induced current densities for exposure to electric, magnetic, or combined electric and magnetic fields at power-line frequencies [37]. While recognizing that the conductivities of many biological tissues (skeletal muscle, bone, etc.) are highly anisotropic for power-line frequencies, however, the effect of anisotropy is neglected for the sake of simplicity. They could be included in more complex models by separately identifying these tissues.

Both sinusoidal and prescribed time-varying incident fields can be used with the FDTD procedure—hence the method is well suited also for transient exposures that are often of interest at power-line-related frequencies. For sinusoidally varying fields, the solution is completed when a sinusoidal steady-state behavior for **E** and **H** fields is observed for each of the cells. For lossy biological bodies this typically takes a time step on the order of three to four time periods of oscillation. Since Δt is fixed for a given cell size, a larger number of iterations are therefore needed at lower frequencies. Because of the large number of iterations, the FDTD procedure would be clearly inapplicable for calculations at power-line frequencies were it not for the quasi-static nature of the coupling at low-frequencies [16,88,89]. Thus, the field outside the body does not depend on the internal tissue properties, but it depends only on the shape of the body so long as the quasi-static approximation holds, that is, the size of the body is a factor of 10 or more smaller than the wavelength, and $| \sigma + j\omega\varepsilon | \gg \varepsilon_0$, where σ and ε are the conductivity and the permittivity of the tissues, respectively; $\omega = 2\pi f$ is the radian frequency; and ε_0 is the permittivity of the free space outside the body. Under these conditions, the electric fields in air are normal to the body surface, and the internal tissue electric fields can be obtained from the boundary conditions in terms of fields outside:

TABLE 10.5

Reported SAR Values, Averaged over the Whole Body (SAR_{WB}), for Plane Wave Exposures

	SAR (W/kg)					
Frequency (MHz)	Grounded Shoes [98]	Grounded [102]	Isolated [102]	Isolated (resolution 3 mm) [103]	Isolated (resolution 5 mm) [103]	Grounded [105]
10	0.027	0.045				
20	0.102	0.182	0.021			
30	0.180	0.313	0.054			
40	0.291	0.348	0.114			
50	0.230	0.293	0.199			
60	0.177	0.231	0.288			
70	0.152	0.188	0.302	0.270	0.290	
80	0.130	0.162	0.251			
90	0.107		0.195			
100	0.092	0.118	0.155			0.123[a]
200	0.062	0.081	0.080	0.048	0.051	0.078[b]
300	0.054					
400	0.060	0.063	0.063	0.064	0.060	
500	0.058					0.060
600	0.057		0.063	0.067	0.066	
700	0.059					
800	0.061			0.064	0.063	
900	0.061	0.062	0.064			
1000				0.063	0.061	0.057
1400			0.063			
1800		0.057	0.058	0.056	0.060	
2000				0.055	0.060	

[a]The frequency considered is 120 MHz.
[b]The frequency considered is 210 MHz.

$$j\omega\varepsilon_0 E_0 = (\sigma + j\omega\varepsilon)E_{\text{tissue}} \tag{10.19}$$

A higher quasi-static frequency f', at 5 to 20 MHz, may therefore be used for irradiation of the E model, and the internal fields E thus calculated may be scaled back to frequency f of interest, for example, 60 Hz. Since in the FDTD method, one needs to calculate in the time domain until convergence is obtained, this frequency scaling to 5 to 20 MHz for f reduces the required number of iterations by over five orders of magnitude. From Equation 10.19 we can write

$$\omega'(\sigma + j\omega\varepsilon)E_{\text{tissue}}(f) = \omega(\sigma' + j\omega\varepsilon')E'_{\text{tissue}}(f') \tag{10.20}$$

or

$$E_{\text{tissue}}(f) = (f\sigma'/f'\sigma)E'_{\text{tissue}}(f') \tag{10.21}$$

assuming that $\sigma + j\omega\varepsilon \sim \sigma'$ at both f' and f [2,90]. To validate the use of a higher frequency f to obtain induced E fields at ELF frequencies, test cases involving homogenous and layered spheres have been used. Excellent agreement between the numerical and analytical results lends support to the validity of the FDTD method for calculating internal E fields and current densities at power-line-related frequencies. It should be noted that incident E and H fields of any orientation and relative magnitudes can be prescribed in the FDTD method, allowing the possibility of calculations for realistic

exposure conditions. Also, the choice of a considerably higher frequency such as 5 to 20 MHz reduces the number of iterations needed to obtain converged results by five to six orders of magnitude as compared to those that would be needed at ELF frequencies of 10 Hz to 1 kHz.

Some calculated results using a 16-tissue, 1.31-cm resolution, anatomically based model of the human body are given in Figure 10.15. A frequency f' of 5 to 10 MHz was used to reduce the computation time. At the higher irradiation frequency f', $\sigma' = \sigma$ was assumed, that is, conductivities of the various tissues at 60 Hz. Furthermore, the incident **E** field, $\mathbf{E}_i(f') = 60\mathbf{E}_i(f)/f'$, was used to obtain $\mathbf{E}_{\text{tissue}}(f)$ at, say, $\mathbf{E}_i(f) = 10\,\text{kV/m}$. The incident magnetic field $\mathbf{H}_i(f')$ has similarly been taken to be considerably lower ($= 60\mathbf{H}_i(f)/f'$) to account for the fact that the induced current densities and internal electric fields are proportional to the frequency of the incident fields and would therefore be higher at the assumed frequency f'. Recognizing the anisotropy in the conductivity of skeletal muscles, two different values of muscle conductivities are taken for curves (1) and (2). For these curves a higher conductivity of 0.52 S/m is taken for the skeletal muscle, and an average value of 0.11 S/m is taken for the muscle in the interior of the body. For curves (3) and (4), however, a lower conductivity of 0.11 S/m is taken for all of the muscle, interior or skeletal. The results shown in Figure 10.15, curves (1), (3), and (4) are for $E_{\text{inc}} = 10\,\text{kV/m}$ (vertical) and $H_{\text{inc}} = 26.5\,\text{A/m}$ ($B_{\text{inc}} = 33.3\,\mu\text{T}$) from side to side of the model. To point out the preponderance of the induced currents due to incident electric field, $H_{\text{inc}} = 0$ is assumed for the calculations shown in curve (2). It is interesting to note that the layer currents due to *E*-field exposure alone are almost 98% to 99% of the currents calculated for the combined electric and magnetic fields. It is also interesting to note that the calculated foot currents of 155 to 160 μA are in excellent agreement with 165 μA that would be projected from the measurements of Deno [91] for the human body. The variations of the induced currents calculated along the height of the body have been checked against the results by DiPlacido et al. [92]. The agreement with the results of these two authors who had

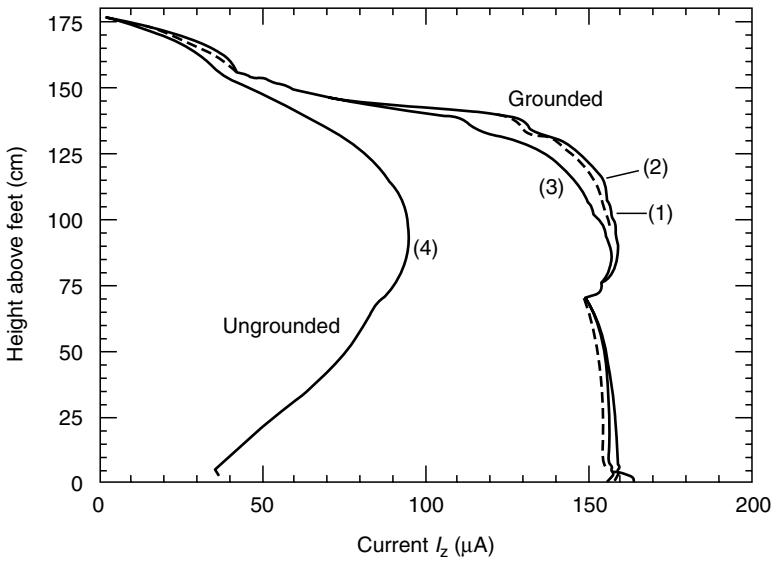

FIGURE 10.15
Calculated layer currents for anatomically based grounded and ungrounded models exposed to EMFs at 60 Hz. For curves (1) and (2), $s = 0.52\,\text{S/m}$ for skeletal muscle, and $s = 0.11\,\text{S/m}$ for the interior muscle. For curves (3) and (4), $s = 0.11\,\text{S/m}$ for all of the muscle. $E = 10\,\text{kV/m}$ (vertical), $H = 26.5\,\text{A/m}$ from side to side for all of the curves except for curve (2), for which only **E**-field exposure is assumed.

used a vertical electric field such as that under a high-voltage power line was found to be very good [37].

10.4.2.3 Absorption in Human Bodies Exposed to Far Field of RF Sources

As noted, the configuration and frequency of the electromagnetic source and the geometry and composition of the biological body will influence the induced field and power absorption and distribution inside the body. Moreover, the field emitted from a source is dictated by the frequency, size, and configuration of the source. Near an antenna, the radiated energy is in the form of a spherical wave in which the wave fronts are concentric shells. The spheroidal wave front expands as the wave propagates outward from the source. At distances far from the source, the radius of curvature of the spherical shells becomes so large that the wave front would essentially appear as a plane. They are therefore referred to as plane waves. Plane waves are important since their behavior is well quantified; the fields are uniform in planes normal to the direction of propagation, and the power density varies only in the direction of propagation. In this case, both electric and magnetic fields of the propagating wave are orthogonal in space and lie in the plane of the wave front, and are related through the intrinsic impedance of the medium. In other words, in the far or radiation zone, the electric and magnetic fields have only transverse components.

In this section, we shall briefly summarize some of the efforts devoted to field computation using various models of the human body, which consists of large quantities of numerical cells, and present some results obtained for plane wave exposures. Note that some, especially the simpler, models are of interest primarily for whole-body SAR and can provide quite adequate results for frequencies lower than 30 MHz. To achieve more accurate structural representation of the human body, anatomically based models are needed.

10.4.2.3.1 SAR Induced in Cubic-Cell Models

The VMoM for field computation has been used for models of the human body consisting of 200 to 1000 cubic cells. These models account for the gross anatomic and biometric characteristics of human bodies and have been used by several investigators [24–28]. The models are 1.75 m tall and can be made either homogenous or inhomogenous by choosing an equivalent or a volume-weighted complex permittivity for each cell. The cubic-cell model has been employed, successfully, to calculate whole-body averaged absorption. It is important to note that for subdivision with less than three cells per wavelength, the magnitude and phase resolutions would be such that even with convergence the reliability of the MoM computed SAR would be questionable.

According to the MoM, the body may be partitioned into N cubic subvolumes or cells that are sufficiently small for the electric field and dielectric permittivity to be constant within each cell. The integral equation is then transformed into a system of $3N$ simultaneous linear equations for the three orthogonal components of the electric field at the center of each cell. The simultaneous equations may be written in matrix form as

$$[G][E] = -[E^i] \tag{10.22}$$

where $[G]$ is a $3N \times 3N$ matrix and $[E^i]$ and $[E]$ are column matrices representing incident and induced electric fields at the center of each cell. The elements of $[G]$ can be evaluated as shown in Liversy and Chen [24]. In particular, the diagonal elements of the $[G]$ matrix may be evaluated exactly by approximating each subvolume with a sphere of equal volume centered at the position of an interior point. If the actual shape of the cell differs

appreciably from that of a sphere, this approximation may lead to unsatisfactory numerical results [36]. In such cases, a small cylindrical volume may be created around an interior point. It may also be necessary to evaluate these terms by numerical integration throughout the cubic subvolume for increased accuracy. The evaluation of off-diagonal elements of the [G] matrix is considerably simplified since it does not involve principal value operations. Therefore, for a given applied field configuration, the induced electric fields inside the body are obtained by matrix inversion. That is,

$$[E] - [G]^{-1}[E^i] \tag{10.23}$$

Factors that influence the computational accuracy include frequency, body size, cell dimensions, and computer memory. It has been found that reliable numerical results can be obtained if the linear dimensions of the cell do not exceed a quarter free-space wavelength [24]. For a computer with sufficient capacity to invert a 120 $\times$ 120 matrix, the maximum number of cells is limited to 40. If we assume, for simplicity, symmetries between the right and the left half and the front and the back of a 1.7-m-tall adult human body, this computer would handle approximately a cell size around 10^{-5} m^3. Once the 10^{-5}-m^3 cell size is adopted, 750 MHz would be the highest frequency that can be considered for field intensity calculation without violating the criterion that the linear dimension of the cell not exceed a quarter free-space wavelength.

The computational resources necessary to obtain even a regional SAR using this MoM approach are quite extensive. A relatively full complex matrix, $3N \times 3N$ in dimensions, is required for a model with N cells. The computation time required for a noniterative solution of the matrix equation is therefore proportional to a value between N^2 and N^3, which increases rapidly as N increases. The faithfulness with which a cubic-cell model approximates the detailed structure of a biological body and the maximum usable frequency increases with the number of cells. In fact, substantial errors will occur if

$$N \leq (2\pi L)/(\lambda' 6^{1/2}) \tag{10.24}$$

where L/λ' is the ratio between the linear dimension of the body and the wavelength in the body.

The accuracy of the numerical method can be verified by comparison with known results from exact analytic solutions based on well-characterized geometric bodies, such as spheres. It should be noted that perfect agreement between the exact solution, based on Mie theory, and the numerical method, based on the volume integral equation, is not expected unless a large number of cubic cells are used to simulate the sphere. Figure 10.16 shows one eighth of a sphere approximated by one eighth of a ''cubic model of a sphere,'' which is constructed from 73 cubic cells. Clearly, a better approximation can be achieved by a larger number of smaller cubic cells. Nevertheless, for a brain sphere constructed from 40 cubic cells at a frequency of 918 MHz, the computed maximum field intensity deviated from the exact solution by less than 9% [93].

A model of a human body consisting of 180 cubic cells that accounts for the anatomic and biometric characteristics of human beings is shown in Figure 10.17. The model is 1.75 m tall and can be made either homogenous or inhomogenous by using an equivalent or a volume-weighted complex permittivity for each cell [94]. The average absorption or whole-body SAR for the model of the human body shown in Figure 10.17 as a function of frequency is illustrated in Figure 10.18. The electric field vector is along the height of the body, and the plane wave propagates from front to back of the model with an incident power density of 10 W/m^2. A homogenous complex permittivity approximately two thirds of that for muscle is used in the calculations. Note that the whole-body SAR

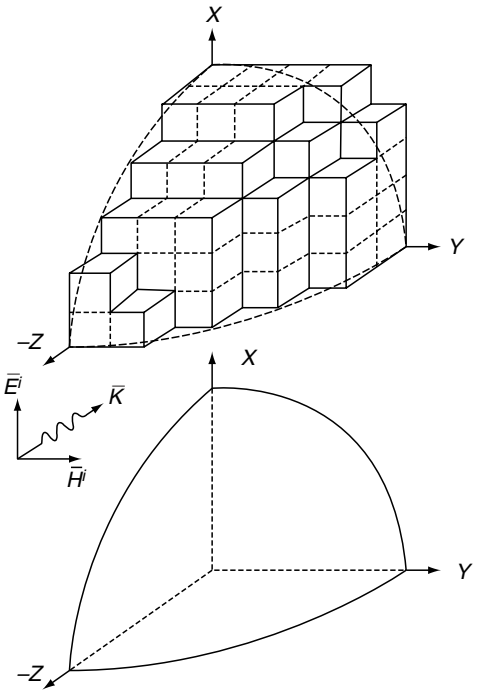

FIGURE 10.16
Approximation of one eighth of a sphere by an equivalent cubic-cell-formed structure.

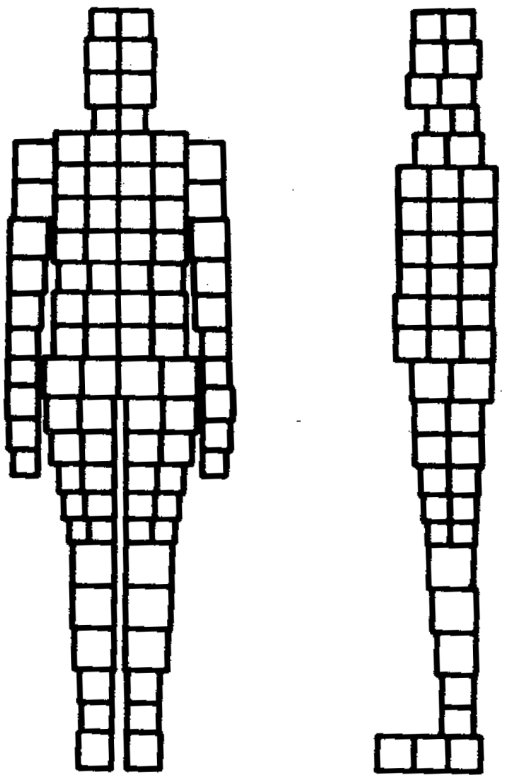

FIGURE 10.17
A cubic-cell representation of the human body.

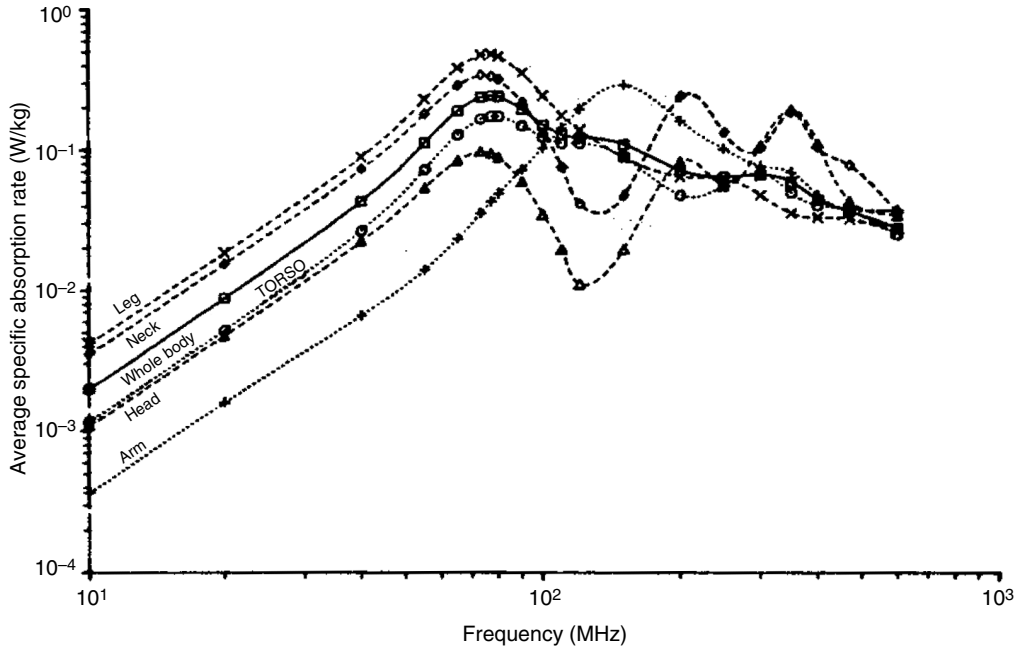

FIGURE 10.18
Average SARs for a homogenous 180-cell model of the human body exposed to a vertically polarized, 80-MHz plane wave. The incident power density is 10 W/m^2.

increases with frequency until it reaches a maximum of about 0.23 W/kg at 77 MHz (resonance frequency), and it then decreases as 1/frequency. The experimental data shown in Figure 10.19 are obtained from a saline-filled scale model of the human body. It can be seen that the calculated absorption is in good agreement with that found experimentally [27,95], except for the resonant frequency, which is somewhat lower (70 MHz) in the experimental case. It should be mentioned that whole-body SAR, given in Figure 10.18, is typically within 10% of that estimated from prolate spheroidal models of the same height and dielectric property. Further, when inhomogenous complex permittivities are used with the model, the whole-body SAR changes less than 2% from that depicted in Figure 10.18. Thus, if one is primarily concerned with average absorption over the body, a homogenous prolate spheroidal model may be quite adequate.

While the MoM based on the volume integral equation has been a useful numerical procedure for computation of average SAR and SAR distribution in complex tissue geometries, the requirement of a full $3N \times 3N$ matrix presents severe limitations. The computation times required to provide even regional SAR distribution of sufficient resolution to delineate the resonant frequency for the head region are enormous. A minimum of 340 cells was needed, increasing the computation time by a factor of 4 over the 180-cell models [95,96].

Matrix inversion operations consume the largest block of time in moment method solutions for the cubic-cell models. The computer time required is proportional to the cube of the number of cells. However, the matrix generated is usually diagonally dominant and well-conditioned. For a human-size body, iterative procedures for matrix inversion are practical at frequencies below about 60 MHz. The convergence rate decreases with increasing frequency and fails above 90 MHz. This is most likely caused by the decrease in the degree of diagonal dominance with increasing frequency. A number of approaches have been investigated to alleviate this difficulty. A semi-iterative procedure

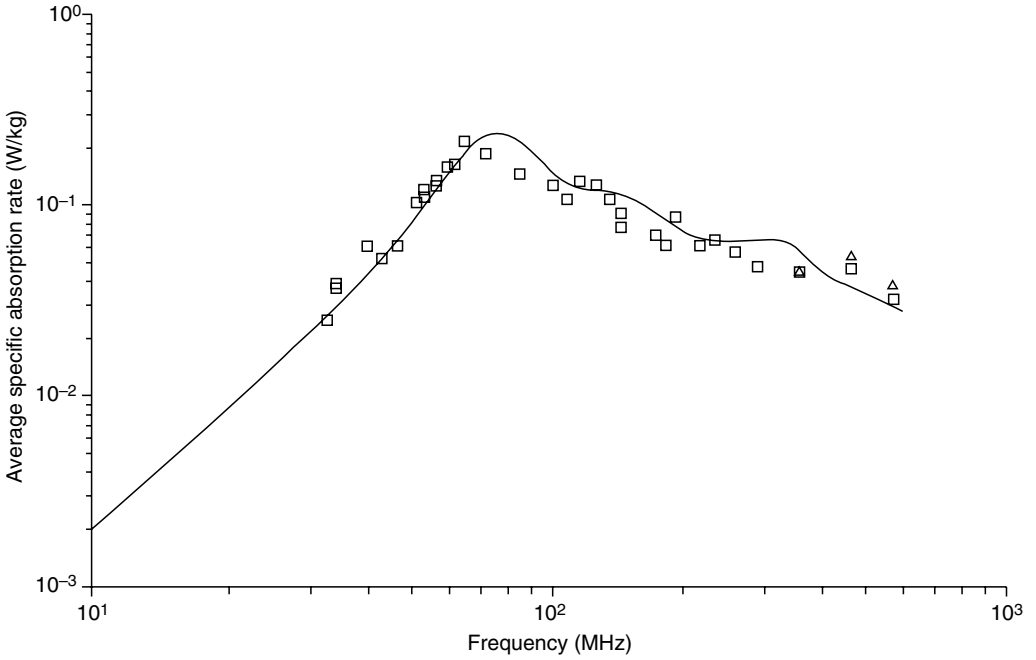

FIGURE 10.19
Whole-body averaged absorption for a homogenous cubic-cell model of humans exposed to vertically polarized plane in free space. The incident power density is 10 W/m^2.

called band approximation method appears to be an efficient algorithm that can be profitably used to invert large matrices generated by the number of cells for human models at arbitrarily high frequencies, and converges significantly faster than standard iterative algorithms [96].

10.4.2.3.2 SAR Induced in Fine Resolution Anatomical Models

To accurately evaluate the SAR induced in the human body, the FDTD method was introduced during the late 1980s, when the limitations of the MoM due to its memory requirements were reached. The capability of FDTD to take into account heterogeneities in models of the human body was first demonstrated using a model of the isolated human torso [69]. Later, a complete model of the human body was considered [97], and results for an isolated homogenous man model standing in free space were compared with results for an inhomogenous man model, under both isolated and grounded conditions [97]. The incident field was a plane wave propagating parallel to the ground plane and with the electric field vertically polarized (parallel to the long axis of the human body), at frequencies of 100 and 350 MHz. The human body model was obtained from cross-sectional diagrams and had a resolution of 2.62 cm at 100 MHz. The total occupied volume was $23 \times 12 \times 68$ cubic cells. At 350 MHz, the resolution was 1.31 cm for a total volume of $45 \times 24 \times 135$ cubic cells. The result, depicted as layer-averaged SAR or organ-averaged SAR, demonstrated the importance of considering inhomogenous models of the human body. For example, the homogenous model was not able to predict the peak SAR obtained in the eyes at 350 MHz, or the difference in absorption among the different organs.

Since these first works on power absorption, several papers have been published using anatomical models of the human body with finer resolutions.

The VH body model has been used to evaluate power absorption and temperature increase as a function of frequency of the incident plane wave, by considering a grounded male, either barefoot or with shoes [98]. The model had a resolution of 5 mm, a total height of 180 cm, and weight of about 103 kg. The large mass was due to the use of the VH model, which is far from the so-called ''reference man,'' as defined by International Commission on Radiological Protection (ICRP). The reference man weighs 73 kg and has a height of 176 cm [99]. In the referenced paper [98], for the frequency range between 10 and 900 MHz, SARs averaged over the whole body (SAR_{WB}) and locally, that is, averaged over 1.0 g (SAR_{1g}) and 10 g (SAR_{10g}), were evaluated. In particular, it has been found [98] that when the incident power density is equal to the reference levels set in the exposure standards, the basic restrictions on SAR_{WB} and on local SARs are never exceeded. Moreover, it has been shown [98] that the ratio, SAR_{10g}/SAR_{WB} was about the same (either 25 or 50 according to the body part considered) as the value used in the safety guidelines to convert basic restrictions on SAR_{WB} to basic restriction on local peak SAR [100]. On the other hand, the SAR_{1g}/SAR_{WB} ratio was found to be always higher than the value of 20 adopted in the safety guideline [101].

Figure 10.20 gives the SAR_{WB} as a function of frequency in a grounded male for an incident plane wave with a power density of 10 W/m^2 for two different human body models [98,102]. The SARs are slightly different because the two body models were different in height, weight, and tissue composition. The influence of the human body model on electromagnetic power absorption is further illustrated in Figure 10.21, where a comparison among the SAR_{WB} values obtained with the heterogenous VH model and a homogenous VH model consisting either of muscle or fat is reported. The frequencies considered are from 10 to 200 MHz to highlight the differences in power absorption at resonance.

It can be seen from the figures that a higher peak appeared at resonance in the homogenous muscle model, and lower absorptions were obtained in the homogenous fat model. Moreover, data from a lighter model (65.8 kg) obtained by reducing the cell dimension on the horizontal plane suggested that the lighter body absorbed more elec-

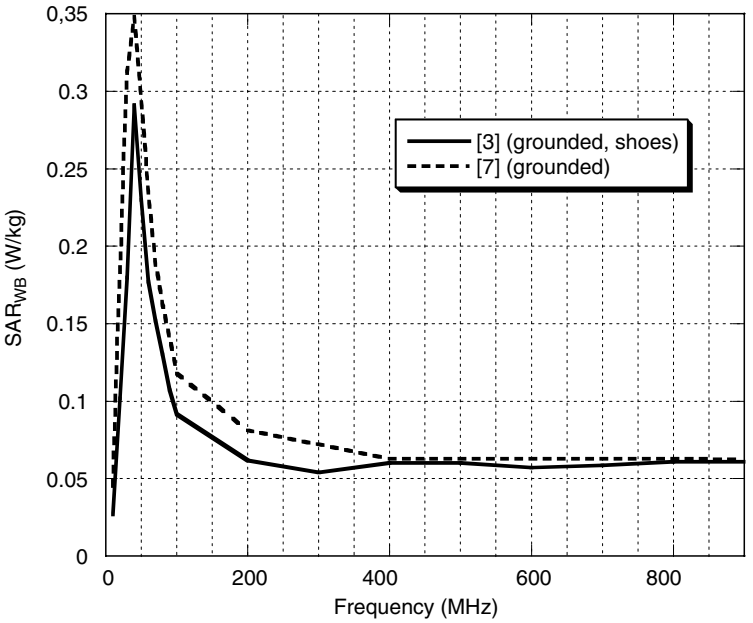

FIGURE 10.20
SAR as averaged over the whole body as a function of the frequency.

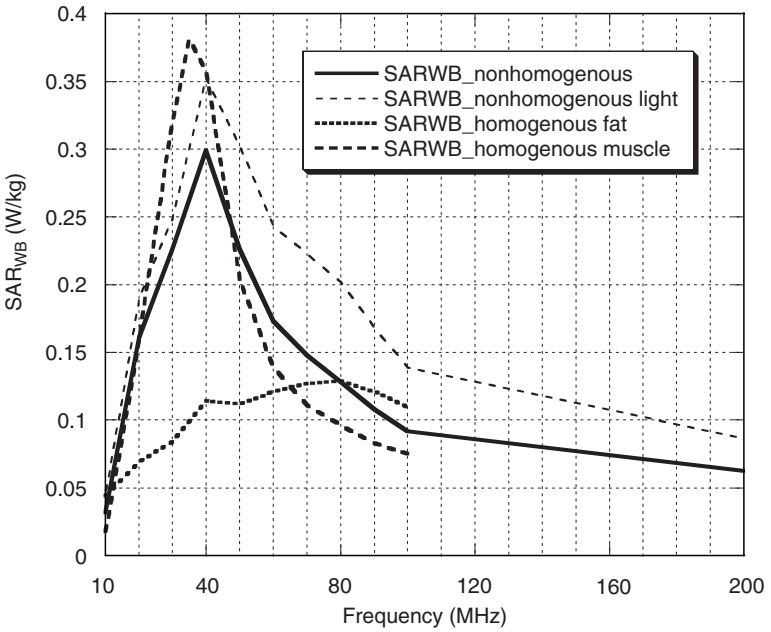

FIGURE 10.21
SAR as averaged over the whole body as a function of the frequency for different VH body models: nonhomogenous, nonhomogenous with a lighter weight (65.8 vs. 103 kg), homogenous fat, and homogenous muscle.

tromagnetic power than the heavier one. The frequency dependence of power absorption is clearly evidenced by Figure 10.20 and Figure 10.21. Indeed, this frequency dependence was the basis of the different limits imposed on the reference levels for different frequencies in the safety guidelines [100,101].

In Table 10.5 some literature data are summarized for the SAR_{WB} as a function of frequency (10 MHz to 2 GHz) for a grounded and isolated man model exposed to an incident power density of 1.0 mW/cm^2.

The first two columns refer to data in Figure 10.20, while the successive columns report data from published literature. Note the resonant frequencies of 40 vs. 70 MHz for grounded or isolated bodies. Moreover, the data in Table 10.5 show nonsignificant differences in SAR averaged over the whole body by changing the model resolution from 3 to 5 mm [103]. For the same reason the cubic-cell model described in the previous section had been employed, successfully, to calculate whole-body averaged absorption. The SAR_{WB} has a weak dependence on model resolution.

Likewise, a study on the SAR dependence on permittivity values [104] showed that uncertainty in permittivity values does not substantially affect the SAR as averaged over the whole body, while the same uncertainties have a greater effect on local SAR. In particular, considerations of different frequencies and orientations of the incident plane wave, or higher or lower permittivity values, showed that the maximum difference in SAR_{WB} was within $\pm 20\%$ [103]. Larger differences were found in local SAR, particularly when the permittivity of muscle, representing about 42% of the whole-body mass, was changed [103].

The data in the last column of Table 10.5 were obtained from a human body model [105] that was developed by using a new, semiautomatic procedure to construct numerically a frequency-dependent, dielectric anatomy model, starting from MRI images. The main difference between this human body model and the models usually considered in FDTD calculations is that in this model permittivity and conductivity can vary, even for the

same tissue, thus reflecting the realistic spatial inhomogeneity of such parameters. The semiautomatic procedure requires a short time to construct the model; thus, it could be used for dosimetry studies based on the model of specific persons.

A high-resolution human body model ($1.974 \times 1.974 \times 3.0$ mm) and a coarser one ($5.922 \times 5.922 \times 6.0$ mm), both for isolated and grounded conditions, were employed to determine the power absorption in the head and neck region and to evaluate the frequencies at which the absorption may be maximized [106]. It was observed that under isolated conditions two resonant frequencies occurred for the head and neck, one associated with the whole-body resonance and the other with a local resonance of the head and neck. Under grounded conditions, three resonances were observed; the additional resonance was attributed to a torso resonance.

Some studies were conducted to evaluate power absorption in models of women and children. Specifically, a 10-year-old child and a 5-year-old child were considered by scaling the adult human body model [106]. It should be noted that simply scaling the adult human body model to the children's dimensions does not produce an accurate model since the different organs scale differently; however, the general features in terms of height and weight are fulfilled, thus allowing for the determination of general properties of electromagnetic power absorption. In this way, resonant frequencies of 104 MHz for the isolated model and 65 MHz for the grounded 10-year-old child were obtained, while for the 5-year-old model, they were 126 and 73 MHz, respectively.

In a different study, power absorption in scaled versions of the adult human body model representing 10-, 5-, and 1-year-old children was evaluated for both grounded and isolated conditions [102]. Figure 10.22 gives the SAR_{WB} obtained for the three child models under isolated conditions and an incident power density of $1\,mW/cm^2$. A shift in the resonant frequency with the height of the model—the taller the model, the lower

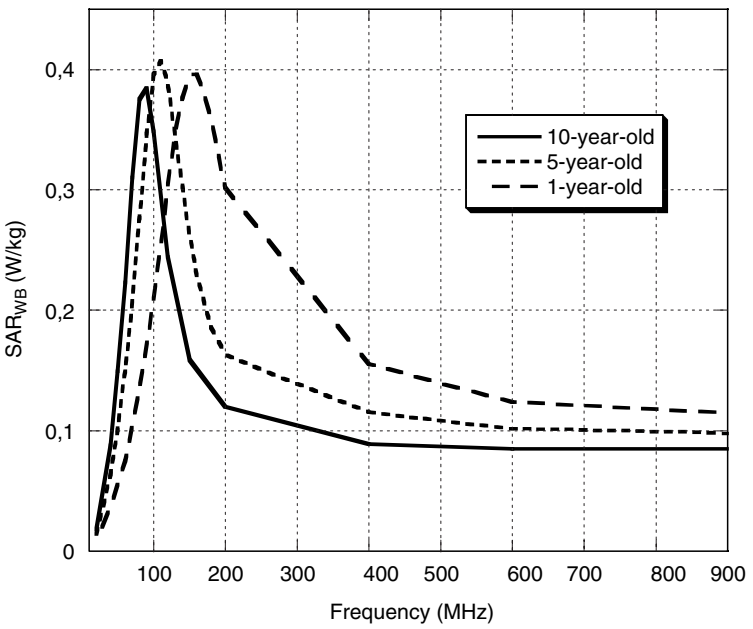

FIGURE 10.22
SAR as averaged over the whole body as a function of the frequency for different child body models: 10, 5, and 1 year old. Incident power: $1\,mW/cm^2$. (Data from Dimbylow, P.J., *Phys. Med. Biol.*, 47, 2835, 2002.)

the resonance frequency—can be observed from the figure; note also the higher absorption in the smaller child body model [102].

The potential differences between SAR induced in man and woman have been explored using slightly different models [107,108]. In one study, 2-mm resolution models were developed for evaluating power absorption in Japanese males and females. Note that the use of the 2-mm resolution body models had led to an overestimation of the skin weight by 50% or more than the average value for the Japanese reference body [107]. The computed results showed that the difference in SAR_{WB} between male and female models was small, within 1.1 dB. The authors concluded that gender does not affect SAR_{WB}. Similarly, they obtained no significant differences between the male and female models with regard to local SARs. However, the overestimation of skin weight, and perhaps other tissues, in the 2-mm resolution body models could have influenced their results and conclusions.

In contrast, a clear difference in power absorption was reported [108] between Caucasian male and female models. The two Caucasian body models were developed using the semiautomated procedure previously cited [105]. In particular, considerably greater SAR_{WB} was obtained in the female model than in the male one (about 40% higher in the frequency range between 500 MHz and 2.0 GHz and 25% higher in the frequency range between 2.0 and 4.0 GHz). The difference in local SARs (both SAR_{1g} and SAR_{10g}) were insignificant between genders for up to 3.0 GHz, while above this frequency, say up to 4 GHz, the SAR_{1g} and SAR_{10g} in the female model became larger than those in the male model. The authors observed that this result could be explained by the difference in subcutaneous fat between man and woman. It was noted that a better identification and modeling of the skin layer could influence the results. Clearly, further studies are needed to assess the similarities and differences in power absorption between male and female body models exposed to EMFs of radiating sources.

In summary, available data on electromagnetic power absorption in human body models exposed to plane wave fields show that the choice of the human body model affects the results obtained. The observed differences among the published data are usually more pronounced in local SARs than in SARs averaged over the whole body. The body height, mass, tissue distribution and composition, including fat and muscle, are important factors in power absorption and can explain some differences among the published data. Another fundamental aspect is the value assigned to the dielectric properties of different tissues or organs identified in the body model. In the case of children, the variation in tissue dielectric properties with age also may influence the computed results. It is noteworthy that the above publications have used dielectric properties from the same sources [109,110].

10.4.2.4 Human Exposure to the Field Radiated by Transceiver Base-Station Antennas

The enormous growth in the number of subscribers of mobile telecommunication systems during the past few years has pushed upward the system's capacity. As a result, more and more base stations have been installed on the rooftop of existing buildings in densely populated areas, and many more are expected to be set up as the next-generation mobile networks (UMTS, IMT2000, etc.) are deployed. These installations are giving rise to widespread concerns among the population about possible deleterious effects on human health from exposure to the EMFs radiated by the base-station antennas. Recently, increasing attention has been paid to the topic of numerical exposure and compliance assessment for base-station installations.

A great deal of work has been done in the area of field intensity prediction in the vicinity of base-station antennas to determine the so-called free-space compliance boundary. The studies were aimed toward a direct comparison with reference levels suggested

by international exposure guidelines [100,101]. They generally have neglected both the influence of the environment in which the antennas operate and the dosimetric problem of SAR evaluation inside an exposed subject. In particular, considerable efforts have been spent on determining simplified and efficient analytical [111,112] and numerical [113,114] models to evaluate field levels near base-station antennas. Starting from the theory of collinear dipole arrays, typically employed in base transceiver station (BTS) antennas, practical analytical formulas have been derived to predict average power density falloff as a function of distance from the antenna. The space surrounding the antenna is often divided into a cylindrical-wave region, closest to the antenna, and a spherical-wave region, further away [111]. A complementary formulation also has been proposed, on the basis of an exact asymptotic solution for the radiated field, to derive approximate analytical formulas that allow a conservative prediction of equivalent peak power density as a function of the distance from the antenna [112].

Besides the aforementioned practical analytical formulations, simplified numerical models are often used, by subdividing the antenna into elementary radiators [113,114]. Under the hypothesis of weak coupling between the subelements, the near field can be quickly computed through a superposition of the fields independently radiated by the different elements. Once the radiation pattern of the subelements is known, the field is derived using the antenna gain-based formula [113,114]. For better accuracies in the vicinity of the antenna, an MoM simulation of the subelement can be invoked [114]. These simplified approaches represent extremely fast tools for field intensity prediction, but they are limited by a minimum distance from the antenna where they can be applied in order to maintain an acceptable computational accuracy. On the other hand, when field computations within a distance of a few wavelengths from the antenna have to be done, full-wave numerical techniques, such as FDTD, must be adopted. The accuracy of FDTD models for evaluating the near field of base-station antennas has been investigated and validated through a comparison with measurements carried out in a fully anechoic chamber [115].

Full-wave approaches require knowledge of the internal structure of the antenna, which is not always available. Cylindrical- and spherical-wave expansion techniques have been proposed to evaluate the near field, starting from measurements performed on a surface enclosing the antenna [116–118]. The basic approach consists of performing field measurements on a spherical surface surrounding the antenna and describing the measured field as a superposition of spherical modes [115]. Once the spherical-wave expansion coefficients have been determined, the near field can be extrapolated for all points lying outside the minimum sphere enclosing the antenna. This technique also has been improved to allow extrapolation of the field inside the minimum sphere [117]. To this end, the spherical-wave expansion coefficients are derived for each of the antenna subelements. This approach extends the range of applicability of the formulation to all points outside the minimum sphere of a single subelement, which is much closer to the antenna than the minimum sphere of the overall array. Recently, an alternative solution to extend field extrapolation close to the antenna was proposed, which consists of spherical-wave expansion outside the minimum sphere of the antenna and cylindrical-wave expansion for the region close to the antenna, with an appropriate matching of the two expansions [118].

The effect of the surrounding environment must be taken into account to some extent in dealing with the problem of evaluating induced SAR in a subject exposed to the field radiated by BTS antennas, since the antenna is not operating in a free-space condition. A very interesting approach, applicable to on-site evaluations, consists of using mixed experimental and numerical procedures [119–121]. One procedure is based on on-site measurement of the amplitude and phase of the exposure field distribution over a surface

surrounding the antenna. The measurement is then used to numerically evaluate induced SAR distributions inside a phantom. The measured fields are used to excite the FDTD domain via the equivalence principle [119]. A much faster and efficient procedure uses previously stored FDTD-computed **E**-field distributions inside a phantom exposed to spatially impulsive electric fields, the equivalent spatial impulsive responses of the phantom or Green's functions. The on-site measurement of amplitude and phase of the exposure field is made over an equally spaced grid of points placed on an appropriately chosen surface [120]. The procedure has recently been enhanced and made faster by substituting the spatial impulse response with responses to spatial harmonic components [121]. In this way, good accuracy is achieved using only six to ten spatial harmonic components, as opposed to the 54 spatial impulse responses needed previously.

The aforementioned hybrid experimental–numerical procedures have the great advantage of allowing easy characterization of environmental perturbations to the exposure field by directly including them in the measured field. On the other hand, they require the antenna to be already installed and operating at the time of measurement. The last point makes such procedures not suitable for *a priori* compliance assessment evaluations during the planning stage of a cellular network. For such evaluations, a thorough numerical dosimetric analysis is required. Once again, a possible approach, when the environment can be neglected and the antenna can be supposed to operate under free-space conditions, consists of performing full-wave FDTD simulations and modeling both the BTS antenna and a numerical phantom of the exposed subject. The applicability of such an approach has also been demonstrated, through a comparison with SAR measurements, for exposure locations in close proximity to the antenna [122]. The main drawback of full-wave FDTD analysis is the large amount of memory required to discretize the simulation space for phantom locations not in the close proximity of the antenna. This problem can be faced by exploiting parallel computer architectures with parallelized versions of the FDTD code [123]. Parallel FDTD also has the potential to allow SAR computations for large antenna–phantom distances.

More efficient techniques have been developed that combine two different techniques, one to model BTS antenna and propagation in free space and the other, SAR inside the phantom [124,125]. In particular, if the antenna–phantom distance is such that mutual coupling can be neglected, a hybrid ray-tracing (RT)–FDTD approach can be used [124]. RT is used to model field propagation from the BTS antenna to an equivalent surface surrounding the phantom, and FDTD is employed to study absorption inside the phantom, using RT-derived exposure fields for excitation. For closer antenna–phantom distances, where the mutual coupling cannot be neglected, a hybrid FEM–MoM technique has been proposed [125]. In this case, MoM is used to model the BTS antenna, while FEM is used to study absorption inside the phantom. The MoM and FEM formulations are coupled together and are solved iteratively. These hybrid approaches allow very efficient SAR computation for different antenna–phantom distances and are well suited for evaluating free-space compliance distances, on the basis of SAR restrictions. They do not require the use of derived exposure field reference levels. For example, the RT–FDTD technique has been applied to a common 14-dBi-gain GSM900 antenna using the VH phantom. It was shown that for a total radiated power of 30 W, typical for urban area installations, SAR basic restrictions for the general population may be exceeded at distances of 2 m or less. Note that, at these distances, only occupational personnel are allowed [124].

The RT–FDTD hybrid technique also has been successfully employed to study human exposure to the field radiated by a BTS antenna in an urban scenario, including the effect of environmental perturbations to the exposure field [126]. In this case, image sources have been introduced to represent corner-reflector-like urban scenarios. Three different exposure conditions have been considered for a rooftop-mounted 14-dBi-gain BTS

TABLE 10.6

Spatial Maximum (E_{iMAX}) and Spatial Average (E_{iAVE}) of the Incident Field (rms Value); Maximum SAR Values Averaged over 1 g (SAR_{1g}) and over 10 g (SAR_{10g}), and SAR Value Averaged over the Whole Body (SAR_{WB}) for Three Exposure Conditions

	E_{iMAX} (V/m)	E_{iAVE} (V/m)	SAR_{1g} (mW/kg)	SAR_{10g} (mW/kg)	SAR_{WB} (mW/kg)
Rooftop	4.2	2.8	5.3	3.0	0.12
Balcony	8.1	5.5	13.2	8.5	0.46
Street	1.3	1.1	0.26	0.17	0.01

antenna, radiating 30 W in the GSM900 frequency band: (1) a subject standing on the rooftop, near the antenna mast; (2) a subject standing on a balcony of a building facing the antenna at a distance of 30 m, within the antenna main beam; and (3) a subject standing in the street below the 30-m tall building on which the BTS antenna was mounted. The computed results for the incident electric field and SARs, under these exposure conditions, are given in Table 10.6.

From Table 10.6, because of the high directivity over the vertical plane of base-station antennas, it appears that the highest field levels are not obtained on the rooftop of the building where the antenna is located. Instead, they are on the nearby building, in the direction of the maximum antenna radiation. As expected, the lowest field levels are experienced by a subject standing in the street, as a result of the large distance from the antenna and the off-axis position with respect to the antenna pointing direction. In all cases, the computed SARs are at least two orders of magnitude lower than the basic restrictions, confirming the expected low exposure levels for people living near a BTS installation in urban areas.

More recently, some hybrid techniques have been developed, with enhanced capabilities in modeling complex urban environments, by taking into account diffraction phenomena [127–129]. One such technique uses FEM to model the BTS antenna, the uniform theory of diffraction (UTD) to model the effects of the environment on field propagation, and FDTD to study power absorption in the exposed subject [127]. The technique has been employed to study exposure of a subject standing inside a room with a microcell BTS antenna mounted on the external wall. Another possible hybrid solution exploits time domain physical optics, instead of UTD, to model field scattering from the environment and FDTD to study absorption inside the exposed subject [128].

Finally, a hybrid UTD–FDTD technique has been developed to highlight some key points related to compliance assessment procedures for cellular base-station antennas, in a realistic urban environment [129]. The scenario analyzed consists of a room in one building where the field, radiated by a GSM900 or a UMTS BTS antenna installed on a facing building, penetrates through the room's external wall and window. The relation between SAR in an exposed subject and ambient field in the absence of the subject has been investigated for the complex scenario. As expected, the ambient field showed a highly nonuniform distribution resulting from the many reflections and diffractions that took place. The results showed that whole-body averaged SARs (SAR_{WB}) are closely correlated with the exposure field value averaged over the volume that would be occupied by the exposed subject. In particular, it has been estimated that assessing SAR_{WB} on the basis of volume-averaged field values yields an average error of approximately 6%. Peak 1-g and 10-g averaged SARs, instead, show a rather complex and difficult-to-predict relation with reference to the exposure field. Analysis of the results has revealed that the use of the volume-averaged exposure field value, in the absence of the subject, can lead to

an underestimation of the peak local SARs, up to 36%. On the contrary, using the maximum volumetric value yields an overestimation of peak local SAR (up to approximately four times). The conclusion was that peak local SAR showed a good correlation (15% average error) with the maximum average exposure field value obtained by varying the position of a vertical averaging plane, having a surface equivalent to the projected human body area, inside the volume occupied by the subject.

10.4.2.4.1 *Human Exposure to the Fields Produced by Coexisting Wireless Communication Systems*

The discussions thus far have dealt with the problem of human exposure to fields radiated by a single base-station antenna from the cellular mobile communication systems (i.e., GSM, UMTS, etc.). However, as the development of communication systems making use of wireless technology expands, new exposure scenarios are encountered in everyday life. Following the enormous growth in the number of base stations in densely populated areas, one of the most promising systems in the near future may be the so-called Wi-Fi system, namely, wireless LAN adopting the IEEE 802.11b communication standard. Wi-Fi is characterized by completely different coverage ranges. Unlike base-station antennas of cellular systems, which are installed almost entirely in outdoor locations, access points (APs) of Wi-Fi systems would operate essentially inside buildings. Nonetheless, the EMFs radiated by the two systems will coexist in indoor environments, particularly if buildings located in front of a rooftop-mounted base-station antenna are considered. This poses new questions about human exposure in such environments. It becomes important to assess typical exposure levels attributable to each system.

The problem has been recently addressed by considering exposure of a subject standing inside a room with a Wi-Fi AP and facing a dual-band GSM900/GSM1800 BTS antenna mounted on the rooftop of a nearby building [130]. The AP radiates a power of 100 mW at 2.44 GHz, while the GSM BTS employs an antenna with a 18-dBi gain, radiating a total power of 30 and 20 W in the GSM900 and GSM1800 frequency bands, respectively. The computed results for exposure field values and SAR levels are summarized in Table 10.7 and Table 10.8. Specifically, the first two columns of Table 10.7 show the peak ($E_{\text{vol peak}}$) and average ($E_{\text{vol ave}}$) root mean square (rms) exposure field values over the entire parallelepiped volume where the subject will be placed, while the third column reports the average ($E_{\text{sup ave}}$) rms exposure field values over vertical sections of the parallelepiped volume. In particular, the minimum and maximum field values are given because the averages depend on where exactly the surface is placed. Table 10.8 presents whole-body, peak 1-g and 10-g averaged SARs inside the exposed subject.

It can be seen from Table 10.7 that the highest contribution to the total field level inside the room is not due to the indoor source but to the outdoor one. In particular, the average **E**-field

TABLE 10.7

Exposure Field (rms Values) for the Indoor Scenario (Coexisting Outdoor GSM BTS and Indoor Wi-Fi AP)

	$E_{\text{vol peak}}$ (V/m)	$E_{\text{vol ave}}$ (V/m)	$E_{\text{sup ave}}$, min.–max. (V/m)
GSM900	5.57	3.13	2.73–3.44
GSM1800	3.61	1.70	1.62–1.91
Total GSM	6.18	3.56	3.19–3.93
Wi-Fi	2.51	1.13	1.05–1.19
Total	6.30	3.74	3.40–4.09

TABLE 10.8
SAR Values for the Indoor Scenario (Coexisting Outdoor GSM BTS and Indoor Wi-Fi AP)

	SAR_{WB} (mW/kg)	SAR_{1g} (mW/kg)	SAR_{10g} (mW/kg)
GSM900	0.109	2.41	1.08
GSM1800	0.027	1.31	0.58
Total GSM	0.136	3.07	1.46
Wi-Fi	0.014	0.79	0.35
Total	0.150	3.66	1.60

value attributable to the Wi-Fi system is as low as 1 V/m. The computed data also demonstrate that coexistence of the two systems (GSM and Wi-Fi) is possible without exceeding the reference levels for the exposure field, as averaged over the volume occupied by the body or over an equivalent surface, even if the particularly stringent limits issued by some national regulations (e.g., 6 V/m) are considered. Finally, the SARs presented in Table 10.8 suggest that a typical exposure scenario results in RF absorption that is two orders of magnitude below the basic restrictions, both for whole-body and for locally averaged SAR.

10.4. 2.5 Coupling of Transien t EM Pulses into the Hum an Body

Electromagnetic transient radiations are widely used for studying the susceptibility of test objects to broadband EMPs, and increasingly, pulsed fields are being explored for telecommunication purposes. The main characteristics of these pulse fields are waveforms that include high peak powers, fast rise times, and a narrow pulse width. Earlier investigations on their interaction with biological systems relied on mathematical analyses of canonical shapes of dielectric equivalent bodies, such models as planar tissue layers and bodies of revolution [131–134]. The well-known effect of microwave hearing from pulse-induced thermoelastic pressure in the human head have been investigated both analytically [135–140] and numerically [141–143]. More recently, major strides have been made in the development of UWB systems for wireless telecommunications [144,145]. It promises a powerful combination of low power, high throughput, greater range, and better inherent security, using nanosecond pulses. This section presents predictions of fields and power depositions, which have been obtained from the frequency-dependent FDTD formulations described in Section 10.4.1.5, for models of the biological body.

10.4.2.5.1 Modeling of Tissue Properties with the Debye Equation

For UWB calculations using the $(FD)^2TD$ method, the measured properties for the various tissues may be fitted to the Debye equation (Equation 10.14) with two relaxation constants [77–79]. For the results shown here, the measured properties of biological tissues (muscle, fat, bone, blood, intestine, cartilage, lung, kidney, pancreas, spleen, lung, heart, brain/nerve, skin, and eye) were obtained from the literature. Optimized values for ε_{s1}, ε_{s2}, ε_{∞}, τ_1, and τ_2 in Equation 10.14 were obtained by nonlinear least squares matching to the measured data for fat and muscle (Table 10.9), with τ_1 and τ_2 being the average of the optimized values for fat and muscle. All other tissues have properties falling roughly between these two types of tissues. This was done to facilitate volume averaging of the tissue properties in cells of the heterogenous human model. Having τ_1 and τ_2 constant for all tissues, allowed linear (volume) averaging of the ε values for each tissue in a given cell to calculate ε values for that cell.

TABLE 10.9

Debye Constants for Tissues, $\tau_1 = 46.2 \times 10^{-9}$ s and $\tau_2 = 0.91 \times 10^{-10}$ s (Average of Optimum for Fat And Muscle)

Tissue	ε_∞	ε_{s1}	ε_{s2}
Muscle	40.0	3948	59.09
Bone/cartilage	3.4	312.8	7.11
Blood	35.0	3563	66.43
Intestine	39.0	4724	66.09
Liver	36.3	2864	57.12
Kidney	35.0	3332	67.12
Pancreas/spleen	10.0	3793	73.91
One-third lung	10.0	1224	13.06
Heart	38.5	4309	54.58
Brain/nerve	32.5	2064	56.86
Skin	23.0	3399	55.59
Eye	40.0	2191	56.99

10.4.2.5.2 Induced Currents and SAs

The $(FD)^2TD$ formulation has been used to calculate coupling of an ultrashort pulse to the heterogenous model of the human body. From the calculated internal fields, the vertical currents passing through the various layers of the body are calculated by using the following equation:

$$I_z(t) = \delta^2 \sum_{i,j} \frac{\partial D_z}{\partial t} \tag{10.25}$$

where δ is the cell size ($=1.31$ cm), and the summation is carried out for all cells in a given layer. The layer-averaged absorbed energy density or SA and the total energy W absorbed by the whole body can be calculated using the following relationships:

$$\mathrm{SA}|_{\text{layer } k} = \frac{\delta t}{N_k} \sum_{i,j,t} \frac{E(i,j,k,t)}{\rho(i,j,k)} \frac{\partial D(i,j,k,t)}{\partial t} \tag{10.26}$$

$$W = \delta t \delta^3 \sum_{i,j,k,t} E(i,j,k,t) \frac{\partial D(i,j,k,t)}{\partial t} \tag{10.27}$$

In Equation 10.26 and Equation 10.27, δt is the time step ($=\delta/2c = 0.02813$ nsec) used for the time domain calculations, N_k is the number of cells in layer k of the body, and $\rho\,(i,j,k)$ is the mass density (in kg/m^3) for each of the cells in the corresponding layers.

A typical time domain, UWB pulse with a peak amplitude of 1.1 V/m is shown in Figure 10.23. It is interesting to note that the pulse has a rise time of about 0.2 nsec and a total time duration of about 7 to 8 nsec. The Fourier spectrum of the pulse is shown in Figure 10.24. Most of the energy in the pulse is concentrated in the 200- to 900-MHz band with the peak of the energy being at about 500 MHz.

For purposes of illustration, the results that follow assume the incident fields to be vertically polarized, since this polarization is known to result in the strongest coupling for standing individuals [146]. Also, a uniform plane wave illumination of the whole body is assumed by the incident fields. The $(FD)^2TD$ procedure is used to calculate the temporal

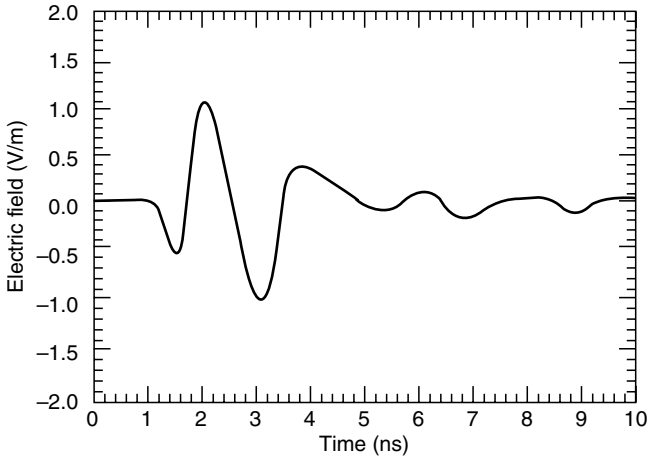

FIGURE 10.23
A representative UWB EMP. Peak incident field = 1.1 V/m.

variations of total vertical currents for the various sections of the body for both the shoe-wearing grounded and ungrounded exposure conditions of the model. The current variations for a couple of representative sections such as those through the eyes and the bladder are given in Figure 10.25a and b, respectively. The calculated peak currents for the various sections are on the order of 1.1 to 3.2 mA/(V/m). It is interesting to note that there is very little difference in the induced currents, whether the model is grounded or not. This is due to the fact that most of the energy in the pulse is at frequencies in excess of 300 MHz, where the effect of the ground plane on the induced currents or the SARs is minimal.

In Figure 10.26, the peak current for each section of the body is plotted with a section resolution of 1.31 cm. The maximum peak sectional current of 3.5 mA, which is equal to 3.2 mA/(V/m), occurs at a height of 96.3 cm above the bottom of the feet. A very similar result also had been observed for calculations using isolated and grounded models of the human body for plane wave exposures at frequencies of 350 to 700 MHz, where the highest induced currents on the order of 3.0 to 3.2 mA/(V/m) were calculated for sections of the body that are at heights of 85 to 100 cm relative to the feet.

The SA and the total absorbed energy for exposure to the UWB pulse can be calculated using Equation 10.26 and Equation 10.27. The total energy absorbed by the body exposed

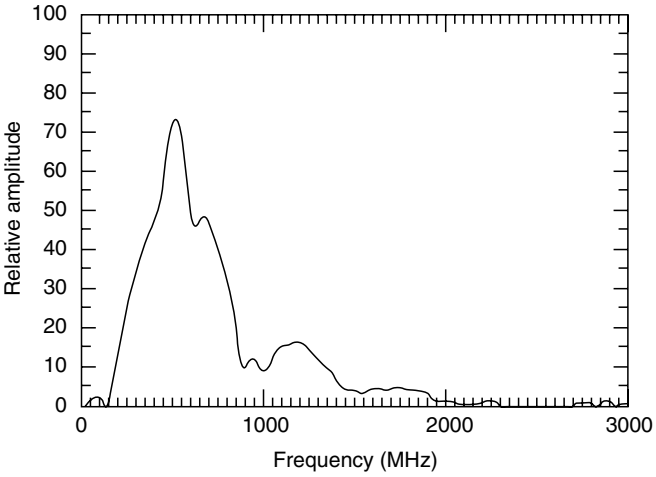

FIGURE 10.24
Fourier spectrum of the EMP of Figure 10.23.

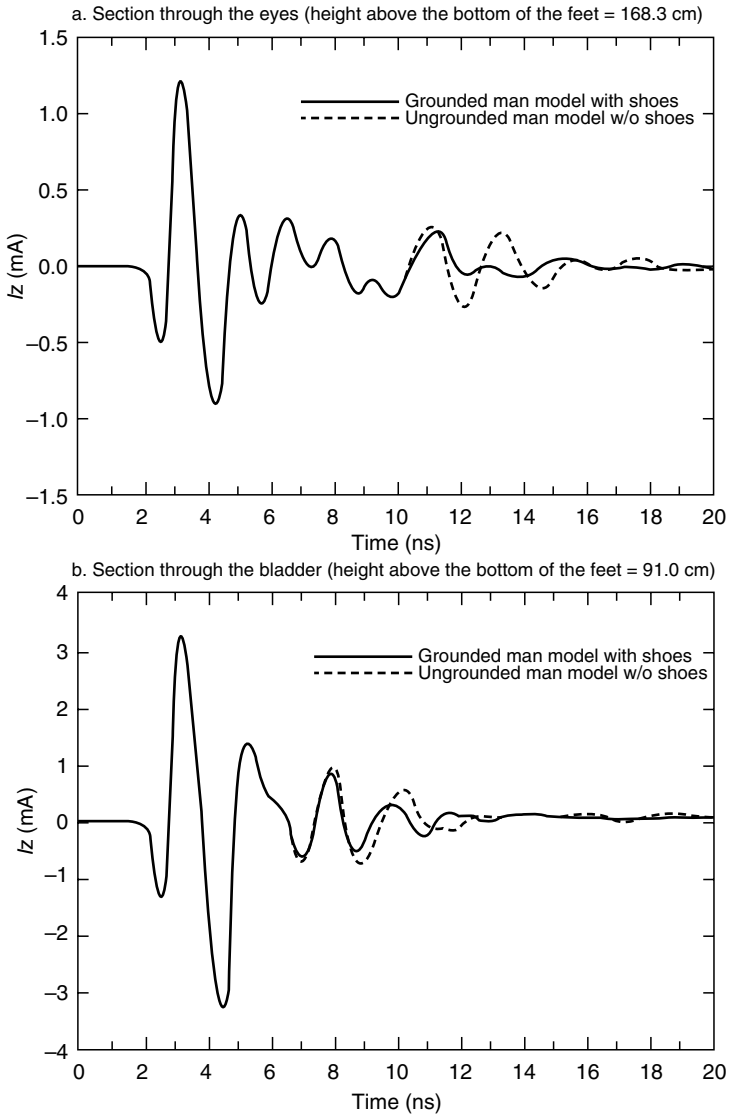

FIGURE 10.25
Currents induced for the various sections of the body for shoe-wearing grounded and ungrounded conditions of exposure. $E_{peak} = 1.1$ V/m.

to a single pulse of the type shown in Figure 10.23 is 2.0 and 1.91 pJ for isolated and shoe-wearing grounded conditions, respectively.

10.4.2.6 Absorption in the Head of Cellular Phone Users

The widespread use of cellular mobile telephone systems has brought about an increased concern for possible adverse health effects from the RF field emitted by the handset. Indeed, exposure standards have been mandated by various national bodies to limit human exposure to cell phone radiations. These RF exposure standards provide specifications in terms of power deposition per unit mass, that is, SAR induced in the user's head, with which cell phones must comply [100,101].

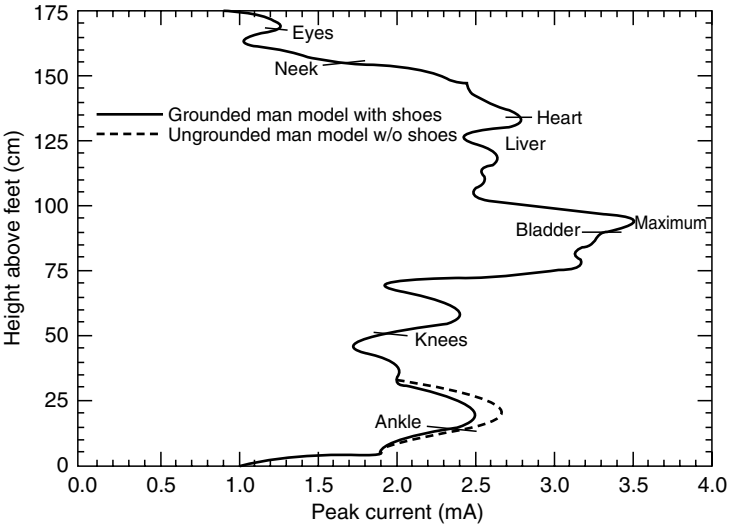

FIGURE 10.26
Peak currents induced for the various sections of the body for shoe-wearing grounded and ungrounded conditions of the model. $E_{\text{peak}} = 1.1$ V/m.

Laboratory procedures for compliance testing of mobile phones are based on experimental measurements, performed according to published protocols [147,148]. In these tests, real phones and phantom head models, shells filled with a material with dielectric properties equivalent to those of the brain tissue at the frequencies of interest, are used. Clearly, the phantom is a simplified model of the human head and is specifically designed for compliance testing. Consequently, it is not suited for an accurate analysis of the SAR distribution in various tissues and organs of the head. A detailed analysis of the distribution of the power absorption would be required to obtain a better understanding of SARs inside the head. Such information is needed for the necessary extrapolation of results from *in vivo* and *in vitro* experimental studies devoted to investigating the effects of RF radiation on humans. They would provide the exposure data needed in epidemiological studies aimed at evaluating any possible dose–effect relations.

Increasingly, advances in computational bioelectromagnetics have made detailed evaluation of SAR distribution inside the human head possible through the use of accurate and realistic models of the human head and the source, that is, the mobile phone, and the use of suitable numerical methods such as the FDTD technique.

The first numerical studies were performed by simulating the phone radiating element as a half-wavelength dipole or a quarter-wavelength monopole mounted on a box [149–154]. These antenna models, and the last in particular, can only be used as a rough model of the retractable antenna, which at the beginning was in nearly all cell phone handsets. However, at present, the need for more and more compact terminals and for dual-band operation has given rise to new antenna types. In particular, two types of antennas have been developed: planar integrated antennas and helical antennas. While half-wavelength dipoles and monopoles can be easily implemented inside an FDTD code, modeling of helix or planar antennas can become a rather difficult task.

The difficulties in modeling helical structures with the FDTD method were revealed in some recent studies. For example, only rather large structures have been studied employing a pure FDTD scheme [155,156]. For smaller structures, published reports had either employed equivalent sources [157] or a hybrid MoM–FDTD technique [158,159]. While these reports show some problems and drawbacks, investigations using FDTD, properly

modified through the use of a graded mesh, have obtained good agreement with MoM and experimental results [160,161]. In these studies, both near-field and radiation patterns of dual-band cell phones equipped with a helical antenna have been reproduced. Moreover, the SAR distributions inside the VH model of the head have been computed, showing a higher penetration depth at 900 MHz and higher superficial SARs at 1800 MHz. Moreover, approximately 80% and 50% of the radiated power was absorbed inside the head at 900 and 1800 MHz, respectively. For a phone in contact with the ear and tilted to bring its axis along the ear–mouth direction (the so-called cheek position), radiating an average power of 250 mW at 900 MHz and 125 mW at 1800 MHz, peak 1-g SARs of 1.65 and 1.08 W/kg were obtained in the head at 900 and 1800 MHz, respectively. In the same examples, the peak 1-g SARs in the brain were 0.13 and 0.06 W/kg at the two considered frequencies, respectively.

Planar antennas can be mounted on the top, lateral, or back sides of the phone [162–165]. Shorted patch antennas typically have a 10-dB bandwidth between 5% and 10% that can be increased to about 12% by parasitically coupling another printed radiator in the vertical direction (stacked patch). For comparison, the bandwidth is about 30% for the monopole antenna [163]. In this case, an important consideration is the influence of the hand wrapped around the handset. For a cell phone equipped with a planar antenna, the hand has a detuning effect on the antenna resonant frequency and causes a reduction of the bandwidth; both are evident where the hand masks the antenna. About 30% of the radiated power was absorbed by the hand, while for the monopole the hand absorption was only 15% [162]. For a radiated power of 250 mW at the frequency of 900 MHz and a head–handset separation of 2 cm, the computed peak 1-g SAR was 0.95 W/kg for a laterally mounted planar inverted F antenna (PIFA), and the result was 0.49 W/kg for a monopole antenna [162]. When a phone equipped with a side-mounted PIFA was kept in contact with the ear, the peak 1-g SAR increased to 1.4 W/kg [164]. Note that the back-mounting configuration gave rise to a substantial (up to three times) reduction in the peak SAR [162].

Another important task for an accurate evaluation of the power absorption in the head is the model adopted for the phone case. The typical approach, followed in the literature, consists of representing the case as a box, that is, a plastic-coated metal parallelepiped [149–165]. In order to model the correct shape of cell phones, both CAD files [166] and topometric sensors [167] have been used. However, in most previous studies, the internal structures of the phone have been modeled simply as a homogenous perfect conductor. Recently, CAD files have been used also to model the internal structures (printed circuit board, battery, keypad and buttons, etc.) of the phone [168]. An alternate approach to a suitable numerical model of the mobile phone was proposed by Pisa et al. [169]. It starts with a simplified model, which includes only the main phone parts (antenna, keyboard, internal box, plastic coating, etc.) having ''realistic'' dimensions and electric properties. The realistic parameters are then tuned by using an optimization procedure, which minimizes a functional that depends on the differences between the measured and simulated electric and magnetic fields in front of the phone and on the SAR inside a cubic phantom. As an example for the applicability of the proposed optimization method, a numerical model of a commercial phone, operating at 900 MHz, was implemented, and the power deposition in the VH model of the human head was computed for various phone–head distances. The results in terms of peak SAR in various head organs and tissues and for various phone–head distances are presented in Table 10.10. The SAR_{1g} and SAR_{10g} show a monotonic decrease when the phone–head distance increases, while the peak SARs inside the head tissues reach their maxima when the phone is kept at specific distances from the head. This behavior is due to the fact that with the telephone pressed against the head, the power absorption is confined to a limited region in front of the

TABLE 10.10

Peak SAR Averaged over 1 g (SAR_{1g}) and 10 g (SAR_{10g}) and Peak SAR as Averaged over 1 g in Various Organs and Tissues, for Different Distances between the Phone and the Visible Human Phantom for a Radiated Power of 250 mW at 900 MHz

	SAR_{1g} (W/kg)	SAR_{10g} (W/kg)	$SAR_{1\ brain}$ (W/kg)	$SAR_{1\ eye}$ (W/kg)	$SAR_{1\ skin}$ (W/kg)	$SAR_{1\ muscle}$ (W/kg)	$SAR_{1\ fat}$ (W/kg)	$SAR_{1\ gland}$ (W/kg)
$d = 0$ mm	1.450	0.600	0.125	0.0102	0.504	0.223	0.142	0.448
$d = 2$ mm	0.740	0.500	0.123	0.0101	0.504	0.244	0.162	0.493
$d = 6$ mm	0.670	0.470	0.174	0.0100	0.482	0.278	0.165	0.471
$d = 8$ mm	0.630	0.450	0.109	0.0103	0.460	0.280	0.160	0.445
Cheek position ($d = 0$ mm) optimized	0.810	0.410	0.088	0.0360	0.171	0.447	0.301	0.420
Cheek position ($d = 0$ mm) nonoptimized	2.568	0.888	0.177	0.0578	0.315	0.721	0.400	0.664

antenna feed point, whereas by moving the handset away from the head, a greater portion of the head is exposed. When the distance was further increased, the SAR decreased monotonically as a result of the decay in field intensity. This study also showed that the use of inaccurate phone models (last row in Table 10.10) could give rise to SARs, averaged over 1 g, up to three times higher than those computed for the optimized model [169].

Faced with a rapid saturation of the cellular phone market, many cell phone manufacturers and service providers are turning their attention toward youths in promoting handsets that are cheap, with inexpensive service plans, or both [170]. An issue of particular interest is the possible difference in power absorption between children and adults. To answer this question, the first problem to be addressed is the realization of an accurate numerical model of a child's head. Because of ethical concerns, the availability of anatomical models of children has been limited. The common approach for obtaining a model of the child has been the reduction of the dimensions of the voxel size of adult models. Sometimes, this reduction was performed by employing different scaling factors for the different parts of the head. It appears that dielectric constants for children may be considerably higher than adults [171]. However, since the detailed data for the dielectric properties of tissues in children are scarce, they are usually assumed to be equal to those of adults or generically increased by a constant factor in most models. Nevertheless, using these models, some papers have reported increases of up to 50% in the peak 1-g SARs in the child head, compared to an adult head, for exposure to cell phones operating at frequencies around 835 and 1900 MHz [151,172]. A similar increase has been observed in the peak 1-g SARs obtained in the brain. A possible explanation of these results is the larger depth of penetration of power in the child models as compared to the adult one [151,172]. Other papers devoted to the investigation of differences between child and adult exposure to cellular phones have shown no significant difference in peak 1-g SAR between adults and children [173,174]. There are several possible explanations for the discrepancy. It has been suggested that the contradictory results may be due to the different phone excitation schemes used by different authors [175]. The disparity in distances of separation between the antenna and the head also was suggested as a pivotal factor in determining the reported discrepancies [170].

In an effort to help resolve the discrepancies, the SAR distributions induced in two child's head models, an isotropic scaling of the VH head (child size, CS) and an

TABLE 10.11

Peak SAR Averaged over 10 g (SAR_{10g}) and Peak SAR as Averaged over 1 g in Various Organs and Tissues, for Radiated Powers of 250 mW at 900 MHz and 125 mW at 1800 MHz in Children and Adults

		SAR_{10g} (W/kg)	$SAR_{1\ skin}$ (W/kg)	$SAR_{1\ muscle}$ (W/kg)	$SAR_{1\ bone}$ (W/kg)	$SAR_{1\ csf}$ (W/kg)	$SAR_{1\ brain}$ (W/kg)
900 MHz	VH	0.67	2.00	0.67	0.20	0.34	0.16
	CS	1.18	4.02	1.03	0.31	0.45	0.25
	CL	1.03	1.15	0.41	0.14	0.23	0.20
1800 MHz	VH	0.39	0.99	0.30	0.08	0.12	0.08
	CS	0.29	0.87	0.30	0.08	0.13	0.09
	CL	0.27	0.91	0.30	0.06	0.15	0.10

tanisotropic scaling of the VH head (childlike, CL), have been computed and compared with SAR distributions induced in the VH by a mobile phone equipped with a back-mounted dual-band patch antenna [176]. Some of the results are presented in Table 10.11. It can be seen that the peak SAR_{10g} showed an increase of about 50% and a reduction of about 25% for the child models compared to the adult model at 900 and 1800 MHz, respectively. Moreover, as the brain is closer to the mobile phone in the case of CS and CL heads, the SAR_{1g} in the brain of children is slightly more significant than that for the adult.

Other exposure scenarios also have been investigated, including head exposure inside a car and cell phones not placed in contact with the ear. In some studies, the influence of the metallic and dielectric structures of a car on SAR induced by a cellular phone inside an adult head was analyzed [155,177–179]. Studies performed by modeling the whole car have shown that the main influence on SAR distribution was due to structures that were very close to the head [178,179]. In particular, the presence of a vertical glass wall in parallel with the antenna axis did not significantly influence the SAR distribution, while a metallic wall can cause up to an 80% increase in the peak 1-g SAR [155,177]. The presence of a reflecting wall placed horizontally over the head, simulating the roof of a car, rendered the SAR distribution more uniform, increasing the lower values and reducing the higher ones [155].

Cellular phones commonly are used in contact with the ear. However, when they are used with a headset, they can be positioned at different body locations. Moreover, unintentional exposures also might occur for a subject standing close to someone using a cellular phone, for example, in a crowded environment. The peak SAR produced by a phone placed slightly above the navel of the VH model has been calculated by using the FDTD method, and the results have been compared to those of a flat phantom—modeled as a multilayered transmission line—whose thickness was varied statistically [180]. The exposure of a human subject to a half-wavelength dipole placed at various positions at a distance of 9 mm from the body surface also has been investigated [181]. In particular, 11 different locations have been considered, that is, in front of the right ear and left ear, the nose, eye, heart, lung, shoulder, stomach, hip, lower back, and the groin. The computed results showed that the maximum values of SAR_{1g} and SAR_{10g} occurred, in all cases, when the phone is close to the ear. For all other positions, corresponding to possible locations of the phone when used in conjunction with a headset, peak 1-g SAR values were at least 30% lower than those obtained in the common ear position.

10.5 Temperature Elevations Induced in Biological Tissues by EM Power Absorption

10.5.1 Introduction

EM energy impinging on the human body induces currents and fields inside the body. A major biological response from absorption of EM energy in the RF and microwave frequency range is the elevation of tissue temperature. Consequently, most internationally recognized guidelines for limiting human exposure to EMFs in the RF and microwave range use SAR as the basic dosimetric metric [100,101]. Likewise, the vast majority of studies available in the literature, addressing the topic of human exposure to EMFs, focus their attention on the dosimetric problem of quantifying induced power absorption inside the exposed subject. A central premise of these exposure guidelines is to protect exposed subjects against temperature increases exceeding the threshold for induction of adverse thermal effects. Therefore, an increasing number of investigators are beginning to address the problem of human exposure to EMFs with a thermal analysis to estimate the temperature increment induced inside the exposed subject.

Another domain in which a thermal analysis can be very useful, or even essential, is that of therapeutic applications where EMFs are deliberately used to cause predefined temperature increases in specific target tissues in the body. Some of the applications include hyperthermia cancer treatment and microwave tissue ablation. In such cases, performing a numerical electromagnetic and thermal study of the applicator in its intended operating environment, inside the body, can be a valuable aid in designing the applicator, in establishing the clinical protocol (i.e., power to be delivered, time of application, etc.), and for treatment planning purposes.

In the following, an overview of the available analytical formulations to characterize heating induced by EMFs is presented. Some numerical implementations, suitable to study the thermal problem in realistic situations, are summarized with specific examples.

10.5.2 Bio-Heat Equation

The bio-heat equation (BHE) was originally proposed by Pennes in 1948 to analyze temperature distributions in a resting forearm [182]. Subsequently, it has been modified to study phenomena of heat transport and exchange for the whole body [183,184]. It is an analytical model that describes the temperature distribution $T = T(\mathbf{r},t)$ inside the body. One of the more general formulations of the BHE is given here for temperature rises associated with exposures to EMFs:

$$\nabla \cdot (K(\mathbf{r})\nabla T) + A(\mathbf{r},T) + Q_{\mathrm{v}}(\mathbf{r}) - R_{\mathrm{L}}(\mathbf{r}) - B(\mathbf{r},T)(T - T_{\mathrm{B}}) = C(\mathbf{r})\rho(\mathbf{r})\frac{\partial T}{\partial t}\,(\mathrm{W/m^3}) \qquad (10.28)$$

The five terms on the left side of Equation 10.28 represent heat accumulation (or loss) per unit time and per unit volume at a point inside the body. Specifically, the various ways through which heat is transferred, produced, or removed from the tissue are:

- Heat transfer through internal conduction, where K (W/(m°C)) is the tissue thermal conductivity
- Metabolic heat production (A [W/m^3])
- Electromagnetic power deposition (Q_{v} [W/m^3])

- Respiratory heat losses in the lungs (R_L [W/m^3])
- Heat exchange due to capillary blood perfusion, which is proportional to blood flow and is represented by the parameter B (W/(°C m^3)), and the difference between blood and tissue temperature ($T_B - T$); note that T_B is a function of time (i.e., $T_B = T_B(t)$)

The right side of Equation 10.28 denotes the temperature increase (or decrease) per unit time. The thermal capacitance per unit volume is given by the product between the tissue specific heat, C (J/(kg°C)) and density, ρ (kg/m^3).

It should be mentioned that the BHE assumes that heat exchange with blood takes place exclusively via capillary perfusion. In reality, heat exchange also occurs with large blood vessels. This mechanism does not take the form of a distributed exchange throughout the tissue volume, like the $B(T - T_B)$ term in the BHE, but instead, the form of a localized exchange at the blood vessel walls. To account for it would require the introduction of an additional term in the BHE [185,186]. Moreover, it would require precise knowledge of the structure of the vasculature inside the biological body, which is not always available. However, this mechanism only alters temperature distribution near large blood vessels and does not significantly affect the overall temperature distribution, especially the maximum temperature increases elsewhere in an exposed body [187]. Therefore, this mechanism can generally be neglected without significant loss of accuracy, if the principal purpose is to assess safety compliance of a given exposure situation, from the thermal point of view. On the other hand, proper inclusion of large blood vessels may be important when planning hyperthermia or ablation treatments. The presence of a large blood vessel in the target region may cause temperature elevations to remain below the minimum threshold required for effective treatment.

A first step in using the BHE to compute the temperature increases induced by exposure to EMFs is the evaluation of SAR or local power deposition. In fact, $Q_v = \rho$ SAR is the exogenous heat source responsible for the alteration in temperature profiles inside the exposed subject. Once the Q_v term is determined, the BHE would provide the time evolution of temperature, provided that appropriate initial and boundary conditions are imposed, as discussed later. In this manner, the BHE allows assessment of both the transient response and steady-state temperature increases.

An implicit assumption in the above discussion is that the electromagnetic and thermal problems are independent and can be investigated sequentially. This is equivalent to assuming that electromagnetic transients are irrelevant and therefore the steady-state SAR distributions can be used as the input for the thermal analysis, and that changes in tissue temperature do not alter the field distribution inside the tissue. Concerning the first assumption, the time constants of the electromagnetic and thermal processes are of orders of magnitude different, with the EMF reaching steady state at most after a few microseconds, while thermal constants inside living biological tissues are of the order of a few minutes under usual circumstances. This means that electromagnetic transients can indeed be neglected for the thermal analysis. The second assumption, instead, deserves some more attention. In fact, dielectric constants of biological tissues are temperature dependent, and therefore, the EMF distribution could change as heating proceeds and temperature increases. However, this effect may be neglected so long as the temperature elevation is small, that is, on the order of a few degree Celsius, as is expected for common EMF exposures. If temperature increase is large and the induced variation in dielectric constants is no longer negligible, for example, when heating food in a microwave oven, the electromagnetic and thermal problems must be solved in a coupled manner, iteratively updating the electromagnetic solution as heating progresses [188–190].

10.5.2.1 Initial Conditions

The BHE is a partial differential equation in time and space; its solution requires the specification of both initial and boundary conditions. For studies involving RF- and microwave-induced heating inside the human body, the initial temperature distribution typically is set to the physiological norm, computed as the steady-state solution of Equation 10.28 in the absence of external power deposition ($Q_v = 0$). Thus, the resulting equation is

$$\nabla \cdot (K(\mathbf{r})\nabla T) + A_0(\mathbf{r}) - R_L(\mathbf{r}) - B_0(\mathbf{r})(T - T_{B0}) = 0 \ (\mathrm{W/m^3}) \tag{10.29}$$

In this case, thermal parameters do not depend on temperature and are set to their physiological values at approximately 37°C. Similarly, the physiological value at rest is used for blood temperature. Note that Equation 10.29 does not contain time derivatives and, therefore, does not require any initial condition to be solved.

10.5.2.2 Boundary Conditions

Boundary conditions are needed to account for the heat exchange between the body surface, namely, the skin, and the external environment, in both the general and the steady-state formulations of the BHE as represented by Equation 10.28 and Equation 10.29, respectively. The simplest boundary conditions that can be applied are the adiabatic condition, that is, a thermally insulated surface, or the Dirichelet boundary condition, that is, an enforced surface temperature. Adiabatic conditions can be used to model tissue surfaces in close contact with highly insulating materials, such as the catheters used to insert antennas employed in hyperthermia or ablation treatment. In contrast, Dirichelet boundary conditions can be used for surfaces in close contact with a circulating fluid kept at a constant temperature (forced convection).

Adiabatic and Dirichelet boundary conditions are rather simple but they are not suitable for representing the general heat exchanges that take place at the skin. A general boundary condition, obtained by imposing the continuity of the heat flow perpendicular to the surface of the body, can be expressed as [191]:

$$-K(\mathbf{r})(\nabla T \cdot \mathbf{n}_0)_S = H(T_s - T_A) + \mathrm{SW}(T)(\mathrm{W/m^2}) \tag{10.30}$$

where S is the skin surface and $\mathbf{n}_0$ is the outward unit vector normal to S. The terms on the right side of Equation 10.30 represent the two ways in which heat is exchanged with the environment. In particular, the first term describes heat loss due to convection, and it is proportional to the difference between skin temperature (T_S) and ambient air temperature (T_A) through the convection coefficient H (W/(m^2°C)). The last term represents heat loss due to sweating (SW).

A few words are needed about radiative heat exchange. If one assumes the body surface is surrounded by objects that are all at the same ambient temperature T_A, the expression for heat exchange through radiation from the body surface to the environment, per unit area, is given by [192,193]:

$$Q_r = e\sigma(T_s^4 - T_A^4)(\mathrm{W/m^2}) \tag{10.31}$$

where e is the surface emissivity, σ is Stefan–Boltzmann's constant, and the temperatures are expressed in degrees Kelvin (K). Under normal conditions, T_S and T_A do not differ significantly from about 300 K, and Equation 10.31 can be approximated as [193]:

$$Q_r = H_r(T_s - T_A)(W/m^2) \tag{10.32}$$

where H_r is an equivalent convection coefficient. Therefore, the convective term in Equation 10.32 can effectively model both convective and radiative heat exchanges, by using an overall convection coefficient that also takes into account the equivalent convection parameter H_r in Equation 10.32. There are cases, however, in which the surrounding objects are at different temperatures. In such circumstances, the problem becomes very complex and a possible solution, based on the use of an RT method to connect mutually visible surfaces and consider radiant heat transfer between them, has been proposed [194]. However, the simple approach of an equivalent convection is generally sufficient for an accurate analysis of the thermal problem.

It is worthy of mention that the convective boundary condition also can be used to represent an adiabatic condition by simply setting the convective coefficient to zero. It can also represent an approximate Dirichelet boundary condition, by using a very high convective coefficient and setting T_A equal to the imposed surface temperature.

10.5.3 Thermoregulatory Responses

The temperature of the human body is regulated to within a narrow range of about 37°C, in its core. Under normal circumstances, this is accomplished through an exquisite thermoregulatory mechanism involving sweating and vasodilatation (see Chapter 5 by Black for more details on thermoregulation [285]). The thermoregulatory mechanism is activated whenever the temperature $T(\mathbf{r})$ in specific parts of the body, where thermal sensors are placed, shifts from its basal value $T_0(\mathbf{r})$. In particular, the basal temperature distribution $T_0(\mathbf{r})$, which corresponds to a state of ''thermal comfort,'' is the one obtained in a naked subject when the external air temperature T_A is about 30°C (in a dry environment) [184,195].

Since a part or all of the absorbed electromagnetic energy is converted into heat inside the human body, computations of tissue temperature must take into account the thermoregulatory mechanisms in response to the heat input from RF and microwave absorption, starting from a state of thermal comfort [195]. Specifically, the presence of thermoregulatory mechanisms causes some of the terms in Equation 10.28 and Equation 10.30 to vary with body temperature. The first term that shows a dependence on temperature in Equation 10.28 is metabolic heat production, which may be characterized by the following equation [196]:

$$A(\mathbf{r},T(\mathbf{r})) = A_0(\mathbf{r})(1.1)^{(T(\mathbf{r})-T_0(\mathbf{r}))} \tag{10.33}$$

where A_0 is the basal metabolic rate in the tissue. Equation 10.33 shows that metabolic heat production depends only on local tissue temperature. It must be noted that this dependence is not related to thermoregulation but rather to the fact that metabolic processes are slightly accelerated when the temperature increases.

With regard to the variation of blood flow, there are two different, but essential, phenomena: one for internal tissue perfusion and the other for peripheral (skin) perfusion. For blood perfusion to the internal tissues, the regulation depends only on local tissue temperature [196,197]. Thus, in a simple model, blood perfusion could be assumed to be at its basal value B_0 until the local temperature reaches 39°C. When the local temperature exceeds 39°C, the blood perfusion starts to increase linearly with temperature in order to enhance the local heat removal process, until the local temperature rises to above a value of about 44°C. At this point, the increasing rate of blood perfusion arrives at a maximum. Accordingly, the internal blood perfusions are modeled by the following expressions:

$$B(\mathbf{r},T(\mathbf{r})) = B_0(\mathbf{r})\ T(\mathbf{r}) \leq 39^{\circ}\mathrm{C} \tag{10.34}$$

$$B(\mathbf{r},T(\mathbf{r})) = B_0(\mathbf{r})[1 + S_B(T(\mathbf{r}) - 39)]\ 39^{\circ}\mathrm{C} < T(\mathbf{r}) < 44^{\circ}\mathrm{C} \tag{10.35}$$

$$B(\mathbf{r},T(\mathbf{r})) = B_0(\mathbf{r})(1 + 5S_B)\ T(\mathbf{r}) \geq 44^{\circ}C \tag{10.36}$$

The above model of the internal temperature regulation mechanism is rather simple. A more complex temperature control model, instead, would include regulation of blood perfusion in the skin through vasodilatation. In particular, two different signals are used as feedback to regulate vasodilatation: one is the hypothalamic temperature increase ($T_H - T_{H0}$), used as an indicator of the elevation of the body core temperature, and the other is the average skin temperature increase $\overline{\Delta T}_s$, defined as follows:

$$\overline{\Delta T}_s = \frac{\int_S (T(\mathbf{r}) - T_0(\mathbf{r}))\,dS}{S} \tag{10.37}$$

where S is the skin surface of the body. The two feedback signals are assigned different weights, with a greater importance given to the hypothalamic temperature, and then used, together with local skin temperature, to regulate skin blood flow according to [183,184]:

$$B(\mathbf{r},T(\mathbf{r})) = \left[B_0(\mathbf{r}) + F_{HB}(T_H - T_{H0}) + F_{SB}\overline{\Delta T_S}\right]2^{(T(\mathbf{r})-T_0(\mathbf{r}))/6} \tag{10.38}$$

where F_{HB} and F_{SB} are the weights of the hypothalamic and skin temperature signals, respectively.

From the above discussion, it can be noted that blood acts as a heat transfer agent, taking heat away from the inner body parts, whose temperature is higher than that of the blood, and bringing this heat to the body periphery. There, heat is passed to the skin layers, whose temperature is lower than that of the blood, and dissipated through sweating and evaporation. During microwave irradiation, the net heat exchange, between blood and the various body tissues, is different from zero, and consequently the blood temperature T_B varies according to the following equation:

$$Q_{BTOT} = C_B\rho_B V_B \frac{\partial T_B}{\partial t}(\mathrm{W}) \tag{10.39}$$

where Q_{BTOT} is the net rate of heat acquisition of the blood from the body tissues, C_B and ρ_B are the blood specific heat and mass density, respectively, and V_B is the total blood volume, assumed equal to about 5 L [198]. When the thermal equilibrium is reached, the net heat exchange is null, and therefore blood temperature stays at a constant value, slightly higher than the basal one.

The feedback mechanism that regulates sweating (SW in Equation 10.30) is very similar to that regulating peripheral blood flow and can be described as follows [183,184]:

$$\mathrm{SW}(\mathbf{r},T(\mathbf{r})) = \left[\mathrm{PI} + F_{HS}(T_H - T_{H0}) + F_{SS}\overline{\Delta T_S}\right]2^{(T(\mathbf{r})-T_0(\mathbf{r}))/10} \tag{10.40}$$

where PI represents *perspiratio insensibilis* (insensible perspiration), that is the basal evaporative heat loss from the skin.

In fact, this model still represents a simplification of the thermoregulatory system of the human body, which is very complex. For example, the skin from different parts of the body does not have the same sweating behavior, as implied by Equation 10.40, and there exist other internal temperature sensors, besides the hypothalamus. Notwithstanding these limitations and the great variability in thermoregulatory behavior among different subjects, the model can be considered a good starting point to assess thermal responses in a human subject exposed to an EMF. It must also be observed that in most practical situations, induced thermal elevations are very small and thermoregulatory responses may not be invoked, so that basal physiological values for thermal parameters may be assumed for the BHE.

10.5.4 Numerical Methods for Solving the Thermal Problem

The combination of the BHE and the thermal boundary condition represent a complicated problem, which can become nonlinear if thermoregulatory mechanisms are considered. Analytical solutions of this problem, neglecting thermoregulation, can be obtained only for simplified body geometries and exposure conditions, which allow an analytical determination of the SAR distribution. For example, an analytical solution in stratified media may be obtained as an expansion in eigenfunctions, which are applicable to planar, cylindrical, and spherical multilayer geometries [199,200]. Also, an analytical solution for the case of a multilayer slab has been investigated in terms of Green's functions [201]. More complicated solutions, able to take into account thermoregulatory mechanisms, have also been developed, based on a simplified cylindrical segment approximation of the human body [183,184,202,203]. In particular, the thermal behavior of the human body is simulated by means of two systems: a controlling system and a controlled one. The controlled system, modeled by the BHE, determines the temperature distribution inside the body, while the controlling system provides feedback signals able to modify the thermal parameters of the controlled one in order to maintain a constant body core temperature (thermoregulation). The principal limitation of this approach stems from modeling the body as a few homogenous cylindrical segments, each having a uniform SAR and temperature distribution.

When studying more realistic and detailed geometries, like an anatomically based body model, analytical or cylindrical segment solutions are no longer feasible, and a numerical approach becomes necessary. One possibility is the development of a finite element solution of the BHE [204,205]. However, the most common approach is to use a finite difference scheme, which will be discussed in some detail in the following. One of the main reasons for preferring a finite difference solution, besides its computational efficiency, is that it allows a very simple link with the FDTD method, which is the most popular numerical method for SAR computations. Earlier finite difference solutions of the BHE, used in conjunction with cubic-cell models of the human body, comprised only a few hundred voxels. They used an implicit formulation to avoid the restrictions on the size of the time step. Since these solutions required matrix inversions, they were computationally intensive [16]. As more detailed body models, comprising thousands of voxels, became available, new finite difference solutions were developed. These techniques, based either on explicit or on alternate direction implicit (ADI) formulations, are discussed in the following.

10.5.4.1 Explicit Finite Difference Formulation

One approach to obtain a finite difference explicit formulation of the BHE is based on the thermal balance approach [98]. The body under consideration is divided into cubic cells of

side δ, and the temperature is evaluated at the center of each cell. Temperatures are computed at equal-time steps, δt. In the following, the expression $T^n(i,j,k)$ represents temperature computed at time $n\delta t$ in the (i,j,k) cell. The finite difference formulation is derived by imposing the thermal balance to each cell [192], such that

$$Q_{\text{tot}}^{n,n+1}(i,j,k) = \Gamma(T^{n+1}(i,j,k) - T^n(i,j,k))(\text{J}) \tag{10.41}$$

where $Q_{\text{tot}}^{n,n+1}$ is the total heat accumulated (positive) or lost (negative) in the cell during the time interval $[n\delta t - (n+1)\delta t]$, $(T^{n+1} - T^n)$ is the variation of the cell temperature in the same time interval, and $\Gamma = C\rho\delta^3$ is the thermal capacitance of the cell. The heat $Q_{\text{tot}}^{n,n+1}$ is accumulated (or lost) in the cell through the five mechanisms present in the BHE, and, for boundary cells, also through convection to external air and sweating (Equation 10.30).

Heat transfer through internal conduction is governed by Fourier's law. For the (i,j,k) cell, the heat $Q_{\text{K}}^{n,n+1}$ entering the cell through conduction from the $(i-1,j,k)$ cell in the time interval $[n\delta t - (n+1)\delta t]$ can be derived by exploiting the well-known analogy between heat conduction and electrical current conduction [185,192]. In particular, if K_1 and K_2 are the thermal conductivities of the two cells under examination, heat flows through the series connection of two thermal conductances, equaling $K_1\delta^2/(\delta/2)$ and $K_2\delta^2/(\delta/2)$, respectively. Therefore, heat flowing from the center of the $(i-1,j,k)$ cell to the center of the (i,j,k) cell, through the boundary face, experiences an overall thermal conductance equal to $2K_1K_2\delta^2/((K_1+K_2)\delta)$. As a result, we obtain:

$$Q_K^{n,n+1}(i,j,k) = \frac{2K_1K_2}{K_1+K_2}\delta^2\frac{T^n(i-1,j,k) - T^n(i,j,k)}{\delta}\delta t \tag{10.42}$$

An expression similar to Equation 10.42 holds for heat exchanged with the other neighboring cells.

The contributions of metabolic heat production and electromagnetic power deposition are volumetric heat sources, and therefore the contribution they give to $Q_{\text{tot}}^{n,n+1}$ can be immediately derived and is expressed by Equation 10.43 and Equation 10.44, respectively:

$$Q_A^{n,n+1}(i,j,k) = A(i,j,k)\delta^3\delta t \tag{10.43}$$

$$Q_{Q_v}^{n,n+1}(i,j,k) = Q_v(i,j,k)\delta^3\delta t \tag{10.44}$$

Respiratory losses in the lungs are taken into account by subtracting the volumetric loss R_L from the metabolic heat production A in the corresponding cells for the lung.

Finally, the contribution to $Q_{\text{tot}}^{n,n+1}$ due to capillary blood perfusion takes the form of a volumetric term and can be represented, as in metabolic heat production and exogenous heat deposition, as:

$$Q_B^{n,n+1}(i,j,k) = B(i,j,k)((T_B - T^n(i,j,k))\delta^3\delta t \tag{10.45}$$

For boundary cells in contact with air, heat flow through the face is governed by convection rather than conduction. For a generic cell (i,j,k), considering a face in direct contact with air, the heat $Q_{\text{H}}^{n,n+1}$ entering the cell through convection in the time interval $[n\delta t - (n+1)\delta t]$ is:

$$Q_H^{n,n+1}(i,j,k) = H(T_A - T^n(i,j,k))\delta^2\delta t \tag{10.46}$$

Heat losses due to sweating at the skin surface (SW) are converted to a volumetric heat loss term and are directly subtracted from the metabolic heat production term A in the skin cells.

Note that in Equation 10.42, Equation 10.45, and Equation 10.46, the temperature has been referred to the time instant $n\delta t$ in order to obtain, at the end, an explicit formulation. Starting from the equations given above, general explicit formulations that hold for each cell can be derived. (See the paper by Bernardi et al. [98] for additional details)

10.5.4.1.1 Stability Criterion

Explicit finite difference formulations are straightforward to implement and are computationally efficient, but they have a limitation on the maximum time step δt that can be used without incurring numerical instability.

The stability criterion for the previously mentioned finite difference scheme can be obtained through Fourier's analysis, which yields the following restriction on δt, derived for internal cells (no convective contributions) [206]:

$$\delta t \leq \frac{1}{6(K/C\rho\delta^2) + (B_0/2C\rho)} \tag{10.47}$$

Because of the typical values of thermal parameters and convection coefficients for the human body, the stability criterion for the peripheral voxels, where some of the faces exchange heat through convection rather than conduction, is less stringent than that of Equation 10.47. Consequently, Equation 10.47 may be safely assumed as the stability criterion for the overall scheme.

10.5.4.2 ADI Formulation

While the explicit finite difference formulation of the BHE has been applied to many simulations, it becomes computationally unaffordable when very small cell sizes are used or when high thermal conductivity materials are present in the domain under study. This stems from the extremely small time steps δt that would be required according to Equation 10.47. In such cases, the ADI formulations can be used [207]. ADI is a general method, developed for numerical solution of parabolic equations. It combines unconditional stability, typical of implicit methods, with the computational efficiency due to the tri-diagonal nature of the resulting matrices [208–210]. Note that the Fourier heat conduction equation is a typical parabolic equation. While the BHE is no longer parabolic, because of the presence of the term related to blood flow, ADI can still be applied, but it loses its unconditional stability. In any case, for time steps on the order of a few seconds, the scheme has proved to be stable in typical applications. It can yield reductions on the order of tenfold or more [207] in execution time, over the classical explicit formulation.

The basic idea behind the ADI technique is to extend to the 3-D case the 1-D Crank–Nicolson's scheme, which averages the outcome from the explicit and the implicit formulations to obtain second-order accuracy both in space and in time variables [192]. In particular, Crank–Nicolson's scheme can be extended to the full 3-D case, by using a sequence of approximate Crank–Nicolson solutions along the three axes, indicated as $T^*(i,j,k)$, $T^{**}(i,j,k)$, and $T^{***}(i,j,k)$, the last one being used as the final estimate for $T^{n+1}(i,j,k)$.

The first approximate solution is obtained using Crank–Nicolson's scheme along the x axis only, while backward differencing is used along y and z:

$$\frac{K}{\rho C}\frac{1}{2}\left(\frac{T^*(i-1,j,k)-2T^*(i,j,k)+T^*(i+1,j,k)}{(\delta x)^2}+\frac{T^n(i-1,j,k)-2T^n(i,j,k)+T^n(i+1,j,k)}{(\delta x)^2}\right)$$
$$+\frac{K}{\rho C}\frac{T^n(i,j-1,k)-2T^n(i,j,k)+T^n(i,j+1,k)}{(\delta y)^2}$$
$$+\frac{K}{\rho C}\frac{T^n(i,j,k-1)-2T^n(i,j,k)+T^n(i,j,k+1)}{(\delta z)^2}$$
$$=\frac{T^*(i,j,k)-T^n(i,j,k)}{\delta t}-\frac{A_0+Q_v+B_0T_B}{\rho C}$$
$$+\frac{B_0}{\rho C}\frac{T^*(i,j,k)+T^n(i,j,k)}{2} \tag{10.48}$$

Extending subsequently Crank–Nicolson's solution along the y axis and the z axis, the following expressions are obtained for the second and third estimates:

$$\frac{K}{\rho C}\frac{1}{2}\left(\frac{T^*(i-1,j,k)-2T^*(i,j,k)+T^*(i+1,j,k)}{(\delta x)^2}+\frac{T^n(i-1,j,k)-2T^n(i,j,k)+T^n(i+1,j,k)}{(\delta x)^2}\right)$$
$$+\frac{K}{\rho C}\frac{1}{2}\left(\frac{T^{**}(i,j-1,k)-2T^{**}(i,j,k)+T^{**}(i,j+1,k)}{(\delta y)^2}+\frac{T^n(i,j-1,k)-2T^n(i,j,k)+T^n(i,j+1,k)}{(\delta y)^2}\right)$$
$$+\frac{K}{\rho C}\frac{T^n(i,j,k-1)-2T^n(i,j,k)+T^n(i,j,k+1)}{(\delta z)^2}$$
$$=\frac{T^{**}(i,j,k)-T^n(i,j,k)}{\delta t}-\frac{A_0+Q_v+B_0T_B}{\rho C}$$
$$+\frac{B}{\rho C}\frac{T^{**}(i,j,k)+T^n(i,j,k)}{2} \tag{10.49}$$

$$\frac{K}{\rho C}\frac{1}{2}\left(\frac{T^*(i-1,j,k)-2T^*(i,j,k)+T^*(i+1,j,k)}{(\delta x)^2}+\frac{T^n(i-1,j,k)-2T^n(i,j,k)+T^n(i+1,j,k)}{(\delta x)^2}\right)$$
$$+\frac{K}{\rho C}\frac{1}{2}\left(\frac{T^{**}(i,j-1,k)-2T^{**}(i,j,k)+T^{**}(i,j+1,k)}{(\delta y)^2}+\frac{T^n(i,j-1,k)-2T^n(i,j,k)+T^n(i,j+1,k)}{(\delta y)^2}\right)$$
$$+\frac{K}{\rho C}\frac{1}{2}\left(\frac{T^{n+1}(i,j,k-1)-2T^{n+1}(i,j,k)+T^{n+1}(i,j,k+1)}{(\delta z)^2}+\frac{T^n(i,j,k-1)-2T^n(i,j,k)+T^n(i,j,k+1)}{(\delta z)^2}\right)$$
$$=\frac{T^{n+1}(i,j,k)-T^n(i,j,k)}{\delta t}-\frac{A_0+Q_v+B_0T_B}{\rho C}$$
$$+\frac{B_0}{\rho C}\frac{T^{n+1}(i,j,k)+T^n(i,j,k)}{2} \tag{10.50}$$

Starting from the above expressions, it is possible to derive the general ADI formulation that holds for each internal cell. (See the paper by Pisa et al. [207] for additional details.) The formulation can also be adapted to boundary cells, where convective heat exchange must be considered, by introducing a fictitious external node.

10.5.5 Temperature Elevations in Subjects Exposed to EM Fields

When an EM field impinges on the biological body, a fraction of the incident power is absorbed by the body and is converted into heat in the body tissue. Thus, the absorbed energy can cause temperature increases in various body organs and tissues. If the temperature increase is small, it has little effect and is controlled by the thermoregulatory mechanisms of the body. However, if the temperature increment is large, it can produce irreversible biological damage. For example, a temperature increase of about 4.5°C for more than 30 min would produce neuronal damage [211]. Experiments performed on the rabbit eye indicated that a threshold increase of 3°C to 5°C in the lens can induce cataract formation [212,213]. The temperature increase necessary to induce thermal damage to the skin is about 10°C [214,215], while it is 8°C for muscle tissues [216]. Also, experiments performed using laboratory animals have shown various physiological and behavioral effects when the body core temperature rises more than 1°C to 2°C [100]. (See also Chapter 5 by Black [285].)

Moreover, most RF protection standards have adopted basic restrictions in order to keep the thermal increments below some agreed upon level. In particular, the value of 4 W/kg averaged over the whole body (SAR_{WB}) had been adopted by exposure guidelines as the threshold for the induction of adverse thermal effects associated with an increase of the body core temperature of about 1°C in animal experiments. Restrictions on local SAR were introduced in order to limit local temperature increments, since the ratio of the local peak to whole-body averaged SAR can be as high as 20:1 for exposure to a uniform plane wave [217]. However, it is important to note that tissue heating during EM exposure is strongly influenced not only by the power dissipated in the local tissue volume, but also by the way in which absorption is distributed in the surrounding area, by the thermal characteristics of the tissue and its neighbors, and, finally, by the heat exchange with the external environment. The correlation between local SAR values and temperature increases and between SAR and temperature distributions is not straightforward. There have been many studies dealing with thermal increments due to exposures both to the far field of radiating sources and to the near field of cellular phones. In the following some of these studies will be summarized and discussed.

10.5.5.1 Temperature Increments in the Human Body Exposed to the Far Field of Radiating RF Sources

In the past, temperature elevations due to EM power absorption in the human body have been evaluated using several models. The earlier studies were based on a simplified cylindrical segment approximation of the human body [183,184,202,203]. In these studies, the thermal behavior of the human body was simulated by means of two systems: a controlling system and a controlled one. The controlled system, modeled by the BHE, determines the temperature distribution inside the body, while the controlling system provides feedback signals able to modify the thermal parameters of the controlled one in order to maintain a constant body core temperature (thermoregulation). These studies are limited to modeling the body as few homogenous cylindrical segments, each one having a uniform SAR and temperature distribution. A subsequent study [197] used a cubic-cell model with tissue inhomogeneity and took into account the thermoregulatory mechanisms in the BHE. In this case, the BHE was solved using an implicit formulation, which

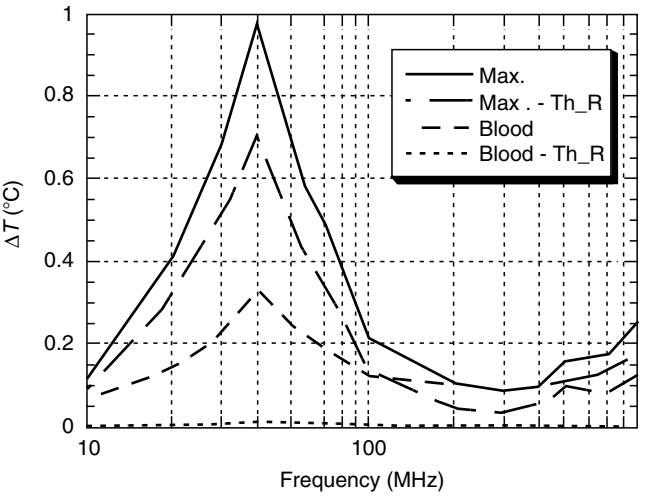

FIGURE 10.27
Maximum temperature increases (ΔT) in the body and blood of a subject wearing shoes, as a function of frequency, with or without thermoregulation (Th_R) for a P_{inc} equal to the limits set by ICNIRP [101].

avoided the restriction in the size of the time step. The explicit formulation requires a computationally intensive matrix inversion. Lately, explicit formulations of the BHE have been developed to study thermal responses in anatomically accurate body models [196,218,219]. In most of these studies, only limited body regions were considered, and thermoregulation mechanisms were neglected.

More recently, the electromagnetic and thermal problems have been combined in a detailed anatomical model of the human body (5-mm resolution) [98]. The FDTD method was used to compute the EMF distribution inside the exposed body, while an explicit finite difference formulation of the BHE, together with an accurate model of the human thermoregulatory system, were developed to compute the corresponding temperature increase.

For an incident power density equal to the maximum permissible value in the International Commission on Non-Ionizing Radiation Protection (ICNIRP) exposure guidelines for the general public [101], Figure 10.27 shows the maximum temperature increase ΔT_{max} obtained inside the body and in the blood as a function of frequency for a subject wearing shoes, both with and without thermoregulation [98]. It can be seen that the highest ΔT values are obtained at 40 MHz. It is also interesting to note that when thermoregulation is considered, the increase in blood temperature is practically zero, while the maximum temperature rise in the body can reach 0.72°C. This happens since blood temperature is very close to the body core temperature, which thermoregulation tends to keep as constant, while the maximum temperature increments are usually found in the superficial tissue layers.

It is worth noting that at 40 MHz, the maximum temperature increase (i.e., 0.72°C in the presence of thermoregulation) is found in the muscle tissues of the ankle. The threshold for the induction of thermal damage in muscle is about 45°C [216], which corresponds to a temperature increase of about 8°C. This temperature differential coincides with the safety factor of 10 promulgated by ICNIRP [100] for occupational exposure in limiting the power density from inducing a thermal effect. Moreover, a safety factor of 50 can be deduced from the temperature increase obtained at 10 MHz and in the frequency range between 100 and 900 MHz, where the maximum temperature increases are less than 0.16°C.

Figure 10.28 shows the distribution of the maximum temperature increase for each horizontal layer of the body at 40 MHz (a) and 900 MHz (b), for an incident power density of 1 mW/cm.^{2} At 40 MHz, the maximum temperature increases are obtained at the level

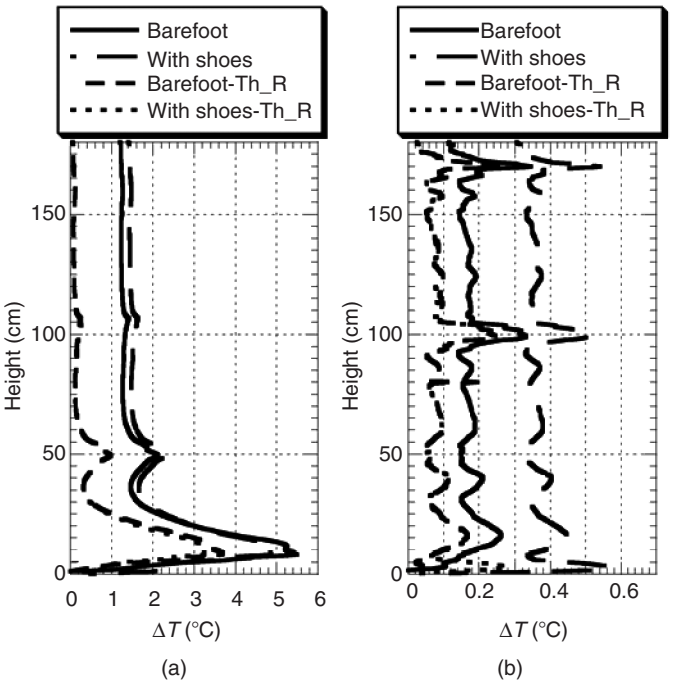

FIGURE 10.28
Layer peak temperature increase (ΔT) in the absence or presence of thermoregulation (Th_R) for a grounded subject barefoot or with shoes ($P_{inc} = 1\,mW/cm^2$). (a) $f = 40\,MHz$ and (b) $f = 900\,MHz$.

of the ankles, where the maximum local SARs also are located. The result showed that the presence of the shoes could influence temperature change. Since shoes are isolators from the thermal point of view, they prevent heat flow from going to the ground through them and provoking higher heating within the body. The only exception is in the ankle section, where heating was higher in the barefoot model because of the higher SAR values, at 40 MHz.

Also, the presence of the thermoregulatory mechanisms reduced the temperature increase almost uniformly along the body. Figure 10.28 illustrates clearly the role of blood convection in heat exchanges. In fact, even without active thermoregulation, heat could be spread from the point where its deposition is relatively high (e.g., the ankle at 40 MHz) to the rest of the body, by an increase in the temperature of the circulating blood. Therefore, even if power absorption is limited to one body region, temperature elevations may occur throughout the body. This is clearly visible at 40 MHz, where, although power absorption is mainly confined to the ankle region, in the absence of thermoregulation significant temperature elevations (about 1.4°C, $P_{inc} = 1.0\,mW/cm^2$—see Figure 10.28a) can be observed in the brain. The corresponding elevation in blood temperature elevation is about 1.46°C. It is interesting to note that at 900 MHz, in the absence of active thermoregulation, the brain temperature elevation (0.5°C, $P_{inc} = 1.0\,mW/cm^2$—see Figure 10.28b) is higher than blood temperature elevation (0.35°C), as a result of power deposition inside the brain.

10.5.5.2 Temperature Increments in the Head of a Cellular Telephone User

One consequence of RF power absorption in the human head exposed to the field emitted by a cellular phone is temperature increase in the head. In practical situations, in addition to RF power deposition, there are two other causes for temperature increase. The first one is the contact between the phone case and the user's head (ear and cheek, in particular), which blocks the convective heat exchange between the skin layers and the air. It causes

the temperature to rise in tissues around the contact zone. Obviously, this heating is independent of the radiated power, and indeed it was observed also for a wired phone. The second cause for temperature increase is the heating of the phone itself, because of the power dissipated in the internal circuitry, especially the power amplifier. This heating is transferred to the head tissues via thermal conduction.

Studies on temperature rises in the human head, associated with the field emitted by the cell phone, are usually conducted by using anatomically based head models, a numerical solution of the electromagnetic problem, and finite difference formulations of the BHE [161,164,172,187,220–223]. For example, the dissipation in the power amplifier was simulated by adding a power deposition of 250 mW at 900 MHz and 125 mW at 1800 MHz, uniformly distributed inside the upper part of the phone with a 50% efficiency [161]. The heating effects due to SAR, phone contact, and power dissipation in the amplifier were considered separately and were subsequently added together in order to obtain the temperature elevation. The maximum temperature elevations obtained in the ear and in the brain of a user's head are given in Table 10.12 for 900 and 1800 MHz. The ambient air temperature was assumed to be 24°C and a time interval of 15 min, approximating the duration of a long phone call. Although a steady state would not have been reached, the temperature elevation after 15 min is expected to be very close to the steady-state value [164].

The data shown in Table 10.12 reveal some interesting aspects. First, the temperature elevation induced inside the brain by SAR alone was less than 0.1°C, especially when the phone was kept in the ''cheek'' position. This configuration resulted in a marked reduction in power deposition inside the brain. Table 10.12 also shows that the mere contact of the cellular phone with the ear and cheek, even in a standby mode, in which no RF power is radiated, can cause a temperature elevation in the ear reaching as high as 1.5°C. This is due to the highly insulating properties assumed for the phone plastic shell. A negligible maximum temperature elevation of about 0.01°C, instead, is obtained in the external brain region. If the contribution from power dissipation in the amplifier is included, the induced temperature elevations are not significantly altered. It must be noted, however, that this result arises from consideration of power dissipation in the power amplifier alone. In the real situation, additional power dissipation is present in the internal circuitry of the handset, besides the power amplifier, and hence slightly higher temperature elevations may be observed [221].

Note: Results are for visible human (VH) adult, isotropically reduced child size (CS), and anisotropically reduced child-like (CL) numerical phantoms.

TABLE 10.12

Temperature Elevations Induced in the User's Head, after 15 min, by a Phone Equipped with a Dual-Band Monopole-Helix Antenna (Average Radiated Power: 250 mW at 900 MHz and 125 mW at 1800 MHz)

Frequency (MHz)	Position	Heating Cause	ΔT_{max} (°C)	$\Delta T_{maxbrain}$ (°C)
900	Vertical	SAR	0.221	0.061
	Cheek	SAR	0.136	0.023[a]
		Contact	1.543	0.012[b]
		Contact + power dissipation	1.544	0.012[b]
		Contact + power dissipation + SAR	1.581	0.023[a]
1800	Vertical	SAR	0.155	0.036
	Cheek	SAR	0.085	0.011[a]
		Contact	1.543	0.012[b]
		Contact + power dissipation	1.543	0.012[b]
		Contact + power dissipation	1.549	0.012[b]

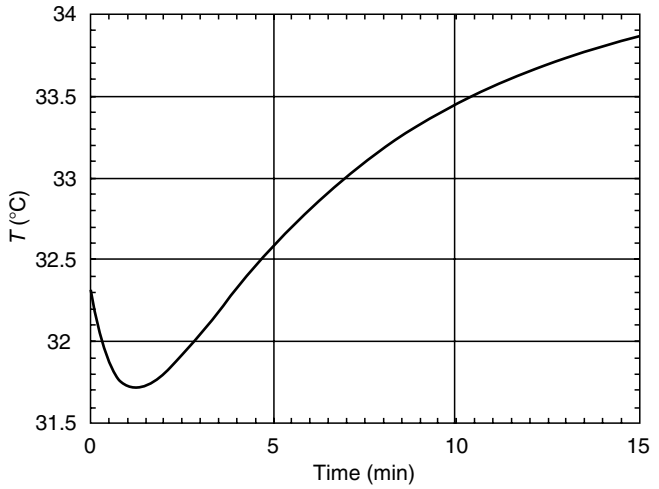

FIGURE 10.29
Time evolution of the temperature at a point on the ear in direct contact with a nonradiating phone.

The effect of the phone contact on the temperature evolution in the ear region is shown in Figure 10.29. It can be seen that when the phone was put in contact with the ear, the ear temperature experienced a quick decrease. This is because the phone was initially at ambient temperature (24°C), which was lower than the ear temperature. However, soon afterward, the heat supplied by the blood and conducted from the neighboring tissues stopped the decrease. Indeed, the temperature started to elevate, going beyond the initial value, because of the suppressed convective exchange with air.

When all heating sources are considered simultaneously, the results indicate that the maximum temperature elevation in the ear was almost entirely due to the contact effect, with only a very slight contribution due to SAR deposition in the ear region. However, the situation was completely different in the brain region. In fact, the heating effects due to SAR and phone contact tend to heat different parts of the brain. The contact-effect heating occurred in the lower external brain region, and the SAR-induced heating appeared mostly in the upper external brain region. Therefore, these two heating effects are not additive in the brain, and when they are simultaneously present, as opposed to the case when only one is considered, the result is that the portion of the brain affected by heating becomes larger. The peak temperature increase in the brain is therefore governed by the more significant of the two heating causes. At 900 MHz, SAR is more dominant, while at 1800 MHz, because of the lower radiated power, the two heating effects are comparable. Note that the ANSI/IEEE safety guidelines, which restrict the 1-g averaged spatial peak SAR to 1.6 W/kg, are associated with maximum temperature rises in the brain between 0.03°C and 0.09°C. These values are about 50 times lower than the threshold for thermal damage. The ICNIRP safety guideline of a 10-g averaged spatial peak SAR equal to 2 W/kg, results in maximum temperature rises in the brain between 0.1°C and 0.2°C, which is about 25 times lower than the threshold value.

10.6 Thermal Therapeutic Applications of Microwave Energy

Recent advances in technological development and in the understanding of EMF interaction with biological materials and systems have launched a broad range of biomedical applications. The following is a brief overview of computational techniques involved in

the development of ablative and hyperthermia therapies, including microwave cardiac ablation, endometrial ablation, and hyperthermia treatment of cancer. All of these therapeutic applications involve the use of microwave technologies to produce localized depositions of electromagnetic energy and, as a result, a rise of the local temperature in biological tissues. The target tissue temperature for the ablative treatments is about 65°C [224,225], whereas for the hyperthermia treatments, it is about 43°C [226]. The ablation treatments include the treatment for cardiac arrhythmias and for endometrial disorders such as menorrhagia. In all cases, the distribution of temperature increase must be carefully controlled in order to avoid excessive temperature increase in the surrounding healthy tissue. (See also Chapter 12 by Chou [284].)

10.6.1 Ablation for Cardiac Arrhythmias

Cardiac arrhythmias are mainly due to the presence of abnormal electrical sources or current paths in the cardiac tissues and are usually treated by destroying the tissue substrate where the electrical anomaly is localized [227–230]. This was performed by surgical resection initially, and later on by delivering a high-intensity DC shock with a defibrillator [227,230]. However, the high voltages and currents associated with the DC shock resulted in uncontrollable cardiac damages and severe complications. Subsequently, the use of RF EMFs to heat and destroy the arrhythmic tissue was proposed [230], and the advantages of microwave technology were demonstrated [228,229].

The RF ablation of cardiac tissue is usually performed using a unipolar arrangement, in which a catheter electrode placed into the heart delivers RF current to a large dispersive ground electrode on the skin surface of the patient. The RF current that flows from the catheter to the ground electrode following radial paths generates heat. While flowing from the catheter, the RF current density decreases as the second power of distance; consequently, the heat generation decreases according to the fourth-power law with the distance from the electrode. With this arrangement, the lesion (ablated tissue) is restricted to a small region (usually about 2 to 3 mm in diameter) contiguous to the catheter electrode, and the lesion dimensions cannot be extended by increasing the delivered power [225,227,229–231]. In microwave ablation, a catheter antenna is inserted into the cardiac chamber and is used to deliver MW power [225,228]. Since MW power deposition inside tissue decays with distance by following a second-power law, deeper lesions can be obtained compared to RF ablation [229,232–234].

In cardiac ablation treatments the lesion is usually defined as the region where temperature exceeds 65°C, which represents the threshold for irreversible damage of this tissue. This region must be large enough to ablate all the abnormal tissue responsible for the arrhythmia. Catheter antennas used for MW ablation have included monopoles [235,236], dipoles [229,237,238], and helices [232,239]. The design of a MW catheter antenna is a crucial point in MW ablation treatments and requires a complete study of the performance of the antenna imbedded in blood and in contact with the cardiac tissue. Performance parameters usually analyzed include the radiation pattern in the tissue; antenna impedance, which governs the bandwidth of the antenna; surface current suppression, in order to prevent heating of tissue along the catheter feeding cable; and dimensions of the induced lesion [240,241].

The design and performance evaluation of the microwave ablation antennas can be conducted by using computational tools and tested through *in vitro* or *in vivo* experimental studies [229,233,238,242]. Numerical tools allow the analysis of antenna performances under different operating conditions, and the evaluation of both electromagnetic power deposition and temperature increase in the tissue. In particular, the numerical evaluation of temperature increase induced inside the cardiac tissue allows the evaluation of blood flow influence on the induced lesion. This evaluation is of fundamental importance since the

D = 2.4 mm, D_1 = 1.4 mm, D_2 = 0.87 mm, D_3 = 0.3 mm

L_1 = 3 mm, L_2 = 0.5 mm, L_3 = 1.5 mm, L_4 = 1 mm

FIGURE 10.30
The cap-choke microwave catheter antenna.

presence of high blood flow rates inside the heart chambers provides a very effective heat removal process at the heart tissue surface so that the blood flow strongly limits the efficiency of both RF and MW ablation systems. Several numerical studies of SAR and temperature increase have been performed with the FEM [236,243–245] as well as the FDTD [246].

Figure 10.30 shows a cap-choke antenna mounted on an RG/178BU flexible coaxial cable operating at 2450 MHz [238]. The structure was realized by connecting an annular cap to the inner conductor of the cable, and a cylindrical coaxial choke to the outer conductor. A junction, filled with high-temperature epoxy resin, was used to separate the cap from the choke. Figure 10.31 shows the same antenna inserted in a two-layer cylindrical model of the heart. The heart model was used to study the influence of antenna position (touching or pressed into the cardiac muscle) and of blood flow (high or low) on the induced lesion. As an example, some computed results are presented in Table 10.13 for the amount of power to be delivered to the cardiac tissue to obtain lesions of different depths, under four operating conditions for an exposure duration of 60 sec [246].

10.6.2 Ablation for Endometrial Disorders

While still in the beginning stage, microwave and RF thermal ablation of the endometrium have been suggested recently as efficient and cost-effective alternatives to surgical resection as a treatment for dysfunctional uterine bleeding [247–251]. Techniques presently in

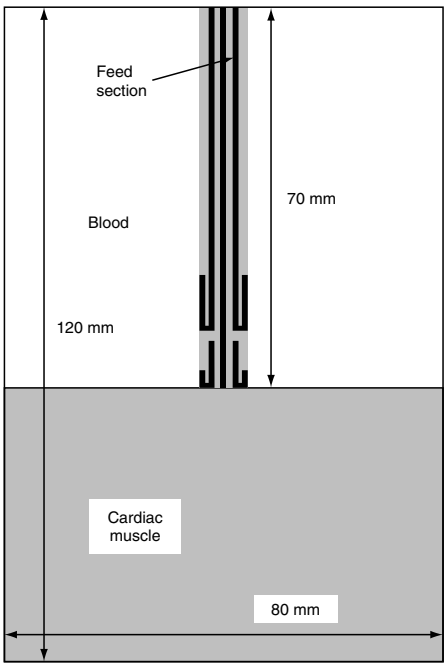

FIGURE 10.31
Cross section of the two-layer numerical model. The antenna's radial dimensions are not in scale.

[a] $\Delta T_{maxbrain}$ located in the upper external brain region.
[b] $\Delta T_{maxBRAIN}$ located in the lower external brain region.

TABLE 10.13

Microwave Power Required to Produce a Given Lesion Depth for Different Operating Conditions (Exposure Duration: 60 sec)

	Power (W)			
Lesion Depth (mm)	**Touch Low Perfusion**	**Touch High Perfusion**	**Pressed Low Perfusion**	**Pressed High Perfusion**
1	2.5	4.0	2.0	2.5
3	6.2	10	5.0	6.2

use include electrosurgery resection and Nd:YAG laser coagulation under direct hysteroscopic visualization [247,248,252–256]. The reported rates of complete amenorrhea are between 25% and 70% [253,256]. The variability arises principally from the unpredictable nature of induced thermal injury and perforation of the uterine wall [253]. Quantitative measures and patients' subjective reports of microwave endometrial ablation suggest a higher rate of satisfaction, acceptability, and life quality improvement [257,258].

In endometrial ablation, as in cardiac ablation, the design of the catheter antenna should be carefully tested to ensure the desired temperature increase (up to an increase of about 40°C in this case) in the tissue of interest. A sleeved-slot antenna designed for endometrial ablation operation at 915 MHz is depicted in Figure 10.32. The antenna configuration is similar to that of the catheter antenna for cardiac ablation, and is mounted on an RG8U coaxial cable. Figure 10.33 shows a comparison of the axial SAR distribution obtained from an FDTD analysis and from temperature measurements made in a cylindrical phantom filled with a muscle-equivalent material [259]. Two radial distances from the antenna axis, 2.5 and 7.5 mm, are shown. The SAR data obtained experimentally were normalized to the ones obtained from the FDTD simulation with 1.0 W of radiated power.

Figure 10.34 presents the lesion depth, defined as the region around the antenna where the temperature increase was greater or equal to 38°C (final temperature 75°C), as a function of the time of the exposure at different radiated powers. The curves were obtained by considering an antenna inserted in a cylindrical phantom filled with muscle-equivalent material. They simulate an antenna touching the endometrial tissue to be ablated. The lesion dimensions were evaluated as the depth from the antenna outer conductor. These curves can serve as guides in clinical trials where the antenna feeding power and time of exposure are key parameters to be chosen for a desired lesion dimension.

10.6.3 Microwave Interstitial Hyperthermia for Cancer Treatment

Hyperthermia cancer therapy is a treatment procedure in which tumor temperatures are elevated to above 43°C [226]. Investigations performed on cell cultures, tumor-bearing animals, and human patients have clearly shown that hyperthermia affords preferential

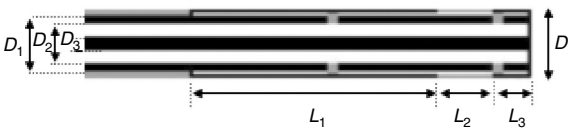

D = 12 mm, D_1 = 9.8 mm, D_2 = 7 mm, D_3 = 2.6 mm
L_1 = 45 mm, L_2 = 10 mm, L_3 = 7 mm,

FIGURE 10.32
A microwave catheter antenna for endometrial ablation.

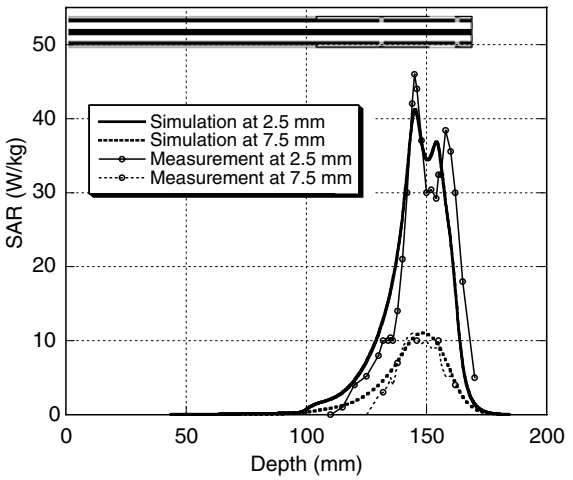

FIGURE 10.33
Comparison of axial SAR distributions obtained from FDTD and from temperature measurements made in tissue phantoms for the endometrial sleeved-slot antenna. The data are shown for radial distances of 2.5 and 7.5 mm.

killing of malignant cells, enhances the cytotoxic effects of many anticancer drugs, and potentiates the cell-killing ability of ionizing irradiation [260–266].

An important aspect of the development of applicators for microwave hyperthermia is the production of required temperature distributions in superficial and deep-seated tumors, that is, to produce temperatures in excess of 43°C in the tumor tissue, in order to guarantee the destruction of the malignant cells, while maintaining the temperature in the healthy tissue below 42°C to avoid thermal damage. In microwave hyperthermia, the antenna must provide efficient power delivery, good impedance matching at the frequency of operation, and a uniform SAR distribution in the tumor region. However, if the region to be treated is large compared to the field penetration depth, the required SAR uniformity cannot be achieved with a single microwave antenna, and the use of antenna

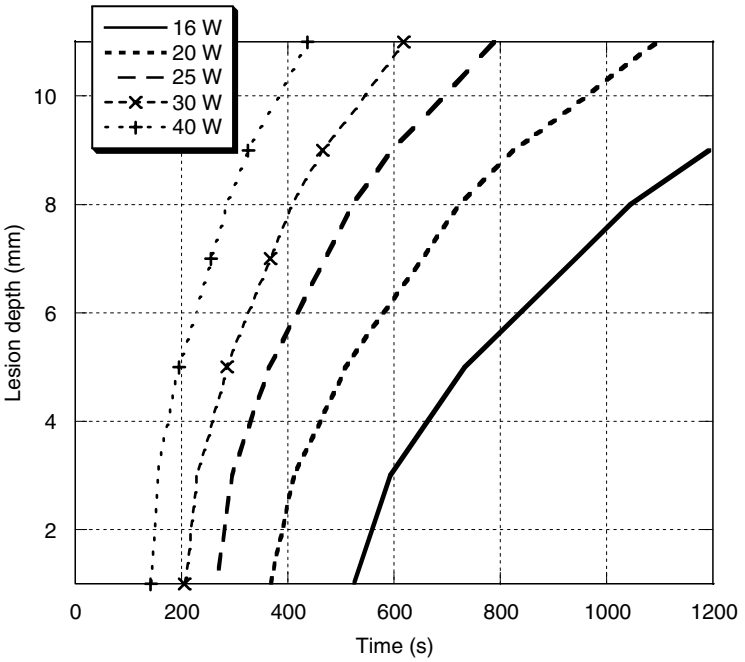

FIGURE 10.34
Endometrial lesion depth as a function of exposure duration for different radiated powers.

arrays becomes necessary. The following paragraphs present some computational results for thin catheter antennas designed for interstitial hyperthermia treatment of brain tumors.

Many investigations have been conducted on electromagnetic power deposition with regard to hyperthermia treatment for cancer. Most earlier studies were conducted analytically, modeling the catheter dipole antenna and surrounding tissue with a lossy transmission line [267–270]. Later, numerical and experimental studies were conducted on several antenna types, with the aim of optimizing antenna performances [270–274]. Considerable attention was devoted to arrays of antennas that have been studied both experimentally [275–277], by measuring the rate of temperature change caused by the radiated power, and theoretically, using antenna theory approaches [275,276,278] or approximate numerical procedures [277,279]. Indeed, antenna arrays have proved to be more suitable for increasing the region of uniform SAR deposition. More recent studies calculated, besides the electromagnetic power deposition, also the corresponding temperature increase. In fact, thermal analysis is a fundamental step in evaluating the effectiveness of the microwave applicator since it allows the assessment of the region where the temperature is above the threshold, and estimation of the required input power. Temperature distributions produced by interstitial antennas in tumor tissues have been experimentally evaluated by using microwave radiometry [277] and computed by using finite difference explicit solutions of the BHE [280,281]. A numerical solution of the BHE allows the analysis of the influence of different parameters such as blood flow on the temperature increase [280] and the development of clinical protocols [281].

Recently, an ADI solution of the BHE has been developed to study a 3-D array of catheter antennas inserted into a brain-equivalent phantom [282]. The antenna considered (Figure 10.35) was a sleeved-slot antenna mounted on a UT-34 coaxial cable [259,283]. An equilateral triangular array of the sleeved-slot antennas was studied in a phantom of brain-equivalent tissue in order to assess its capability in heating tumor regions of various dimensions [282]. Figure 10.36a shows the SAR distribution for 15-mm spacing among the antennas in the array; while in Figure 10.36b, contour plots at $\Delta T = 6^{\circ}\mathrm{C}$ for various radiated powers and for a 15-mm spacing are presented. The graphs shown in Figure 10.36a and b are for a horizontal plane passing through the antenna slot [282].

Results such as those in Figure 10.36 can provide guidance to clinical protocols regarding the input power and optimal geometry (array spacing) for achieving an efficient tumor heating. For example, there is a minimum input power below which three separated regions around the three interstitial antennas constitute the region with temperatures above 43°C. Once this power is exceeded, a simply connected domain is obtained.

It is interesting to note that blood flow is remarkably low in the necrotic core of tumor tissues compared to normal tissue. Moreover, the rate of blood flow in normal tissue increases during hyperthermia. These phenomena may be investigated by varying the blood perfusion parameter in the BHE. Computer simulations, performed by varying the blood perfusion parameter from 5% to 200% of the nominal value, showed that the heat removal mechanism becomes less efficient as the blood flow is decreased, and the effective region of hyperthermia therapy is enlarged [282]. Consequently, the reduced blood flow in the necrotic tumor core and the increase in blood flow in normal tissue can serve to facilitate hyperthermia therapy.

10.7 Concluding Remarks

Knowledge of internal electric and magnetic fields, induced current densities, and SARs is fundamental in the study of biological responses, health effects, and medical applications

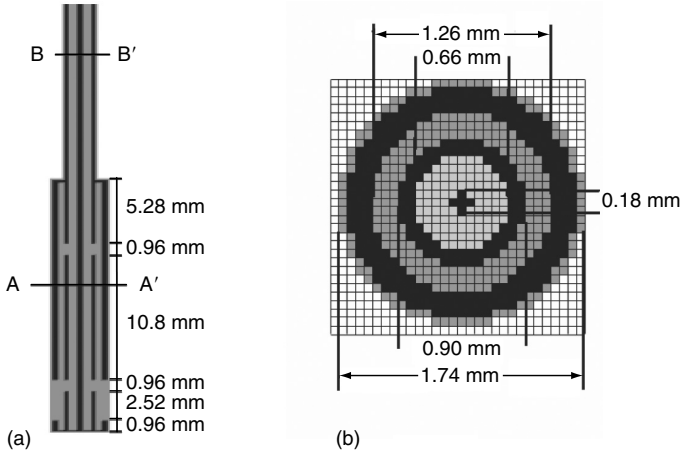

FIGURE 10.35
Longitudinal (a) and horizontal AA′ (b) sections of the sleeved-slot antenna.

of EMFs. Complexities of biological tissues and of the incident fields make closed-form analytical solutions impractical, and computer methods are needed to predict the internal fields and their distributions. Great strides have been made during the past decade in the area of numerical dosimetry using anatomically based models of the human body. Among the most valuable of the numerical methods for predicting field intensities and SAR calculations are the impedance method for use at lower frequencies, where quasi-static approximations may be made ($<\sim$40 MHz for the human body), and the FEM and FDTD methods, which may be used at any frequency of interest. For numerical calculations, the FDTD method requires a computer memory and computation time that is proportional to N. This is a considerable advantage over the computing methods, such as MoM or MoM–FFT. This chapter described the salient features of these methods and the many bioelectromagnetic exposure conditions for which they have been applied. Because of the limitations on the length of the chapter, only a few of the important recent applications of some of these methods were presented in some detail.

Note that numerical methods have matured to a level that they are being increasingly used by researchers in many laboratories for dosimetric calculations for important and

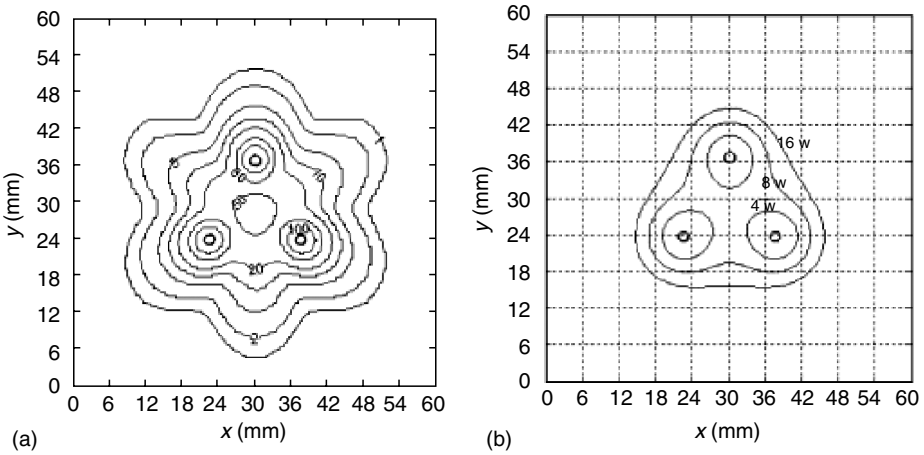

FIGURE 10.36
SAR distribution (a) and contour plots at $\Delta T = 6^{\circ}$C for various radiated powers (b), on a horizontal plane passing through the antenna slot, for 15-mm spacing among the antennas in the array.

meaningful bioelectromagnetic problems. Some of the future developments will involve improving the efficiencies of the various codes by techniques such as use of the expanding grid rather than the regular grid, elimination of the relatively shielded interior regions of the modeled space at higher frequencies, and use of truncated models of the body at microwave frequencies where there is a lack of coupling between the various regions of the body. Because of accurate modeling of the tissue heterogeneities and shapes, these models have and will continue to play an important role in emerging technologies with bioelectromagnetic concerns. Some of the likely applications are personal wireless and mobile communications systems, automotive devices such as electric automobiles and collision avoidance systems, medical devices such as MRIs, implantable pacemakers and defibrillators, applicators for hyperthermia, and other minimally invasive therapeutic and surgical procedures.

Acknowledgment

We wish to thank Stefano Pisa, Marta Cavagnaro, Emanuele Piuzzi, and Zhangwei Wang for their valuable assistance in preparing the manuscript.

References

1. Lin, J.C., Computer methods for field intensity predictions, in *CRC Handbook of Biological Effects of Electromagnetic Fields*, Polk, C., and Postow, E., Eds., CRC Press, Boca Raton, FL, 1986, 273–313.
2. Lin, J.C. and Gandhi, O.P., Computer methods for predicting field intensity, in *Handbook of Biological Effects of Electromagnetic Fields*, Polk, C., and Postow, E., Eds., CRC Press, Boca Raton, FL, 1996, 337–402.
3. Lin, J.C., Mechanisms of field coupling into biological systems at ELF and RF frequencies, in *Advances in Electromagnetic Fields in Living Systems*, vol. 3, Kluwer/Plenum, New York, 2000, 1–38.
4. Schwan, H.P. and Piersol, G.M., Absorption of electromagnetic energy in body tissues, *Am. J. Phys. Med*., 33, 371, 1954.
5. Schwan, H.P. and Li, K., Hazards due to total body irradiation by radar, *Proc. IRE*, 44, 1572, 1956.
6. Schwan, H.P. and Li, K., The mechanism of absorption of ultrahigh frequency electromagnetic energyin tissue as related to the problem of tolerance dosage, *IRE Trans. Med. Electron*., 4, 45, 1956.
7. Johnson, C.C. and Guy, A.W., Nonionizing electromagnetic wave effects in biological materials and systems, *Proc. IEEE*, 60, 692, 1972.
8. Michaelson, S.M. and Lin, J.C., *Biological Effects and Health Implications of Radiofrequency Radiation*, Plenum Press, New York, 1987.
9. Shapiro, A.R., Lutomirski, R.F., and Yura, H.T., Induced fields and heating within a cranial structure irradiated by an electromagnetic plane wave, *IEEE Trans. Microwave Theory Technol*., 19, 187, 1971.
10. Kritikos, H.N. and Schwan, H.P., Hot spot generated in conduction spheres by EM waves and biological implications, *IEEE Trans. Biomed. Eng*., 19, 53, 1972.
11. Lin, J.C., Guy, A.W., and Kraft, G.H., Microwave selective brain heating, *J. Microwave Power*, 8, 275, 1973.
12. Ho, H.S. and Guy, A.W., Development of dosimetry for RF and microwave radiation, *Health Phys*., 29, 317, 1975.

13. Weil, C.M., Absorption characteristics of multi-layered sphere models exposed to UHF/microwave radiation, *IEEE Trans. Biomed. Eng*., 22, 468, 1975.
14. Joines, W.T. and Spiegel, R.J., Resonance absorption of microwaves by the human skull, *IEEE Trans. Biomed. Eng*., 21, 46, 1975.
15. Lin, J.C., Interaction of two cross-polarized electromagnetic waves with mammalian cranial structures, *IEEE Trans. Biomed. Eng*., 23, 371, 1976.
16. Lin, J.C., Guy, A.W., and Johnson, C.C., Power deposition in a spherical model of man exposed to 1–20 MHz electromagnetic fields, *IEEE Trans. Microwave Theory Technol*., 21, 791, 1973 (see also corrections *IEEE MTT*, 23, 265, 1975).
17. Kritikos, H.N. and Schwan, H.P., The distribution of heating potential inside lossy spheres, *IEEE Trans. Biomed. Eng*., 22, 457, 1975.
18. Johnson, C.C., Durney, C.H., and Massoudi, H., Long-wavelength electromagnetic power absorption in prolate spheroidal models of man and animals, *IEEE Trans. Microwave Theory Technol*., 23, 739, 1975.
19. Durney, C.H., Johnson, C.C., and Massaudi, A., Long wave-length analysis of plane wave irradiation of a prolate spheroidal model of man, *IEEE Trans. Microwave Theory Technol*., 23, 246, 1975.
20. Massoudi, H., Durney, C.H., and Johnson, C.C., Long wavelength electromagnetic power absorption in ellipsoidal models of man and animals, *IEEE Trans. Microwave Theory Technol*., 24, 41, 1977.
21. Rowlandson, G.I. and Barber, P.W., Absorption of high frequency RF energy by biological models: calculations based on geometrical optics, *Radio Sci*., 14, 43S, 1979.
22. Lin, J.C., Whole-body exposure in the near zone of HF electromagnetic fields, *URSI International Electromagnetic Waves and Biology Symposium*, Jouy en Josas, France, 1980.
23. Guy, A.W., Webb, M.D., and Sorenson, C.C., Determination of power absorption in man exposed to HF electromagnetic fields by thermographic measurements on scale models, *IEEE Trans. Biomed. Eng*., 23, 361, 1976.
24. Liversy, D.E. and Chen, K.M., Electromagnetic fields induced inside arbitrary shaped biological bodies, *IEEE Trans. Microwave Theory Technol*., 22, 1273, 1974.
25. Guru, B.S. and Chen, K.M., Experimental and theoretical studies in electromagnetic field induced inside finite biological bodies, *IEEE Trans. Microwave Theory Technol*., 24, 433, 1976.
26. Chen, K.M. and Guru, B.S., Internal EM field and absorbed power density in human torsos induced by 1–500 MHz EM waves, *IEEE Trans. Microwave Theory Technol*., 25, 746. 1977.
27. Hagman, M.J., Gandhi, O.P., and Durney, C.H., Numerical calculation of electromagnetic energy deposition for a realistic model of man, *IEEE Trans. Microwave Theory Technol*., 27, 804, 1979.
28. Gandhi, O.P., Electromagnetic absorption in inhomogeneous model of man for realistic exposure conditions, *Bioelectromagnetics*, 3, 81, 1982.
29. Armitage, D.W., Leveen, H.H., and Pethig, R., Radio-frequency induced hyperthermia: computer simulation of specific absorption rate distributions using realistic anatomical models, *Phys. Med. Biol*., 28, 31, 1983.
30. Gandhi, O.P., DeFord, J.F., and Kanai, H., Impedance method for calculation of power deposition patterns in magnetically induced hyperthermia, *IEEE Trans. Biomed. Eng*., 31, 644, 1984.
31. Gandhi, O.P. and DeFord, J.F., Calculation of EM power deposition for operator exposure to RF induction heaters, *IEEE Trans. Electromagn. Compat*., 30, 63, 1988.
32. Orcutt, N. and Gandhi, O.P., A 3-D impedance method to calculate power deposition in biological bodies subjected to time-varying magnetic fields, *IEEE Trans. Biomed. Eng*., 35, 577, 1988.
33. Orcutt, N. and Gandhi, O.P., Use of the impedance method to calculate 3-D power deposition patterns for hyperthermia with capacitive plate electrodes, *IEEE Trans. Biomed. Eng*., 37, 36, 1990.
34. Epstein, B.R. and Foster, K.R., Anisotropy in dielectric properties of skeletal muscle, *Med. Biol. Eng. Comput*., 21, 51, 1983.
35. Zheng, E., Shao, S., and Webster, J.G., Impedance of skeletal muscle from 1 Hz to 1 MHz, *IEEE Trans. Biomed. Eng*., 31, 477, 1984.

36. Zhu, X.L. and Gandhi, O.P., Design of RF needle applicators for optimum SAR distributions in irregularly-shaped tumors, *IEEE Trans. Biomed. Eng*., 35, 382, 1988.
37. Gandhi, O.P. and Chen, J.Y., Numerical dosimetry at power-line frequencies using anatomically based models, *Bioelectromagnetics*, Supplement 1, 43, 1992.
38. Tofani, S., Ossola, P., d'Amore, G., and Gandhi, O.P., Electric fields and current density distributions induced in an anatomically based model of the human head by magnetic fields from a hair dryer, *Health Phys*., 68, 71–79, 1995.
39. Wu, D., Ren, J., and Gandhi, O.P., Currents induced in the arm and the body by the magnetic fields of an electric hand drill, *Abstracts of the Fifteenth Annual Meeting of the Bioelectromagnetics Society*, Los Angeles, CA, 1993, 31.
40. Ren, J., Gandhi, O.P., Casamento, J.P., and Bassen, H.I., Currents induced in the human body by electric blankets, *Abstracts of the 15th Annual Meeting of the Bioelectromagnetics Society*, Los Angeles, CA, 1993, 32.
41. Harrington, R.F., *Field Computation by Moment Methods*, McGraw-Hill, New York, 1968.
42. Schelkunoff, S.A., Field equivalence theorems, *Comm. Pure Appl. Math*., 4, 43, 1951.
43. Lin, J.C. and Wu, C.L., Scattering of microwaves by dielectric materials used in laboratory animal restrainers, *IEEE Trans. Microwave Theory Technol*., 24, 219, 1976.
44. Gandhi, O.P., Hagman, M.J., and D'Andrea, J.A., Part-body and multi-body effects on absorption of radio frequency electromagnetic energy by animals and by models of man, *Radio Sci*., 14, 155, 1979.
45. Karimullah, K., Chen, K.M., and Nyquist, D.P., Electromagnetic coupling between a thin-wire antenna and a neighboring biological body, *IEEE Trans. Microwave Theory Technol*., 28, 1218, 1980.
46. Chatterjee, I., Hagman, M.J., and Gandhi, O.P., Electromagnetic energy deposition in an inhomogeneous block model for near-field irradiation conditions, *IEEE Trans. Microwave Theory Technol*., 28, 1452, 1980.
47. Wu, T.K. and Tsai, L.L., Electromagnetic fields induced inside arbitrary cylinders of biological tissue, *IEEE Trans. Microwave Theory Technol*., 25, 61, 1977.
48. Wu, T.K. and Tsai, L.L., Scattering from arbitrary-shaped lossy dielectric bodies of revolution, *Radio Sci*., 12, 709, 1977.
49. Poggio, A.J. and Miller, E.K., Integral equation solutions of three-dimensional scattering problems, in *Computer Techniques for Electromagnetics*, Mittra, R., Ed., Pergamon Press, Elmsford, New York, 1973, 159.
50. Massoudi, H., Durney, C.H., Barber, P.W., and Iskander, M.F., Post resonance EM absorption by man and animals, *Bioelectromagnetics*, 3, 333, 1982.
51. Wu, T.K., Electromagnetic fields and power deposition in body of revolution models of man, *IEEE Trans. Microwave Theory Technol*., 27, 279, 1979.
52. Mautz, J.R. and Harrington, R.F., Radiation and scattering from bodies of revolution, *Appl. Sci. Res*., 20, 405, 1969.
53. Harrington, R.F. and Mautz, J.R., Green's functions for surfaces of revolution, *Radio Sci*., 7, 603, 1972.
54. Pogorzelski, R.J. and Wu, T.K., Computations of scattering from inhomogeneous penetrable elliptic cylinders by means of invariant imbedding, in *URSI Symposium of Electromagnetic Wave Theory*, Stanford, CA, 1977, 323.
55. Jin, J., *The Finite Element Method in Electromagnetics*, Wiley, New York, 1993.
56. Boyes, W.E., Lynch, D.R., Paulsen, K.D., and Minerbo, G.N., Nodal-based finite element modelling of Maxwell's equations in three dimensions, *IEEE Trans. Antennas Propagat*., 40, 642, 1992.
57. Paulsen, K.D., Jia, X., and Sullivan, J.M., Jr., Finite element computations of specific absorption rates in anatomically conforming full-body models for hyperthermia treatment analysis, *IEEE Trans. Biomed. Eng*., 40, 933, 1993.
58. Yee, K.S., Numerical solutions of initial boundary value problems involving Maxwell's equations in isotropic media, *IEEE Trans. Antennas Propagat*., 14, 303, 1966.
59. Taflove, A. and Brodwin, M.E., Computation of the electromagnetic fields and induced temperatures within a model of the microwave-irradiated human eye, *IEEE Trans. Microwave Theory Technol*., 23, 888, 1975.

60. Taflove, A. and Brodwin, M.E., Numerical solution of steady-state EM scattering problems using the time dependent Maxwell's equation, *IEEE Trans. Microwave Theory Technol.*, 23, 623, 1975.
61. Taflove, A., Application of the finite-difference time domain method to sinusoidal steady-state electromagnetic-penetration problems, *IEEE Trans. Electromagn. Compat.*, 22, 191, 1980.
62. Holland, R., THREDE: a free field EMP coupling and scattering code, *IEEE Trans. Nuclear Sci.*, 24, 2416, 1977.
63. Kunz, K.S. and Lee, K.M., A three-dimensional finite-difference solution of the external response of an aircraft to a complex transient EM environment: part 1—the method and its implementation, *IEEE Trans. Electromagn. Compat.*, 20, 328, 1978.
64. Kunz, K.S. and Luebbers, R.J., *The Finite-Difference Time-Domain Method for Electromagnetics*, CRC Press, Boca Raton, FL, 1993.
65. Taflove, A., *Computational Electrodynamics: The Finite-Difference Time-Domain Method*, Artech House, London, 1995.
66. Taflove, A. and Hagness, S.C., Eds., *Computational Electrodynamics: The Finite-Difference Time-Domain Method*, Artech House, London, 2000.
67. Spiegel, R.J., Fatmi, M.B.A., Stuchly, S.S., and Stuchly, M.A., Comparison of finite-difference time-domain SAR calculations with measurements, in a heterogeneous model of man, *IEEE Trans. Biomed. Eng.*, 36, 849, 1989.
68. Chen, J.Y. and Gandhi, O.P., Currents induced in an anatomically based model of a human for exposure to vertically polarized electromagnetic pulses, *IEEE Trans. Microwave Theory Technol.*, 39, 31, 1991.
69. Sullivan, D.M., Borup, D.T., and Gandhi, O.P., Use of the finite-difference time-domain method in calculating EM absorption in human tissues, *IEEE Trans. Biomed. Eng.*, 34, 148, 1987.
70. Chen, J.Y. and Gandhi, O.P., Numerical simulation of annular-phased arrays of dipoles for hyperthermia of deep-seated tumors, *IEEE Trans. Biomed. Eng.*, 39, 209, 1992.
71. Chen, J.Y., Gandhi, O.P., and Conover, D.L., SAR and induced current distributions for operator exposure to RF dielectric sealers, *IEEE Trans. Electromagn. Compat.*, 33, 252, 1991.
72. Luebbers, R., Hunsberger, F.P., Kunz, K.S., Standler, R.B., and Schneider, M., A frequency-dependent finite-difference time-domain formulation for dispersive materials, *IEEE Trans. Electromagn. Compat.*, 32, 222, 1990.
73. Bui, M.D., Stuchly, S.S., and Costache, G.I., Propagation of transients in dispersive dielectric media, *IEEE Trans. Microwave Theory Technol.*, 39, 1165, 1991.
74. Sullivan, D.M., A frequency-dependent FDTD method for biological applications, *IEEE Trans. Microwave Theory Technol.*, 40, 532, 1992.
75. Luebbers, R.J., Hunsberger, F., and Kunz, K.S., FDTD for nth order dispersive media, *IEEE Trans. Antennas Propagat.*, 40, 1297, 1992.
76. Joseph, R.M., Hagness, S.C., and Taflove, A., Direct time integration of Maxwell's equations in linear dispersive media with absorption for scattering and propagation of femtosecond electromagnetic impulses, *Optics Lett.*, 16, 1412, 1991.
77. Gandhi, O.P., Gao, B.Q., and Chen, J.Y., A frequency-dependent finite-difference time-domain formulation for induced current calculations in human beings, *Bioelectromagnetics*, 13, 543, 1992.
78. Gandhi, O.P., Gao, B.Q., and Chen, J.Y., A frequency-dependent finite-difference time-domain formulation for general dispersive media, *IEEE Trans. Microwave Theory Technol.*, 41, 658, 1993.
79. Furse, C.M., Chen, J.Y., and Gandhi, O.P., A frequency-dependent finite-difference time-domain method for induced current and SAR calculations for a heterogeneous model of the human body, *IEEE Trans. Electromagn. Compat.*, 36, 128, 1994.
80. Gandhi, O.P. and Chen, J.Y., Electromagnetic absorption in the human head for a proposed 6 GHz mobile communication system, *IEEE Trans. Electromagn. Compat.*, 37, 547, 1995.
81. Gandhi, O.P., Some numerical methods for dosimetry: ELF to microwave frequencies, *Radio Sci.*, 30, 161–177, 1995.
82. Ackerman, M.J., The visible human project, *Proc. IEEE*, 86, 504, 1998.

83. Mason, P.A., Ziriax, J.M., Hurt, W.D., Walters, T.J., Ryan, K.L., Nelson, D.A., Smith, K.I., and D'Andrea, J.A., Recent advancements in dosimetry measurements and modeling, in *Radio Frequency Radiation Dosimetry*, Klauenberg, B.J. and Miklavcic, D., Eds., Kluwer, Newyork, 2000, 141.
84. fttp://starview.brooks. af.mil/EMF/dosimetry_models/
85. Rush, S., Abildskov, J.A., and McFee, R., Resistivity of body tissues at low frequencies, *Circ. Res.*, 12, 40, 1963.
86. Florig, H.K., Hoburg, J.F., and Morgan, M.G., Electric-field exposure from electric blankets, *IEEE Trans. Power Deliv.*, 2, 527, 1987.
87. Hayashi, N., Isaka, K., and Yokoi, Y., Analysis of magnetic-field profiles in electric blanket users, *IEEE Trans. Power Deliv.*, 4, 1897, 1989.
88. Kaune, W.T. and Gillis, M.F., General properties of the interaction between animals and ELF electric fields, *Bioelectromagnetics*, 2, 1, 1981.
89. Guy, A.W., Davidow, S., Yang, G.Y., and Chou, C.K., Determination of electric current distributions in animals and humans exposed to a uniform 60-Hz high-intensity electric field, *Bioelectromagnetics*, 3, 47, 1982.
90. Stratton, J.A., *Electromagnetic Theory*, McGraw-Hill, New York, 1941.
91. Deno, D.W., Currents induced in the human body by high voltage transmission line electric field—measurement and calculation of distribution and dose, *IEEE Trans. Power Apparatus Syst.*, 96, 1517, 1977.
92. DiPlacido, J., Shih, C.H., and Ware, B.J., Analysis of the proximity effects in electric field measurements, *IEEE Trans. Power Apparatus Syst.*, 97, 2167, 1978.
93. Rukspollmuang, S. and Chen, K.M., Heating of spherical vs. realistic models of human and infrahuman heads by electromagnetic waves, *Radio Sci.*, 14, 51, 1979.
94. Hagman, M.J., Gandhi, O.P., D'Andrea, J.A., and Chatterjee, I., Head resonance: numerical solutions and experimental results, *IEEE Trans. Microwave Theory Technol.*, 27, 809, 1979.
95. Gandhi, O.P., Hunt, E.L., and D'Andrea, J.A., Deposition of EM energy in animals and in models of man with and without grounding and reflector effects, *Radio Sci.*, 12, 39S, 1977.
96. Deford, J.F., Gandhi, O.P., and Hagman, M.J., Moment-method solutions and SAR calculations for inhomogeneous models of man with large number of cells, *IEEE Trans. Microwave Theory Technol.*, 31, 848, 1983.
97. Sullivan, D.M., Gandhi Om, P., and Taflove, A., Use of the finite-difference time-domain method for calculating EM absorption in man models, *IEEE Trans. Biomed. Eng.*, 35, 179, 1988.
98. Bernardi, P., Cavagnaro, M., Pisa, S., and Piuzzi, E., Specific absorption rate and temperature elevation in a subject exposed in the far-field of radio-frequency sources operating in the 10–900-MHz range, *IEEE Trans. Biomed. Eng.*, 50, 295, 2003.
99. Dimbylow, P.J., FDTD calculations of the whole-body averaged SAR in an anatomically realistic voxel model of the human body from 1 MHz to 1 GHz, *Phys. Med. Biol.*, 42, 479, 1997.
100. ICNIRP, Guidelines for limiting exposure to time-varying electric, magnetic, and electromagnetic fields (up to 300 GHz), *Health Phys.*, 74, 494, 1998.
101. IEEE, IEEE standard for safety levels with respect to human exposure to radio frequency electromagnetic fields, 3 kHz to 300 GHz, in *IEEE Standard C95.1*, 1999.
102. Dimbylow, P.J., Fine resolution calculations of SAR in the human body for frequencies up to 3 GHz, *Phys. Med. Biol.*, 47, 2835, 2002.
103. Mason, A.P., Hurt, W.D., Walters, T.J., D'Andrea, J.A., Gajšek, P., Ryan, K.L., Nelson, D.A., Smith, K.I., and Ziriax, J.M., Effects of frequency, permittivity, and voxel size on predicted specific absorption rate values in biological tissue during electromagnetic-field exposure, *IEEE Trans. Microwave Theory Technol.*, 48, 2050, 2000.
104. Gajšek, P., Hurt, W.D., Ziriax, J.M., and Mason, A.P., Parametric dependence of SAR on permittivity values in a man model, *IEEE Trans. Biomed. Eng.*, 48, 1169, 2001.
105. Mazzurana, M., Sandrini, L., Vaccari, A., Malacarne, C., Cristoforetti, L., and Pontalti, R., A semi-automatic method for developing an anthropomorphic numerical model of dielectric anatomy by MRI, *Phys. Med. Biol.*, 48, 3157, 2003.
106. Tinniswood, A.D., Furse, C.M., and Gandhi Om, P., Power deposition in the head and neck of an anatomically based human body model for plane wave exposures, *Phys. Med. Biol.*, 43, 2361, 1998.

107. Nagaoka, T., Watanabe, S., Sakurai, K., Kunieda, E., Watanabe, S., Taki, M., and Yamanaka, Y., Development of realistic high-resolution whole-body voxel models of japanese adult males and females of average height and weight, and application of models to radio-frequency electromagnetic-field dosimetry, *Phys. Med. Biol.*, 49, 1, 2004.
108. Sandrini, L., Vaccari, A., Malacarne, C., Cristoforetti, L., and Pontalti, R., RF dosimetry: a comparison between power absorption of female and male numerical models from 0.1 to 4 GHz, *Phys. Med. Biol.*, 49, 5185, 2004.
109. Gabriel, S., Lau, R.W., and Gabriel C., The dielectric properties of biological tissues: III. Parametric models for the dielectric spectrum of tissues, *Phys. Med. Biol.*, 41, 2271, 1996.
110. Gabriel, C., Compilation of the Dielectric Properties of Body Tissues at RF and Microwave Frequencies, Technical Report, AL/OE-TR-1996–0037, Brooks Air Force, Brooks AFB, TX, 1996.
111. Faraone, A., Tay, R.Y.-S., Joyner, K.H., and Balzano, Q., Estimation of the average power density in the vicinity of cellular base-station collinear array antennas, *IEEE Trans. Veh. Technol.*, 49, 984, 2000.
112. Cicchetti, R. and Faraone, A., Estimation of the peak power density in the vicinity of cellular and radio base station antennas, *IEEE Trans. Electromagn. Compat.*, 46, 275, 2004.
113. Bizzi, M. and Gianola, P., Electromagnetic fields radiated by GSM antennas, *Electron. Lett.*, 35, 855, 1999.
114. Altman, Z., Begasse, B., Dale, C., Karwowski, A., Wiart, J., Wong, M.F., and Gattoufi, L., Efficient models for base station antennas for human exposure assessment, *IEEE Trans. Electromagn. Compat.*, 44, 588, 2002.
115. Bernardi, P., Cavagnaro, M., Cristoforetti, L., Malacarne, C., Pisa, S., Piuzzi, E., Pontalti, R., and Vaccari, A., Modelling of BTS antennas: Dependence of the accuracy on FDTD mesh size and implementation criteria, in *Proceedings of the 2nd International Workshop on Biological Effects of Electromagnetic Fields*, Rhodes, Greece, Kostarakis, P., Ed., 2002, 74.
116. Blanch, S., Romeu, J., and Cardama, A., Near field in the vicinity of wireless base-station antennas: an exposure compliance approach, *IEEE Trans. Antennas Propagat.*, 50, 685, 2002.
117. Adane, Y., Gati, A., Wong, M.-F., Dale, C., Wiart, J., and Hanna V.F., Optimal modeling of real radio base station antennas for human exposure assessment using spherical-mode decomposition, *Antennas Wireless Propagat. Lett.*, 1, 215, 2002.
118. Fridén, J., RF exposure compliance boundary analysis of base station antennas using combined spherical–cylindrical near-field transformations, *Electron. Lett.*, 39, 1783, 2003.
119. Nicolas, E., Lautru, D., Jacquin, F., Wong, M.F., and Wiart, J., Specific absorption rate assessments based on a selective isotropic measuring system for electromagnetic fields, *IEEE Trans. Instrum. Meas.*, 50, 397, 2001.
120. Lazzi, G. and Gandhi, O.P., A mixed FDTD-integral equation approach for on-site safety assessment in complex electromagnetic environments, *IEEE Trans. Antennas Propagat.*, 48, 1830, 2000.
121. Gandhi, O.P. and Lam, M.S., An on-site dosimetry system for safety assessment of wireless base stations using spatial harmonic components, *IEEE Trans. Antennas Propagat.*, 51, 840, 2003.
122. Cooper, J., Marx, B., Buhl, J., and Hombach, V., Determination of safety distance limits for a human near a cellular base station antenna, adopting the IEEE standard or ICNIRP guidelines, *Bioelectromagnetics*, 23, 429, 2002.
123. Catarinucci, L., Palazzari, P., and Tarricone, L., Human exposure to the near field of radiobase antennas—a full-wave solution using parallel FDTD, *IEEE Trans. Microwave Theory Technol.*, 51, 935, 2003.
124. Bernardi, P., Cavagnaro, M., Pisa, S., and Piuzzi, E., Human exposure in the vicinity of radio base station antennas, in *Proceedings of EMC Europe 2000 (4th European Symposium on Electromagnetic Compatibility)*, Brugge, Belgium, 2000, 187.
125. Meyer, F.J.C., Davidson, D.B., Jakobus, U., and Stuchly M.A., Human exposure assessment in the near field of GSM base-station antennas using a hybrid finite element/method of moments technique, *IEEE Trans. Biomed. Eng.*, 50, 224, 2003.
126. Bernardi, P., Cavagnaro, M., Pisa, S., and Piuzzi, E., Human exposure to cellular base station antennas in urban environment, *IEEE Trans. Microwave Theory Technol.*, 48, 1996, 2000.

127. Alaydrus, M., Bitz, A., Streckert, J., and Hansen, V., Combination of the hybrid$^{(2)}$–method and the FDTD for safety assessment of human for base station antennas mounted in real environments, in XXVIIth General Assembly of International Union of Radio Science, Maastricht, The Netherlands, 2002.
128. Martinez-Burdalo, M., Nonidez, L., Martin, A., and Villar, R., Near-field time-domain physical-optics and FDTD method for safety assessment near a base-station antenna, *Microwave Opt. Technol. Lett*., 39, 393, 2003.
129. Bernardi, P., Cavagnaro, M., Cicchetti, R., Pisa, S., Piuzzi, E., and Testa, O., A UTD/FDTD investigation on procedures to assess compliance of cellular base-station antennas with human-exposure limits in a realistic urban environment, *IEEE Trans. Microwave Theory Technol*., 51, 2409, 2003.
130. Bernardi, P., Cavagnaro, M., Cicchetti, R., Pisa, S., Piuzzi, E., and Testa, O., Human exposure to the electromagnetic fields produced by coexisting wireless communication systems in a complex indoor environment, in *Proceedings of EMC Europe 2004 (International Symposium of Electromagnetic Compatibility)*, Eindhoven, The Netherlands, 2004, 79.
131. Lin, J.C., Interaction of electromagnetic transient radiation with biological materials, *IEEE Trans. Electromagn. Compat*., 17, 93, 1975.
132. Lin, J.C., Wu, C.L., and Lam, C.K., Transmission of electromagnetic pulse into the head, *Proc. IEEE*, 63, 1726, 1975.
133. Lin, J.C., Electromagnetic pulse interaction with mammalian cranial structures, *IEEE Trans. Biomed. Eng*., 23, 61, 1976.
134. Lin, J.C. and Lam, C.K., Coupling of Gaussian electromagnetic pulse into muscle-bone model of biological structure, *J. Microwave Power*, 11, 67, 1976.
135. Lin, J.C., The microwave auditory phenomenon, *Proc. IEEE*, 68, 67, 1980.
136. Lin, J.C., Microwave-induced hearing sensation: some preliminary theoretical observations, *J. Microwave Power*, 11, 295, 1976.
137. Lin, J.C., On Microwave-induced hearing sensation, *IEEE Trans. Microwave Theory Technol*., 25, 605, 1977.
138. Lin, J.C., Further studies on the microwave auditory effects, *IEEE Trans. Microwave Theory Technol*., 25, 936, 1977.
139. Lin, J.C., Calculations of frequencies and threshold of microwave-induced auditory signals, *Radio Sci*., 12, SS-1, 237, 1977.
140. Lin, J.C., *Microwave Auditory Effects and Applications*, Charles C. Thomas, Publisher, Springfield, IL, 1978.
141. Watanabe, Y., Tanaka, T., Taki, M., and Watanabe, S., FDTD analysis of microwave hearing effect, *IEEE MTT*, 48, 2126, 2000.
142. Lin, J.C. and Wang, Z.W., RF thermoelastic pressures induced in a human head model in high-pass MRI birdcage coils, in ISMRM, Miami, 2005.
143. Wang, Z.W. and Lin, J.C., RF induced thermoelastic pressure waves in different size human head models in MRI birdcage coils, in 27th Annual Meeting of Bioelectromagnetics Society, Dublin, Ireland, June 2005.
144. Yang, L.Q. and Giannakis, G.B., Ultra-wideband communications, *IEEE Signal Process. Mag*., 21, 26, 2004.
145. Qiu, R.C., Liu, H.P., and Shen, X.M., Ultra-wideband for multiple access communications, *IEEE Commun. Mag*., 43, 80, 2005.
146. Gandhi, O.P., Gu, Y.G., Chen, J.Y., and Bassen, H.I., Specific absorption rates and induced current distributions in an anatomically based human model for plane-wave exposures, *Health Phys*., 63, 281, 1992.
147. FCC, Evaluating compliance with FCC guidelines for human exposure to radiofrequency electromagnetic fields, in *OET Bulletin 65*, FCC, Washington, DC, Aug. 1997.
148. IEC, human exposure to radio frequency fields from hand-held and body-mounted wireless communication devices—human models, instrumentation, and procedures—part 1: procedure to determine the specific absorption rate (SAR) for hand-held devices used in close proximity to the ear (frequency range of 300 MHz to 3 GHz), in *IEC Standard, 62209-1*, 2005.

149. Toftgard, J., Hornsleth, S.N., and Andersen, J.B., Effects on portable antennas of the presence of a person, *IEEE Trans. Antennas Propagat.*, 41, 739, 1993.
150. Dimbylow, P.J. and Mann, S.M., SAR calculations in an anatomically realistic model of the head for mobile communication transceivers at 900 MHz and 1.8 GHz, *Phys. Med. Biol.*, 39, 1537, 1994.
151. Gandhi, O.P., Lazzi, G., and Furse, C.M., Electromagnetic absorption in the human head and neck for mobile telephones at 835 and 1900 MHz, *IEEE Trans. Microwave Theory Technol.*, 44, 1884, 1996.
152. Okoniewski, M., and Stuchly, M.A., A study of the handset antenna and human body interaction, *IEEE Trans. Microwave Theory Technol.*, 44, 1855, 1996.
153. Hombach, V., Meier, K., Burkhardt, M., Kuhn, E., and Kuster, N., The dependence of EM energy absorption upon human head modeling at 900 MHz, *IEEE Trans. Microwave Theory Technol.*, 44, 1865, 1996.
154. Watanabe, S., Taki, M., Nojima, T., and Fujiwara, O., Characteristics of the SAR distributions in a head exposed to electromagnetic fields radiated by a hand-held portable radio, *IEEE Trans. Microwave Theory Technol.*, 44, 1874, 1996.
155. Bernardi, P., Cavagnaro, M., and Pisa, S., Evaluation of the SAR distribution in the human head for cellular phones used in a partially closed environment, *IEEE Trans. Electromagn. Compat.*, 38, 357, 1996.
156. Colburn, J.S., and Rahmat-Samii, Y., Human proximity effects on circular polarized handset antennas in personal satellite communications, *IEEE Trans. Antennas Propagat.*, 46, 813, 1998.
157. Lazzi, G., and Gandhi, O.P., On modeling and personal dosimetry of cellular telephone helical antennas with the FDTD code, *IEEE Trans. Antennas Propagat.*, 46, 525, 1998.
158. Mangoud, M.A., Abd-Alhameed, R.A., and Excell, P.S., Simulation of human interaction with mobile telephones using hybrid techniques over coupled domains, *IEEE Trans. Microwave Theory Technol.*, 48, 2014, 2000.
159. Cerri, G., Russo, P., Schiavoni, A., Tribellini, G., and Bielli, P., A new MoM-FDTD hybrid technique for the analysis of scattering problems, *Electron. Lett.*, 34, 438, 1998.
160. Bernardi, P., Cavagnaro, M., Pisa, S., and Piuzzi, E., A graded-mesh FDTD code for the study of human exposure to cellular phones equipped with helical antennas, *Appl. Comput. Electromagn. Soc. J.*, 16, 90, 2001.
161. Bernardi, P., Cavagnaro, M., Pisa, S., and Piuzzi, E., Power absorption and temperature elevations induced in the human head by a dual-band monopole-helix antenna phone, *IEEE Trans. Microwave Theory Technol.*, 49, 2539, 2001.
162. Jensen, M.A. and Rahmat-Samii, Y., EM interaction of handset antennas and a human in personal communications, *Proc. IEEE*, 83, 7, 1995.
163. Rowley, J.T. and Waterhouse, R.B., Performance of shorted patch antennas for mobile communication handsets at 1800 MHz, *IEEE Trans. Microwave Theory Technol.*, 47, 815, 1999.
164. Bernardi, P., Cavagnaro, M., Pisa, S., and Piuzzi, E., Specific absorption rate and temperature increases in the head of a cellular-phone user, *IEEE Trans. Microwave Theory Technol.*, 48, 1118, 2000.
165. de Salles, A.A., Fernandez, C.R., and Bonadiman, M., FDTD simulations and measurements on planar antennas for mobile phones, *Proc. SBMO/IEEE MTT-S IMOC*, 1043, 2003.
166. Tinniswood, A.D., Furse, C.M., and Gandhi, O.P., Computations of SAR distributions for two anatomically based models of the human head using CAD files of commercial telephones and the parallelized FDTD code, *IEEE Trans. Antennas Propagat.*, 46, 829, 1998.
167. Schiavoni, A., Bertotto, P., Richiardi, G., and Bielli, P., SAR generated by commercial cellular phones—phone modeling, head modeling, and measurements, *IEEE Trans. Microwave Theory Technol.*, 48, 2064, 2000.
168. Chavannes, N., Tay, R., Nikoloski, N., and Kuster, N., Suitability of FDTD-based TCAD tools for RF design of mobile phones, *IEEE Antennas Propagat. Mag.*, 45, 52, 2003.
169. Pisa, S., Cavagnaro, M., Lopresto, V., Piuzzi, E., Lovisolo, G.A., and Bernardi, P., A procedure to develop realistic numerical models of cellular phones for an accurate evaluation of SAR distribution in the human head, *IEEE Trans. Microwave Theory Technol.*, 53, 2005.
170. Lin, J.C., Cellular mobile telephones and children, *IEEE Antennas Propagat. Mag.*, 44, 142, 2002.
171. Peyman, A., Rezazadeh, A.A., and Gabriel, C. Changes in the dielectric properties of rat tissue as a function of age at microwave frequencies, *Phys. Med. Biol.*, 46, 1617, 2001.

172. Gandhi, O.M. and Kang, G., Some present problems and a proposed experimental phantom for SAR compliance testing of cellular telephone at 835 and 1900 MHz, *Phys. Med. Biol*, 47, 1501, 2002.
173. Schoenborn, F., Burkhardt, M., and Kuster, N., Differences in energy absorption between heads of adults and children in the near field of sources, *Health Phys*., 74, 160, 1998.
174. Guy, A.W., Chou, C.K., and Bit-Babik, G., FDTD derived SAR distributions in various size human head models exposed to simulated cellular telephone handset transmitting 600 mW at 835 MHz, in *24th Bioelectromagnetics Society Annual Meeting*, Quebec, Canada, 7, 2002.
175. Wang, J. and Fujiwara, O., Comparison and evaluation of electromagnetic absorption characteristic in realistic human head models of adult and children for 900-MHz mobile telephones, *IEEE Trans. Microwave Theory Technol*., 51, 966, 2003.
176. Hadjem, A., Lautru, D., Dale, C., Wong, M.F., Hanna, V.H., and Wiart, J., Study of specific absorption rate (SAR) induced in two child head models and in adult heads using mobile phones, *IEEE Trans. Microwave Theory Technol*., 53, 4, 2005.
177. Dominguez, H., Raizer, A., and Carpes, W.P., Jr., Electromagnetic fields radiated by cellular phone in close proximity to metallic walls, *IEEE Trans. Magn*., 38, 793, 2002.
178. Anzaldi, G., Delgado, E.C., Riu, P.J., and Silva, F., FDTD analysis of SAR from a cell phone inside a vehicle, in *Proceedings of the 16th International Symposium on Electromagnetic Compatibility*, Zurich, Switzerland, 2005, 155.
179. Ruddle, A.R., Modelling electromagnetic field exposure and SAR in vehicles due to on-board transmitters, in *Proceedings of the 16th International Symposium on Electromagnetic Compatibility*, Zurich, Switzerland, 2005, 145.
180. Onishi, T., Iyama, T., and Uebayashi, S., The estimation of the maximum SAR with respect to various types of wireless device usage, in *Proceedings of 16th International Symposium on Electromagnetic Compatibility*, Zurich, Switzerland, 2005, 151.
181. Bernardi, P., Cavagnaro, M., Pisa, S., Piuzzi, E, and Lin, J., SAR distribution produced by cellular phones radiating close to the human body, in BioEM-2005 Meeting, Dublin, Ireland, 2005.
182. Pennes, H.H., Analysis of tissue and arterial blood temperatures in resting forearm, *J. Appl. Physiol*., 1, 93, 1948.
183. Stolwijk, J.A.J. and Hardy, J.D., Control of body temperature, in *Handbook of Physiology—Reaction to Environmental Agents*, Lee, D.H.K., Ed., Am. Physiol. Soc. Bethesda, MD, 1977, 45.
184. Spiegel, R.J., A review of numerical models for predicting the energy deposition and resultant thermal responses of humans exposed to electromagnetic fields, *IEEE Trans. Microwave Theory Technol*., 32, 730, 1984.
185. Mooibroek, J. and Lagendijk, J.J.W., A fast and simple algorithm for the calculation of convective heat transfer by large vessels in three-dimensional inhomogeneous tissues, *IEEE Trans. Biomed. Eng*., 38, 490, 1991.
186. Kolios, M.C., Sherar, M.D., and Hunt, J.W., Large blood vessel cooling in heated tissues: a numerical study, *Phys. Med. Biol*., 40, 477, 1995.
187. Van Leeuwen, G.M.J., Lagendijk, J.J.W., Van Leersum, B.J.A.M., Zwamborn, A.P.M., Hornsleth, S.N., and Kotte, A.N.T.J., Calculation of change in brain temperatures due to exposure to a mobile phone, *Phys. Med. Biol*., 44, 2367, 1999.
188. Ma, L., Paul, D.-L., Pothecary, N., Railton, C., Bows, J., Barratt, L., Mullin, J., and Simons, D., Experimental validation of a combined electromagnetic and thermal FDTD model of a microwave heating process, *IEEE Trans. Microwave Theory Technol*., 43, 2565, 1995.
189. Torres, F. and Jecko, B., Complete FDTD analysis of microwave heating process in frequency-dependent and temperature-dependent media, *IEEE Trans. Microwave Theory Technol*., 45, 108, 1997.
190. Lu, C.-C., Li, H.-Z., and Gao, D., Combined electromagnetic and heat-conduction analysis of rapid rewarming of cryopreserved tissues, *IEEE Trans. Microwave Theory Technol*., 48, 2185, 2000.
191. Gordon, R.G., Roemer, R.B., and Horvath, S.M., A mathematical model of the human temperature regulatory system—transient cold exposure response, *IEEE Trans. Biomed. Eng*., 23, 434, 1976.

192. Ozisik, N., *Heat Transfer: A Basic Approach*, McGraw-Hill, New York, 1985.
193. Gagge, A.P. and Nishi, Y., Heat exchange between human skin surface and thermal environment, in *Handbook of Physiology—Reaction to Environmental Agents*, Lee, D.H.K., Ed., Am. Physiol. Soc. Bethesda, MD, 1977, 69.
194. Haala, J. and Wiesbeck, W., Modeling microwave and hybrid heating processes including heat radiation effects, *IEEE Trans. Microwave Theory Technol.*, 50, 1346, 2002.
195. Adair, E.R., Thermal physiology of radiofrequency radiation (RFR) interactions in animals and humans, in *Radiofrequency Radiation Standards*, Klanenberg, B.J., Grandolfo, M., and Erwin, D.N., Eds., Plenum Press, New York, 1994, 245.
196. Hoque, M. and Gandhi, O.P., Temperature distributions in the human leg for VLF-VHF exposures at the ANSI recommended safety levels, *IEEE Trans. Biomed. Eng.*, 35, 442, 1988.
197. Chatterjee, I. and Gandhi, O.P., An inhomogeneous thermal block model of man for the electromagnetic environment, *IEEE Trans. Biomed. Eng.*, 30, 707, 1983.
198. Guyton, A.C., *Textbook of Medical Physiology*, W.B. Saunders Company, Philadelphia, PA, 1991.
199. Bardati, F., Gerosa, G., and Lampariello, P., Temperature distribution in simulated living tissues irradiated electromagnetically, *Alta Freq.*, XLIX, 61, 1980.
200. Durkee, J.W., Antich, P.P., and Lee, C.E., Exact solutions to the multiregion time-dependent bioheat equation. I: solution development, *Phys. Med. Biol.*, 35, 847, 1990.
201. Vyas, R. and Rustgi, M.L., Green's function solution to the tissue bioheat equation, *Med. Phys.*, 19, 1319, 1992.
202. Way, W.I., Kritikos, H., and Schwan, H., Thermoregulatory physiological responses in the human body exposed to microwave radiation, *Bioelectromagnetics*, 2, 341, 1981.
203. Charny, C.K., Hagmann, M.J., and Levin, R.L., A whole body thermal model of man during hyperthermia, *IEEE Trans. Biomed. Eng.*, 34, 375, 1987.
204. Scott, J.A., A finite element model of heat transport in the human eye, *Phys. Med. Biol.*, 33, 227, 1988.
205. Labonté, S., Blais, A., Legault, S.R., Ali, H.O., and Roy, L., Monopole antennas for microwave catheter ablation, *IEEE Trans. Microwave Theory Technol.*, 44, 1832, 1996.
206. Wang, J. and Fujiwara, O., FDTD computation of temperature rise in the human head for portable telephones, *IEEE Trans. Microwave Theory Technol.*, 47, 1528, 1999.
207. Pisa, S., Cavagnaro, M., Piuzzi, E., Bernardi, P., and Lin, J.C., Power density and temperature distributions produced by interstitial arrays of sleeved-slot antennas for hyperthermic cancer therapy, *IEEE Trans. Microwave Theory Technol.*, 51, 2418, 2003.
208. Peaceman, D.W. and Rachford, H., The numerical solution of parabolic and elliptic differential equations, *J. Soc. Ind. Appl. Math.*, 3, 28, 1955.
209. Douglas, J., On the numerical integration of $u_{xx}+u_{yy} = u_t$ by implicit methods, *J. Soc. Ind. Appl. Math.*, 3, 42, 1955.
210. Douglas, J., Alternating direction methods for three space variables, *Numer. Math.*, 4, 41, 1962.
211. Guyton, A.C., *Textbook of Medical Physiology*, W.B. Saunders Company, Philadelphia, PA, 1991.
212. Guy, A.W., Lin, J.C., Kramar, P.O., and Emery, A.F., Effect of 2450 MHz radiation on the rabbit eye, *IEEE Trans. Microwave Theory Technol.*, 23, 492, 1975.
213. Appleton, B., Hirsch, S.E., and Brown, P.V.K., Investigation of single-exposure microwave ocular effects at 3000 MHz, *Ann. NY Acad. Sci.*, 247, 125, 1975.
214. Sliney, D.H. and Stuck, B.E. Microwave exposure limits for the eye: applying infrared laser threshold data, in *Radiofrequency Radiation Standards*, Klanenberg, B.J., Grandolfo, M., and Erwin, D.N., Eds., Plenum Press, New York, 1994, 79.
215. Hardy, J.D., Wolff, H.G., and Goodell, H., *Pain Sensations and Reactions*, Williams and Wilkins, Baltimore, MD, 1952.
216. Foster, K.R., and Erdreich, L.S., Thermal models for microwave hazards and their role in standards development, *Bioelectromagnetics,* 20, 52, 1999.
217. Riu, P.J. and Foster, K.R., Heating of tissue by near-field exposure to a dipole: a model analysis, *IEEE Trans. Biomed. Eng.*, 46, 911, 1999.
218. Cherry, P.C. and Iskander, M.F., Calculations of heating patterns of an array of microwave interstitial antennas, *IEEE Trans. Biomed. Eng.*, 40, 771, 1993.

219. Bernardi, P., Cavagnaro, M., Pisa, S., and Piuzzi, E., SAR distribution and temperature increase in an anatomical model of the human eye exposed to the field radiated by the user antenna in a wireless LAN, *IEEE Trans. Microwave Theory Technol.*, 46, 2074, 1998.
220. Wainwright, P., Thermal effects of radiation from cellular telephones, *Phys. Med. Biol.*, 45, 2363, 2000.
221. Gandhi, O.M., Li, Q.X., and Kang, G., Temperature rise for the human head for cellular telephones and for peak SARs prescribed in safety guidelines, *IEEE Trans. Microwave Theory Technol.*, 49, 1607, 2001.
222. Hirata, A., Morita, M., and Shiozawa, T., Temperature increase in the human head due to a dipole antenna at microwave frequencies, *IEEE Trans. Electromagn. Compat.*, 45, 109, 2003.
223. Hirata, A. and Shiozawa, T., Correlation of maximum temperature increase and peak SAR in the human head due to handset antennas, *IEEE Trans. Microwave Theory Technol.*, 51, 1834, 2003.
224. Beckman, K.J., Lin, J.C., Wang, Y., Illes, R.W., Papp, M.A., and Hariman, R.J., Production of reversible and irreversible atrio-ventricular block by microwave energy, in *The 60th Scientific Sessions, American Heart Association, Anaheim*, CA, 1987; also in *Circulation* 76, 1612, 1987.
225. Lin, J.C., Beckman, K.J., Hariman, R.J., Bharati, S., Lev, M., and Wang, Y.J., Microwave ablation of the atrioventricular junction in open heart dogs, *Bioelectromagnetics*, 16, 97, 1995.
226. Lin, J.C., Hyperthermia therapy, in *Encyclopedia of Electrical and Electronics Engineering*, vol. 9, Webster, J.G., Ed., Wiley, New York, 1999, 450–460.
227. McRury, I.D. and Haines, D.E., Ablation for the treatment of arrhythmias, *Proc. IEEE*, 84, 404, 1996.
228. Lin, J.C., Hariman, R.J., Wang, Y.G., and Wang, Y.J., Microwave catheter ablation of the atrioventricular junction in closed-chest dogs, *Med. Biol. Eng. Comput.*, 34, 295, 1996.
229. Lin, J.C., Catheter microwave ablation therapy for cardiac arrhythmias, *Bioelectromagnetics,* 20, S4, 120, 1999.
230. Huang, S.K.S. and Wilber, D.J., Eds., *Radiofrequency Catheter Ablation of Cardiac Arrhythmias: Basic Concepts and Clinical Applications*, 2nd ed., Futura, Armonk, New York, 2000.
231. Lin, J.C., Biophysics of radiofrequency ablation, in *Radiofrequency Catheter Ablation of Cardiac Arrhythmias: Basic Concepts and Clinical Applications*, 2nd ed, Huang, S.K.S. and Wilber, D.J., Eds., Futura, Armonk, New York, 2000,13–24.
232. Wonnel, T.L., Stauffer, P.R., and Langberg, J.J., Evaluation of microwave and radio-frequency catheter ablation in a myocardium-equivalent phantom model, *IEEE Trans. Biomed. Eng.*, 39, 10, 1086, 1992.
233. Lin, J.C., Wang, Y.L., and Heriman, R.J., Comparison of power deposition patterns produced by microwave and radio frequency cardiac ablation catheters, *Electron. Lett.*, 30, 12, 922, 1994.
234. Lin, J.C., Studies on microwaves in medicine and biology: from snails to humans, *Bioelectromagnetics*, 25, 146, 2004.
235. Labonté, S., Blais, A., Legault, S.R., Ali, H.Q., and Roy, L., Monopole antennas for microwave catheter ablation, *IEEE Trans. Microwave Theory Technol.*, 44, 1832, 1996.
236. Kaouk, Z., Khebir, A., and Savard, P., A finite element model of a microwave catheter for cardiac ablation, *IEEE Trans. Microwave Theory Technol.*, 44, 1848, 1996.
237. Lin, J.C. and Wang, Y.J., The cap-slot catheter antenna for microwave ablation therapy, *IEEE Trans. Biomed. Eng.*, 43, 657, 1996.
238. Lin, J.C. and Wang, Y.J., A catheter antenna for percutaneous microwave therapy, *Microwave Opt. Technol. Lett.*, 8, 70, 1995.
239. Gu, Z., Rappaport, C.M., Wang, P.J., and VanderBrink, B.A., Development and experimental verification of the wide-aperture catheter-based microwave cardiac ablation antenna, *IEEE Trans. Microwave Theory Technol.*, 48, 1892, 2000.
240. Nevels, R.D., Arndt, G.D., Raffoul, G.W., Carl, J.R., and Pacifico, A., Microwave catheter design, *IEEE Trans. Biomed. Eng.*, 45, 885, 1998.
241. Rosenbaum, R.M., Greenspon, A.J., Hsu, W.L., Walinsky, S.P., and Rosen, A., RF and microwave ablation for the treatment of ventricular tachycardia, *IEEE MTT-S Int. Microwave Symp. Digest*, 1993, 1155.
242. Greenspon, A.J., Advances in catheter ablation for the treatment of cardiac arrhythmias, *IEEE Trans. Microwave Theory Technol.*, 48, 2670, 2000.

243. Panescu, D., Whayne, J.G., Fleischman, S.D., Mirotznik, M.S., Swanson, D.K., and Webster, J.G., Three-dimensional finite element analysis of current density and temperature distributions during radio-frequency ablation, *IEEE Trans. Biomed. Eng*., 42, 879, 1995.
244. Cao, H., Vorperian,, V.R., Tungjitkusolmun, S., Tsai, J.Z., Haemmerich, D., Choy, Y.B., and Webster, J.G., Flow effect on lesion formation in RF cardiac catheter ablation, *IEEE Trans. Biomed. Eng*., 48, 425, 2001.
245. Tungjitkusolmun, S., Vorperian, V.R., Bhavaraju, N., Cao, H., Tsai, J.Z., and Webster, J.G., Guidelines for predicting lesion size at common endocardial locations during radio-frequency ablation, *IEEE Trans. Biomed. Eng*., 48, 194, 2001.
246. Bernardi, P., Cavagnaro, M., Lin, J.C., Pisa, S., and Piuzzi, E., Distribution of SAR and temperature elevation induced in a phantom by a microwave cardiac ablation catheter, *IEEE Trans. Microwave Theory Technol*., 52, 1978, 2004 (special issue on medical applications and biological effects of RF/microwaves).
247. McLucas, B., Management of uncontrolled menorrhagia with the resectoscope, *Minim. Invasive Ther*., 1, 131, 1992.
248. Brooks, P.G., Clouse, J., and Morris, L.S., Hysterectomy vs resectoscopic endometrial ablation for the control of abnormal uterine bleeding—a cost-comparative study, *J. Reprod. Med*., 39, 755, 1994.
249. Pinion, S.B., Parkin, D.E., Abramovich, D.R., Naji, A., Alexander, D.A., Russel, I.T., and Kitchener, H.C., Randomized trial of hysterectomy, endometrial laser ablation, and transcervical endometrial resection for dysfunctional uterine bleeding, *Br. Med.J*., 309, 979, 1994.
250. Seymour, J., Wallage, S., Graham, W., Parkin, D., and Cooper, K., The cost of microwave endometrial ablation under different anaesthetic and clinical settings, *BJOG: Int. J. Obstet. Gynaecol*., 110, 922, 2003.
251. Wallage, S., Cooper, K.G., Graham, W.J., and Parkin, D.E., A randomised trial comparing local versus general anaesthesia for microwave endometrial ablation, *BJOG: Int. J. Obstet. Gynaecol*., 110, 799, 2003.
252. Lalonde, A., Evaluation of surgical options in menorrhagia, *Br.J. Obstet. Gynaecol*., 101, 8, 1994.
253. Erian, J., Endometrial ablation in the treatment of menorrhagia, *Br.J. Obstet. Gynaecol*, 104, 19, 1994.
254. Daniell, J.F., Kurtz, B.R., and Ke, R.W., Hysteroscopic endometrial ablation using the rollball electrode, *Obstet. Gynecol*., 80, 329, 1992.
255. Reid, P.C., Turrell, W., Smith, J.H.F., Kenndy, A., and Sharp, F., Nd-YAG laser endometrial ablation—histological aspects of uterine healing, *Int. J. Gynecol. Pathol*., 11, 174, 1992.
256. Phillips, D.R., A comparison of endometrial ablation using the Nd:YAG laser or electrosurgical techniques, *J. Am. Assoc. Gynecol. Laparosc*., 1, 235–239, 1993.
257. Sharp, N.C., Cronin, N., Feldberg, I., Evans, M., Hodgson, D., and Ellis, S., Microwaves for menorrhagia: s new fast technique for endometrial ablation, *Lancet*, 346, 1003, 1995.
258. Cooper, K.G., Bain, C., and Parkin, D.E., Comparison of microwave endometrial ablation and transcervical resection of the endometrium for treatment of heavy menstrual loss: a randomised trial, *Lancet*, 354, 1859, 1999.
259. Pisa, S., Cavagnaro, M., Bernardi, P., and Lin, J.C., A 915-MHz antenna for microwave thermal ablation treatment: physical design, computer modeling and experimental measurement, *IEEE Trans. Biomed. Eng*., 48, 599, 2001.
260. Stea, B., Kittleson, J., and Cassady, J.R., Treatment of malignant glioma with interstitial irradiation and hyperthermia, *Int. J. Radiat. Oncol. Biol. Phys*., 24, 657, 1992.
261. Overgaard, J., Gonzalez, D.G., Hulshof, M., Arcangeli, G., Dahl, O., Mella, O., and Bentzen, S.M., Randomised trial of hyperthermia as adjuvant to radiotherapy for recurrent or metastatic malignant melanoma, *Lancet*, 345, 540, 1995.
262. Kuwano, H., Sumiyoshi, K., Watanabe, M., Sadanaga, N., Nozoe, T., Yasuda, M., and Sugimachi, K., Preoperative hyperthermia combined with chemotherapy and irradiation for the treatment of patients with esophageal carcinoma, *Tumorigenesis*, 81, 18, 1995.
263. Nakajima, T., Roberts, D.W., Ryan, T.P., Hoopes, P.J., Coughlin, C.T., Trembly, B.S., and Strohbehn, J.W., Pattern of response to interstitial hyperthermia and brachytherapy for malignant intracranial tumour: a CT analysis, *Int. J. Hyperthermia*, 9, 491, 1993.
264. Sneed, P.K., Stauffer, P.R., McDermott, M.W., Diederich, C.J., Lamborn, K.R., Prados, M.D., Chang, S., Weaver, K.A., Spry, L., Malec, M.K., Lamb, S.A., Voss, B., Davis, R.L., Wara, W.M.,

Larson, D.A., Phillips, T.L., and Gutin, P.H., Survival benefit of hyperthermia in a prospective randomized trial of brachytherapy boost +/− hyperthermia for glioblastoma multiforme, *Int. J. Radiat. Oncol. Biol. Phys*., 40, 287, 1998.
265. Coughlin, C.T., Douple, E.B., Strohbehn, J.W., Eaton, J.W., Jr., Trembly, B.S., and Wong, T.Z., Interstitial hyperthermia in combination with brachytherapy, *Radiobiology*, 148, 285, 1983.
266. Hiraoka, M., Mitsumori, M., Hiroi, N., Ohno, S., Tanaka, Y., Kotsuka, Y., and Sugimachi, K., Development of RF and microwave heating equipment and clinical applications to cancer treatment in Japan, *IEEE Trans. Microwave Theory Technol*., 48, 1789, 2000.
267. King, R.W.P., Trembly, B.S., and Strohbehn, J.W., The electromagnetic field of an insulated antenna in a conducting or dielectric medium, *IEEE Trans. Microwave Theory Technol*., 31, 574, 1983.
268. Jones, K.M., Mechling, J.A., Trembly, B.S., and Strohbehn, J.W., SAR distribution for 915 MHz interstitial microwave antennas used in hyperthermia for cancer therapy, *IEEE Trans. Biomed. Eng*., 35, 851, 1988.
269. Iskander, M.F. and Tumeh, A.M., Design optimization of interstitial antennas, *IEEE Trans. Biomed. Eng*., 36, 238, 1989.
270. Su, D.W.-F. and Wu, L.-K., Input impedance characteristics of coaxial slot antennas for interstitial microwave hyperthermia, *IEEE Trans. Microwave Theory Technol*., 47, 302, 1999.
271. Camart, J.C., Despretz, D., Chive, M., and Pribetich, J., Modeling of various kinds of applicators used for microwave hyperthermia based on the FDTD method, *IEEE Trans. Microwave Theory Technol*., 44, 1811, 1996.
272. Ahn, H.R. and Lee, K., Interstitial antennas tipped with reactive load, *IEEE Microwave Wireless Comp. Lett*., 15, 83, 2005.
273. Longo, L., Gentili, G.B., Cerretelli, M., and Tosoratti, N., A coaxial antenna with miniaturized choke for minimally invasive interstitial heating *IEEE Trans. Biomed. Eng*., 50, 82, 2003.
274. Brace, C.L., Laeseke, P.F., van der Weide, D.W., and Lee, F.T., Jr., Microwave ablation with a triaxial antenna: results in *ex vivo* bovine liver, *IEEE Trans. Microwave Theory Technol*., 53, 215, 2005.
275. Jones, K.M., Mechling, J.A., Strohbehn, J.W., and Trembly, B.S., Theoretical and experimental SAR distributions for interstitial dipole antenna arrays used in hyperthermia, *IEEE Trans. Microwave Theory Technol*., 37, 1200, 1989.
276. Lin, J.C., Hirai, S., Chiang, C.L., Hsu, W.L., and Wang, Y.J., Computer simulation and experimental studies of SAR distributions of interstitial arrays of sleeved-slot microwave antennas for hyperthermia treatment of brain tumors, *IEEE Trans. Microwave Theory Technol*., 48, 2191, 2000.
277. Camart, J.C., Fabre, J.J., Prevost, B., Pribetich, J., and Chive, M., Coaxial antenna array for 915 interstitial hyperthermia: design and modelization—power deposition and heating pattern—phased array, *IEEE Trans. Microwave Theory Technol*., 40, 2243, 1992.
278. Clibbon, K.L., McCowen, A., and Hand, J.W., SAR distribution in interstitial microwaveantenna arrays with a single dipole displacement, *IEEE Trans. Biomed. Eng*., 40, 925, 1993.
279. Cherry, P.C. and Iskander, M.F., FDTD analysis of power deposition patterns of an array of interstitial antennas for use in microwave hyperthermia, *IEEE Trans. Microwave Theory Technol*., 40, 1692, 1992.
280. Cherry, P.C. and Iskander, M.F., Calculations of heating patterns of an array of microwave interstitial antennas, *IEEE Trans. Biomed. Eng*., 40, 771, 1993.
281. Gentili, G.B., Leoncini, M.L., Trembly, B.S., and Schweizer, S.F., FDTD electromagnetic and thermal analysis of interstitial hyperthermic applicators, *IEEE Trans. Biomed. Eng*., 42, 973, 1995.
282. Pisa, S., Cavagnaro, M., Piuzzi, E., Bernardi, P., and Lin, J.C., Power density and temperature distributions produced by interstitial arrays of sleeved-slot antennas for hyperthermic cancer therapy, *IEEE Trans. Microwave Theory Technol*., 5, 2418, 2003.
283. Lin, J.C. and Wang, Y.J., Interstitial microwave antennas for thermal therapy, *Int. J. Hyperthermia*, 3, 37, 1987.
284. Chou, C.-K., Therapeutic heating applications of radio frequency energy, *Biological and Medical Aspects*, Barnes, F.S. and Greenebaum, B., Eds., Taylor & Francis, Boca Raton, FL, 2006, Chapter 12.
285. Black, D., Thermoregulation in the presence of radiofrequency fields, in *Biological and Medical Aspects*, Barnes, F.S. and Greenebaum, B., Eds., Taylor & Francis, Boca Raton, FL, 2006, Chapter 5.